ARL-TR-10469 • Oct 2026

# Atmospheric Intelligence for Hybrid Power Advancements (AIHPA): Volume 6 (Photovoltaic Characterization: Voltage, Current, Thermal, and IR)

Robert S. Jane, Gail T. Vaucher, Michael S. D'Arcy, Michael S. Lee, and Morris M. Berman

Controlled by: FCDD-RLA-GD
CUI Category:
Distribution/Dissemination Controls: A
POC: Robert S. Jane, (520) 691-5040

DISTRIBUTION STATEMENT A. Approved for public release; distribution is unlimited.

## NOTICES

### Disclaimers

The findings in this report are not to be construed as an official Department of the Army position unless so designated by other authorized documents.

Citation of manufacturer's or trade names does not constitute an official endorsement or approval of the use thereof.

DESTRUCTION NOTICE—For classified documents, follow the procedures in DOD 5220.22-M, National Industrial Security Program Operating Manual, Chapter 5, Section 7, or DoDM 5200.01, Volume 3, DoD Information Security Program: Protection of Classified Information.

ARL-TR-10469 ● Oct 2026






# Atmospheric Intelligence for Hybrid Power Advancements (AIHPA): Volume 6 (Photovoltaic Characterization: Voltage, Current, Thermal, and IR)

**Robert S. Jane, Gail T. Vaucher, Michael S. D'Arcy, Michael S. Lee, and Morris M. Berman**
***DEVCOM Army Research Laboratory***

**DISTRIBUTION STATEMENT A. Approved for public release; distribution is unlimited.**

# REPORT DOCUMENTATION PAGE

| 1. REPORT DATE | 2. REPORT TYPE | 3. DATES COVERED | |
|---|---|---|---|
| | | START DATE | END DATE |
| October 2026 | Technical Report | 7/1/24 | 9/30/24 |

**4. TITLE AND SUBTITLE**

Atmospheric Intelligence for Hybrid Power Advancements (AIHPA): Volume 6 (Photovoltaic Characterization: Voltage, Current, Thermal, and IR)

| 5a. CONTRACT NUMBER | 5b. GRANT NUMBER | 5c. PROGRAM ELEMENT NUMBER |
|---|---|---|
| **5d. PROJECT NUMBER** | **5e. TASK NUMBER** | **5f. WORK UNIT NUMBER** |

**6. AUTHOR(S)**
Robert S. Jane, Gail T. Vaucher, Michael S. D'Arcy, Michael S. Lee, and Morris M. Berman

**7. PERFORMING ORGANIZATION NAME(S) AND ADDRESS(ES)**
DEVCOM Army Research Laboratory
ATTN: FCDD-RLA-GD
Adelphi, MD 20783

**8. PERFORMING ORGANIZATION REPORT NUMBER**
ARL-TR-10469

| 9. SPONSORING/MONITORING AGENCY NAME(S) AND ADDRESS(ES) | 10. SPONSOR/MONITOR'S ACRONYM(S) | 11. SPONSOR/MONITOR'S REPORT NUMBER(S) |
|---|---|---|
| | | |

**12. DISTRIBUTION/AVAILABILITY STATEMENT**
DISTRIBUTION STATEMENT A. Approved for public release; distribution is unlimited.

**13. SUPPLEMENTARY NOTES**
ORCIDs: Robert S. Jane, 0000-0001-6742-7306; Michael S. Lee, 0000-0002-0419-6069

**14. ABSTRACT**
The DoD is the largest energy consumer in the U.S. Federal Government, using 613.712 trillion British thermal units in FY23. In the context of great power competition, reliable energy delivery at the tactical edge is a critical operational enabler requiring hybridized, resilient microgrids. This report details the thermal characterization of an operational photovoltaic array intended for contested edge environments. Crucially, this investigation demonstrates that standard manufacturer power models are insufficient for operational prediction due to unmodeled cell temperature dynamics, especially at lower irradiance levels. To resolve this limitation, this work develops a validated lumped-parameter thermal model and demonstrates that tactical forward-looking IR thermal imagers provide an effective, noninvasive method for monitoring array-level thermal behavior in the field.

**15. SUBJECT TERMS**
Energy Sciences, photovoltaic arrays, thermal analysis, infrared thermography, hybrid power systems, energy forecasting, tactical microgrids, solar energy, atmospheric intelligence

| 16. SECURITY CLASSIFICATION OF: | | | 17. LIMITATION OF ABSTRACT | 18. NUMBER OF PAGES |
|---|---|---|---|---|
| a. REPORT | b. ABSTRACT | C. THIS PAGE | | |
| UNCLASSIFIED | UNCLASSIFIED | UNCLASSIFIED | SAR | 92 |

| 19a. NAME OF RESPONSIBLE PERSON | 19b. PHONE NUMBER *(Include area code)* |
|---|---|
| Robert S. Jane | (520) 691-5040 |

**STANDARD FORM 298 (REV. 5/2020)**
*Prescribed by ANSI Std. Z39.18*

## Contents

**List of Figures** v

**List of Tables** x

**1. Introduction** 1

**2. Background** 3

**3. Voltage and Current Characterizations** 7

3.1 Voltage and Current Characterizations 7

3.2 Energy and Power Characterizations 18

3.3 Summary 22

**4. Thermal Characterizations** 23

4.1 Thermal Model A Characterizations 29

4.2 Thermal Model B Characterizations 32

4.3 Summary 34

**5. FLIR Characterizations** 35

5.1 FLIR Characterizations for 30 May 2024 37

5.2 FLIR Characterizations for 22 July 2024 41

5.3 FLIR Characterizations for 23 July 2024 46

5.4 FLIR Characterizations for 25 July 2024 51

5.5 Summary 55

**6. Conclusions** 57

**7. Future Work** 60

**8. References** 61

**Appendix A: AIHPA Testbed** 64

**Appendix B: 315 W Sunmodule Pro-Series XL Monocrystalline** **72**

**List of Symbols, Abbreviations, and Acronyms** **79**

**Distribution List** **80**

## List of Figures


Figure 1. Measured irradiance and panel power time series for 11 June 2024, resembling clear sky conditions.....4

Figure 2. Measured irradiance and panel power time series for 20 August 2024, resembling clear sky conditions.....4

Figure 3. Measured irradiance and panel power time series for 29 September 2024, resembling clear sky conditions.....5

Figure 4. Measured and modeled panel power time series for 11 June and 29 September 2024, resembling clear sky conditions. .....6

Figure 5. 350 W case: current–voltage and power–voltage curves from 350 W applied to PV reference cell.....9

Figure 6. 350 W case: measured cell temperature at MPP. ..... 10

Figure 7. 450 W case: current–voltage and power–voltage curves from 450 W applied to PV reference cell..... 10

Figure 8. 450 W case: measured cell temperature at MPP. ..... 11

Figure 9. 550 W case: current–voltage and power–voltage curves from 550 W applied to PV reference cell..... 11

Figure 10. 550 W case: measured cell temperature at MPP. ..... 12

Figure 11. 650 W case: current–voltage and power–voltage curves from 650 W applied to PV reference cell..... 12

Figure 12. 650 W case: measured cell temperature at MPP. ..... 13

Figure 13. 750 W case: current–voltage and power–voltage curves from 750 W applied to PV reference cell..... 13

Figure 14. 750 W case: measured cell temperature at MPP. ..... 14

Figure 15. 850 W case: current–voltage and power–voltage curves from 850 W applied to PV reference cell..... 14

Figure 16. 850 W case: measured cell temperature at MPP. ..... 15

Figure 17. 950 W case: current–voltage and power–voltage curves from 950 W applied to PV reference cell..... 15

Figure 18. 950 W case: measured cell temperature at MPP. ..... 16

Figure 19. 1025 W case: current–voltage and power–voltage curves from 1025 W applied to PV reference cell..... 16

Figure 20. 1025 W case: measured cell temperature at MPP. ..... 17

Figure 21. A comparison between the manufacturer data sheet representative voltage–current (current–voltage) curves compared with the configured Simulink subject to an irradiance ranging from 1025 to 350 W/m$^2$. 20

Figure 22. A comparison between the manufacturer data sheet representative voltage–power (power–voltage) curves compared with the configured Simulink subject to an irradiance ranging from 1025 to 350 W/m$^2$. 21

Figure 23. Measured cell temperature, subjected to an irradiance ranging from 1025 to 350 W/m$^2$. ..... 24

Figure 24. Lumped parameter 1D thermal models postulated for approximating the thermal behavior of the PV reference cell. ..... 26

Figure 25. A comparison between the measured and approximated cell temperature, subjected to an irradiance of 1025, 950, 650, 550, or 450 W/m$^2$ and Thermal Model A. ..... 31

Figure 26. A comparison between the measured and approximated cell temperature, subjected to an irradiance of 1025, 950, 650, 550, or 450 W/m$^2$ and Thermal Model B. ..... 33

Figure 27. The approximate configuration of the PV array located on an academic building at USMA. ..... 36

Figure 28. The approximate configuration of the PV array included within the AIHPA Testbed. ..... 36

Figure 29. The observed PV panel cell temperatures obtained via the FLIR camera as deployed to USMA on 30 May 2024 from 1321 through 1343 EST. ..... 38

Figure 30. The observed PV panel cell temperatures obtained via the FLIR camera as deployed to AIHPA Testbed on 30 May 2024 from 1300 through 1400 EST. ..... 39

Figure 31. The observed PV panel cell temperatures obtained via the FLIR camera as deployed to AIHPA Testbed on 30 May 2024 from 1300 through 1400 EST. ..... 40

Figure 32. The observed PV panel cell temperatures obtained via the FLIR camera as deployed to AIHPA Testbed on 22 July 2024 from 0700 through 1800 MST. ..... 41

Figure 33. The observed PV panel cell temperatures obtained via the FLIR camera as deployed to AIHPA Testbed on 22 July 2024 from 0700 through 1800 MST. ..... 42

Figure 34. The observed PV panel cell temperatures obtained via the FLIR camera as deployed to AIHPA Testbed on 22 July 2024 from 0700 through 1800 MST. ..... 43

Figure 35. The observed PV panel cell temperatures obtained via the FLIR camera as deployed to AIHPA Testbed on 22 July 2024 from 0700 through 1800 MST. ..... 44

Figure 36. The observed PV panel cell temperatures obtained via the FLIR camera as deployed to AIHPA Testbed on 22 July 2024 from 0700 through 1800 MST. ..... 45

Figure 37. The observed PV panel cell temperatures obtained via the FLIR camera as deployed to AIHPA Testbed on 23 July 2024 from 0700 through 1800 MST. ..... 46

Figure 38. The observed PV panel cell temperatures obtained via the FLIR camera as deployed to AIHPA Testbed on 23 July 2024 from 0700 through 1800 MST. ..... 47

Figure 39. The observed PV panel cell temperatures obtained via the FLIR camera as deployed to AIHPA Testbed on 23 July 2024 from 0700 through 1800 MST. ..... 48

Figure 40. The observed PV panel cell temperatures obtained via the FLIR camera as deployed to AIHPA Testbed on 23 July 2024 from 0700 through 1800 MST. ..... 49

Figure 41. The observed PV panel cell temperatures obtained via the FLIR camera as deployed to AIHPA Testbed on 23 July 2024 from 0700 through 1800 MST. ..... 50

Figure 42. The observed PV panel cell temperatures obtained via the FLIR camera as deployed to AIHPA Testbed on 25 July 2024 from 0700 through 1800 MST. ..... 51

Figure 43. The observed PV panel cell temperatures obtained via the FLIR camera as deployed to AIHPA Testbed on 25 July 2024 from 0700 through 1800 MST. ..... 52

Figure 44. The observed PV panel cell temperatures obtained via the FLIR camera as deployed to AIHPA Testbed on 25 July 2024 from 0700 through 1800 MST. ..... 53

Figure 45. The observed PV panel cell temperatures obtained via the FLIR camera as deployed to AIHPA Testbed on 25 July 2024 from 0700 through 1800 MST. ..... 54

Figure 46. The observed ambient and panel temperature time series as measured via the MMT for 11 June 2024. ..... 56

Figure 47. The observed ambient and panel temperature time series as measured via the MMT for 20 August 2024. ..... 56

Figure 48. The observed ambient and panel temperature time series as measured via the MMT for 29 September 2024. ..... 57

Figure A-1. AIHPA Testbed measurement for 11 June 2024. Representative data illustrating ambient temperature, panel temperature, panel power output, atmospheric pressure, solar irradiance, wind direction, and wind speed. ..... 66

Figure A-2. AIHPA Testbed measurements for 20 August 2024. Representative data illustrating ambient temperature, panel temperature, panel power output, atmospheric pressure, solar irradiance, wind direction, and wind speed. ..... 67

Figure A-3. AIHPA Testbed measurements for 29 September 2024. Representative data illustrating ambient temperature, panel temperature, panel power output, atmospheric pressure, solar irradiance, wind direction, and wind speed. ..... 68

Figure A-4. AIHPA Testbed measurement for 10 June 2024. Representative data illustrating ambient temperature, panel temperature, panel power output, atmospheric pressure, solar irradiance, wind direction, and wind speed. ..... 69

Figure A-5. AIHPA Testbed measurements for 2 July 2024. Representative data illustrating ambient temperature, panel temperature, panel power output, atmospheric pressure, solar irradiance, wind direction, and wind speed. ..... 70

Figure A-6. AIHPA Testbed measurement for 4 August 2024. Representative data illustrating ambient temperature, panel temperature, panel power output, atmospheric pressure, solar irradiance, wind direction, and wind speed. ..... 71

Figure B-1. A comparison between the manufacturer data sheet representative voltage–current (VI) curves when compared with the configured Simulink subject to an irradiance ranging from 1000 to 800 W/m$^2$. 74

Figure B-2. A comparison between the manufacturer data sheet representative voltage–current (VI) curves when compared with the configured Simulink subject to an irradiance ranging from 600 to 400 W/m$^2$.. 74

Figure B-3. A comparison between the manufacturer data sheet representative voltage–current (VI) curves when compared with the configured Simulink subject to an irradiance ranging from 200 to 100 W/m$^2$.. 75

Figure B-4. Family of characteristic IV curves subject to variable temperatures and an irradiance ranging from 250 to 500 W/m$^2$. The color gradient represents electrical current, ranging from blue (lowest) to yellow (highest)..... 76

Figure B-5. Family of characteristic IV curves subject to variable temperatures and an irradiance ranging from 750 to 1000 W/m$^2$. The color gradient represents electrical current, ranging from blue (lowest) to yellow (highest)..... 76

Figure B-6. Family of characteristic power–voltage curves subject to variable temperatures and an irradiance ranging from 250 to 500 W/m$^2$. The color gradient represents electrical power, ranging from blue (lowest) to yellow (highest). ..... 77

Figure B-7. Family of characteristic power–voltage curves subject to variable temperatures and an irradiance ranging from 750 to 1000 W/m$^2$. The color gradient represents electrical power, ranging from blue (lowest) to yellow (highest). ..... 77

Figure B-8. A multidimensional surface approximating the maximum power point subject to an irradiance and temperature parameter sweep.The color gradient represents electrical power, ranging from blue (lowest) to yellow (highest). ..... 78

## List of Tables

Table 1. Oriel PV reference cell recipe parameters. ..... 7

Table 2. Oriel PV reference cell recipe parameters, part 2. ..... 8

Table 3. Oriel PV reference cell recipe parameters, part 3. ..... 8

Table 4. Oriel PV reference cell recipe parameters, part 4. ..... 8

Table 5. Approximate PV reference cell parameters. ..... 19

Table 6. Approximate PV reference cell physical parameters. ..... 29

Table 7. Approximate PV reference cell Thermal Model A thermal constant parameters. ..... 30

Table 8. Approximate PV reference cell Thermal Model B thermal constant parameters. ..... 32

Table B-1. Data sheet parameters for a 315-W Sunmodule Pro-Series XL monocrystalline PV module at STC. ..... 73

Table B-2. Data sheet parameters for a 315-W Sunmodule Pro-Series XL monocrystalline PV module at 800 W/m$^2$ operating at the NOTC. ..... 73

## 1. Introduction

Energy utilization will be a decisive factor in multi-domain operations during this era of great power competition. Effective, real-time energy management at the tactical edge is vital to prevent mission degradation, particularly when facing near-peer adversaries in denied, disrupted, intermittent, and limited environments and contested or delayed logistics.

Battlefield energy awareness can mitigate this degradation by leveraging virtual and physical sensors, AI and ML, and the internet of battlefield things (IoBT) to enable rapid, optimized, adaptable platform utilization. This provides near-real-time energy understanding across all command levels, enabling energy dominance through well-timed logistics, reduced energy utilization, improved threat and signature management, and extended operational reach amidst chaotic environments.

Hybridized energy and power (E&P) solutions are critical to a modernized, electrified fighting force. By diversifying energy networks with nontraditional resources such as wave, solar, or nuclear generation (complementing traditional fuels), these systems increase resiliency and enable continued operations even amidst chaotic battlefield conditions, further strengthened by wireless power beaming capabilities. The value of any such resource, however, depends on the ability to model its generation mechanisms and forecast its future output so energy can be allocated optimally. For example, wave energy converters require a detailed understanding of complex hydrodynamic mechanisms and show promise for low-power applications, unattended sensors, and surveillance in remote coastal or offshore environments. Nuclear generation depends on precise neutron regulation and integrated thermal–hydraulic control; recent reactor advancements improve its feasibility for battlefield power transfer though significant strategic, logistical, and safety concerns currently limit deployment.

This report focuses on the third of these nontraditional sources: solar generation via photovoltaic (PV) arrays. PV power output relies on semiconductor physics—photon absorption and charge separation—and is governed by two dominant environmental factors: solar irradiance and cell temperature, both of which directly affect electron excitation and power output. Solar offers significant potential for powering unattended

sensors at the tactical edge and reducing the Warfighter's logistical burden, as flexible solar solutions capable of recharging Warfighter systems minimize the need to carry numerous batteries and, when integrated with local energy storage, can extend operational endurance and enhance Warfighting capability.

While solar irradiance is the primary driver of PV power generation, its effect cannot be forecast accurately without first characterizing the thermal behavior of the cell—a relationship that remains comparatively understudied. Cell temperature directly modulates power output, and the same atmospheric thermal behavior that influences PV performance simultaneously drives energy demand through the operation of environmental control units. Accurately predicting PV cell temperature is therefore a prerequisite for forecasting both energy supply and demand at the tactical edge.

The contributions of this report are threefold: 1) deriving a predictive current–voltage and energy–power model for a representative PV thermal reference cell as a function of irradiance and temperature; 2) developing and comparing two lumped-parameter thermal models for predicting cell temperature; and 3) evaluating forward-looking IR (FLIR) imaging as a means of observing the thermal behavior of cells and arrays under field conditions.

The remainder of this report is organized as follows. Section 2 presents additional background and motivation for investigating the thermal mechanisms governing PV module E&P generation. Because a PV module comprises individual cells arranged in series and parallel strings—most commonly positive–negative (PN) junctions based on monocrystalline (mono-Si) or polycrystalline (poly-Si) silicon—a thorough understanding of cell dynamics enables the resulting characterizations to be extended to the module level. Accordingly, Section 3 presents the voltage and current characterizations of a PV thermal reference cell; Section 4 develops the lumped-parameter thermal model; and Section 5 presents the FLIR characterizations of individual cells and the PV module under observed environmental conditions. Finally, Sections 6 and 7 present conclusions and recommendations for future work.

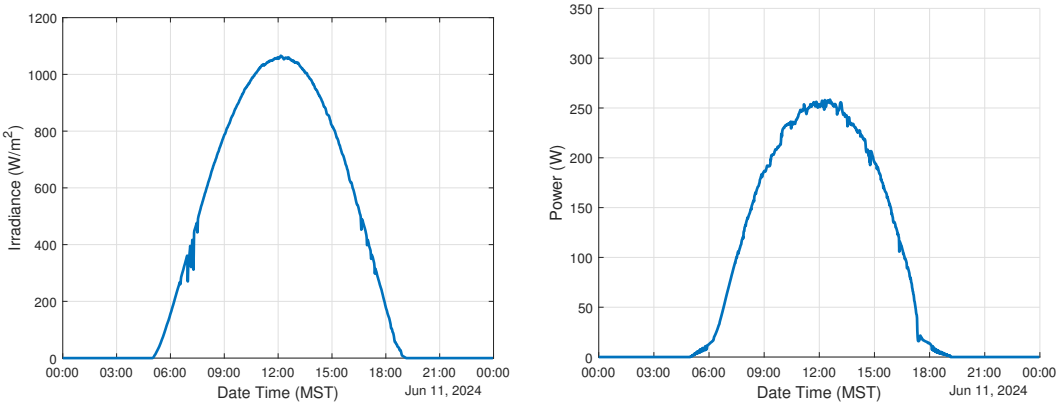
## 2. Background

The Atmospheric Intelligence for Hybrid Power Advancements (AIHPA) Testbed[1–12] originated from the In-situ Atmospheric Intelligence for Hybrid Power Grids feasibility study, which assessed whether accurate atmospheric intelligence—critical for optimizing tactical energy use—could be obtained using solely on-site measurements. Results validated this approach, demonstrating that on-site data can mitigate the limitations of, and support validation of, existing microgrid simulations.

Annual improvements to the AIHPA Testbed continue to enhance its capabilities for investigations supporting improved Warfighter capability. The current Testbed system is composed of two main components: the meteorological measurement tripod (MMT) and power train (PT). The MMT comprises a tripod with fixed temperature probes, barometer, hygrometer, pyranometer, and anemometer; all recorded by a datalogger. The PT includes a 315-W Sunmodule Pro-Series XL monocrystalline PV module with a back-panel temperature sensor, a colocated 24-V battery bank, and a resistive load bank with voltage and current sensors monitoring all power resources. The MMT is positioned upwind of the PT to characterize local atmospheric conditions and correlate them with PT performance. To broaden the scope of investigation and support fundamental research, the Testbed has been duplicated and deployed to an alternative location, namely the U.S. Military Academy (USMA). This second installation enables continued research and development from contrasted (desert vs. forested) geographic and climatic regimes. This alternate location also provides a platform for hands-on fundamental research with cadets—the future Warfighters—directly connecting energy and power experimentation to the development of the next generation of Army leaders.

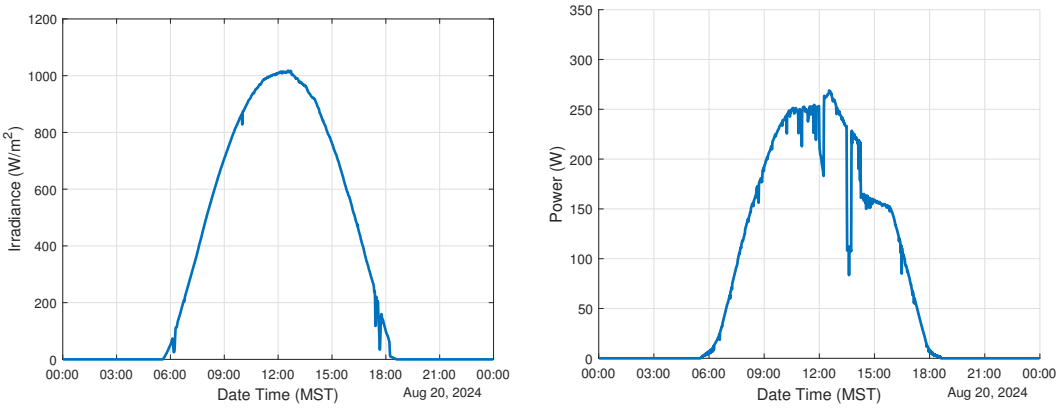
Examples of the MMT measurements under clear and partly cloudy sky conditions are provided in Appendix A. The clear sky case exhibits a Gaussian solar radiation curve, indicating uniform heating and minimal atmospheric disturbance (Figures 1–3). The partly cloudy case follows the same underlying Gaussian curve but contains periodic disturbances caused by cloud movement, evolution, and propagation. The magnitude of irradiance reduction was primarily a function of cloud type and height,

cascading into nonuniform heating.




(a) Irradiance (b) Panel power

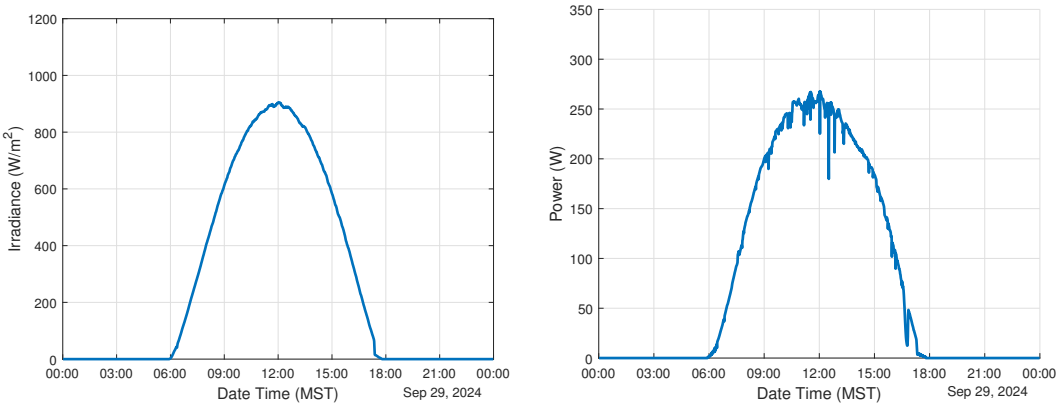
Figure 1: Measured irradiance and panel power time series for 11 June 2024, resembling clear sky conditions.




(a) Irradiance (b) Panel power

Figure 2: Measured irradiance and panel power time series for 20 August 2024, resembling clear sky conditions.

The testbed's PV module uses a maximum power point tracking (MPPT) algorithm to regulate output voltage based on irradiance and cell temperature, attaining the maximum power point (MPP) at which energy generation is maximized. This implementation deviates from standard charging profiles. For example, rather than allowing a full charge and float stage, it manages load based on battery voltage, cycling through three states: 100% load below 24.7 V, 20% trickle charge between 24.4 and 24.7 V, and complete shutdown below 24.4 V. This effectively limits the battery's charge level through a nontraditional management strategy. Maximizing




(a) Irradiance (b) Panel power

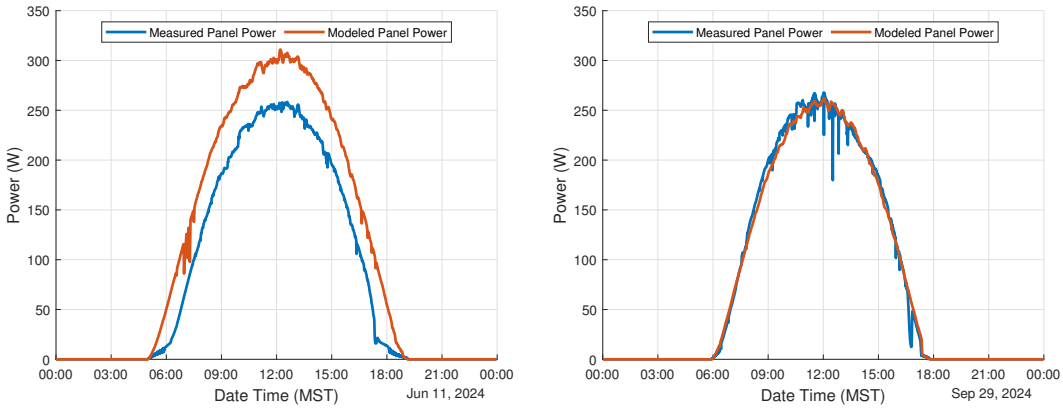
Figure 3: Measured irradiance and panel power time series for 29 September 2024, resembling clear sky conditions.

PV generation requires a continuous path for the harvested energy. If the batteries are full and no load is present, the array cannot remain at its MPP. To resolve this, excess energy that the battery bank cannot accept is diverted to the resistive load bank, where it is converted to heat. This ensures the PV module can be driven at its MPP regardless of the battery state of charge, decoupling the goal of maximizing generation from the available storage capacity.

Because this strategy maximizes generation, PV panel power output closely mirrors the irradiance profile. Clear sky observations on 11 June and 29 September 2024 confirm a strong correlation between solar irradiance and panel power, though both exhibit noticeable noise beginning approximately 2 h before solar noon and decaying 2 h after. The 20 August 2024 data show more considerable deviations from the characteristic Gaussian pattern. Local engineering logs reported no environmental disturbances, but internal documentation indicates the load switched off unexpectedly during periods of negligible load (1200–1215 MST and 1330–1345 MST). The observed degradation is therefore attributed to excessive battery charge forcing the PT into a float state. Because this represents an unresolved operating anomaly rather than an atmospheric effect, the 20 August case is excluded from the modeling analysis that follows.

Having established the testbed's ability to characterize atmospheric conditions, we

now examine whether panel power can be predicted from those measurements—a prerequisite for the optimal regulation and control of hybrid energy networks. A mathematical model approximating PV power generation (Appendix B), configured from the manufacturer's data sheet, was applied to the two valid clear sky cases (11 June and 29 September 2024), since uniform-heating conditions represent the optimal scenario for validating the model. A comparison of measured and modeled panel power is provided in Figure 4.




(a) 11 June 2024 (b) 29 September 2024

Figure 4: Measured and modeled panel power time series for 11 June and 29 September 2024, resembling clear sky conditions.

As shown in Figure 4, the model produces commensurate results for 29 September 2024 but overpredicts panel power for 11 June 2024 despite comparable sensor measurements on both dates. Examining the corresponding ambient conditions (Appendix A), the atmospheric pressure shows no distinguishing frontal passages, consistent with the gentle-breeze wind velocities observed. The wind direction, however, offers a possible clue: the better-performing case (29 September) featured easterly winds—air advecting along-axis to the solar progression—whereas 11 June was dominated by southerly and easterly airflow. While the sample is too small to be conclusive, combining this observation with seasonal changes in solar angle suggests that nonuniform heating and cooling of the panel may drive the discrepancy.

This points directly to cell temperature as the unmodeled variable. The manufacturer-configured model assumes a thermal relationship that does not hold across all conditions, and the candidate explanation—nonuniform heating—is fundamentally a

thermal effect. Accurately predicting PV panel power therefore requires a deeper, empirically grounded characterization of how irradiance and ambient conditions govern cell temperature and how that temperature in turn governs energy and power generation. This need motivates the cell-level voltage, current, thermal, and IR characterizations that constitute the remainder of this report.

## 3. Voltage and Current Characterizations

Accurate prediction of E&P performance is critical for maximizing the utility of the thermal reference cell. To this end, we established a rigorous characterization framework enabling the development of a predictive mathematical model. This framework begins with detailed current–voltage analysis, followed by comprehensive energy and power characterization.

### 3.1 Voltage and Current Characterizations

An arc lamp (i.e., an electric lamp that produces light by creating an arc between two electrodes) class AAA solar simulator (Newport; Franklin, Massachusetts) was used to characterize the current and voltage behavior of a PV reference cell. Simulators produced by Newport adhere to the most current standards established by the American Society for Testing and Materials and International Electrotechnical Commission. The arc lamp was controlled and regulated using the Oriel instrumentation software package through the creation of a recipe. Tables 1–4 show the input parameters defined by a recipe derived from simulator and PV reference cell manufacture data sheets.

Table 1: Oriel PV reference cell recipe parameters.

| Sample Area ($cm^2$) | Irradiance (Suns) | Pre-sweep delay (s) | Bias direction (char) |
|---|---|---|---|
| 4.0 | 1.0 | 0.50 | Forward > reverse |

Table 2: Oriel PV reference cell recipe parameters, part 2.

| Max reverse bias (V) | Max forward bias (V) | No. sweep points |
|---|---|---|
| 0.00 | 0.610 | 62 |

Table 3: Oriel PV reference cell recipe parameters, part 3.

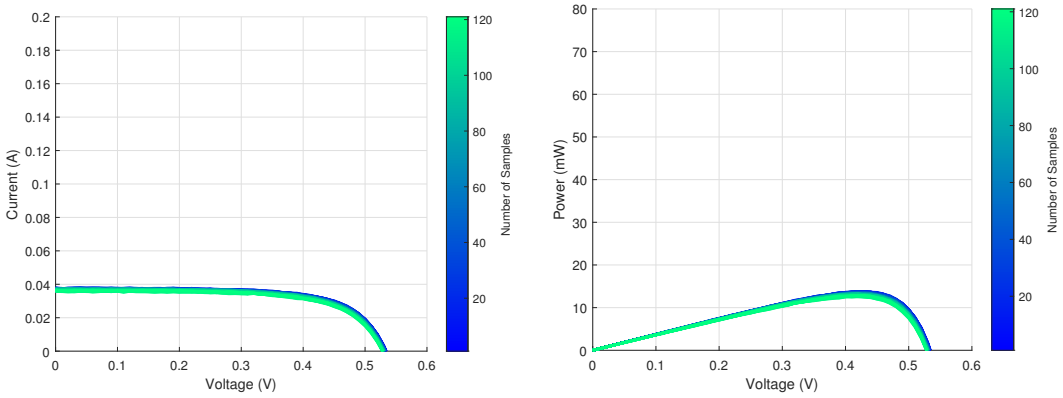
| Dwell time (ms) | Current limit (mA) | Average (char) |
|---|---|---|
| 30 | 150 | Smooth first 20% |

Table 4: Oriel PV reference cell recipe parameters, part 4.

| Shunt resistance low voltage (V) | Shunt resistance high voltage (V) |
|---|---|
| –0.600 | –0.100 |

The PV reference cell was then subjected to a repeatable measurement routine. The arc lamp was regulated and controlled to operate the internal lamp at a fixed power level regulated by a power supply, prior to implementing the measurement routine. The system was allowed to warm up to a constant power level, then the arc lamp aperture was opened, permiting the lamp to irradiate the PV reference cell for a prescribed period of time, as defined within the recipe. The recipe further dictated voltage modulation or PV reference cell regulation, equating to a voltage sweep, enabling the voltage and current characterization of the PV reference cell to be measured. The period of irradiation was dictated by dwell time, pre-sweep delay, and the number of sweep points, as defined in the recipe. The aperture was closed upon completing the measurement. The limited duration of irradiation resulted in an increase in temperature. The PV reference cell was then permitted to rest for approximately 60 s, during which time the PV reference cell temperature would decay toward the ambient conditions. The PV reference cell was irradiated again at the end of the rest period.

This process was executed 120 times sequentially. This measurement routine was applied to the arc lamp multiple times over multiple days, during which the arc lamp was regulated to different power levels including 350 W (Figures 5 and 6), 450 W (Figures 7 and 8), 550 W (Figures 9 and 10), 650 W (Figures 11 and 12), 750 W (Figures 13 and 14), 850 W (Figures 15 and 16), 950 W (Figures and 17 and 18), and 1025 W (Figures 19 and 20). A gradient color scheme was used to visually illustrate the response of the PV reference cell subject to sequential sampling periods, ranging between blue (first measurement) and a shade of teal/seafoam green (final measurement). Measured cell temperature at the MPP is shown for each power level.




(a) Characteristic current–voltage curves (b) Characteristic power–voltage curves

Figure 5: 350 W case: current–voltage and power–voltage curves from 350 W applied to PV reference cell.

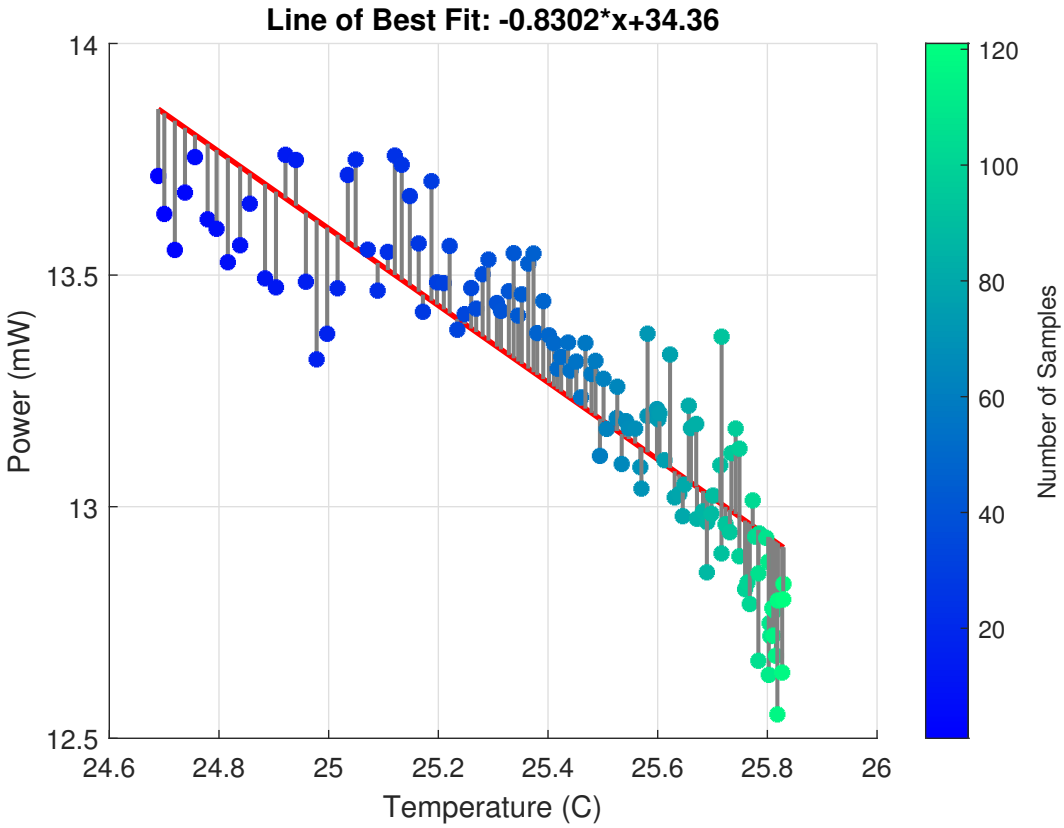
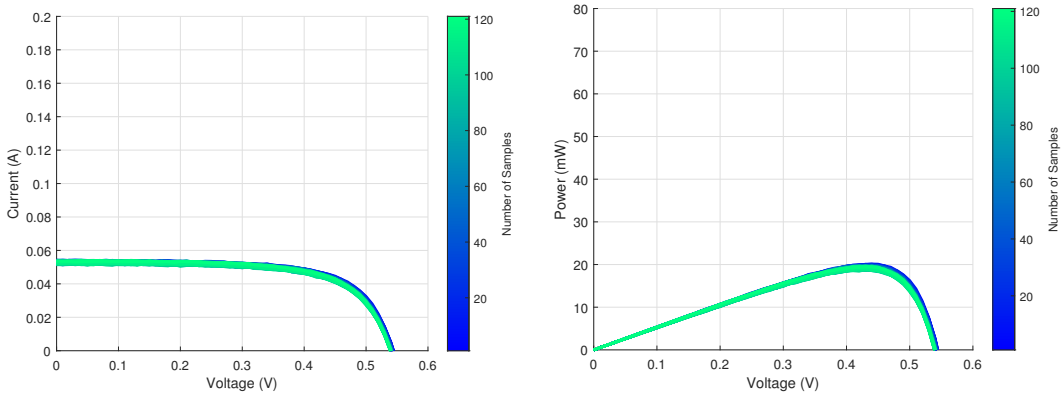



Figure 6: 350 W case: measured cell temperature at MPP.




(a) Characteristic current–voltage curves

(b) Characteristic power–voltage curves

Figure 7: 450 W case: current–voltage and power–voltage curves from 450 W applied to PV reference cell.

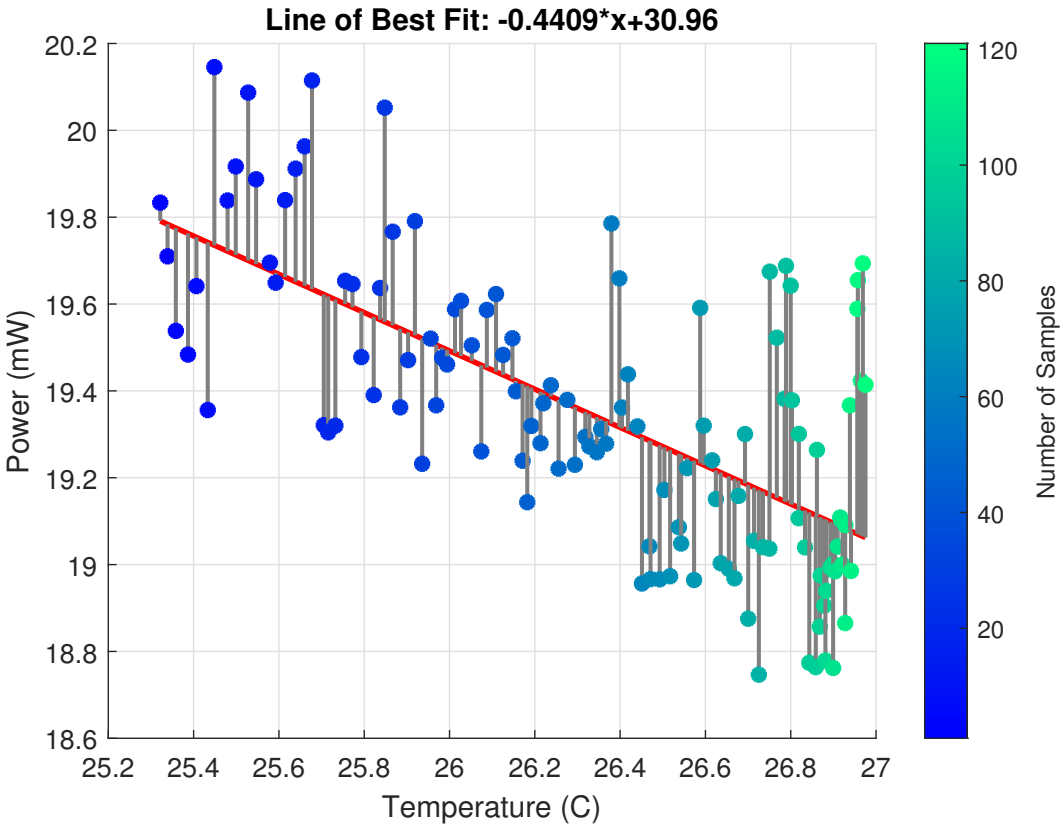
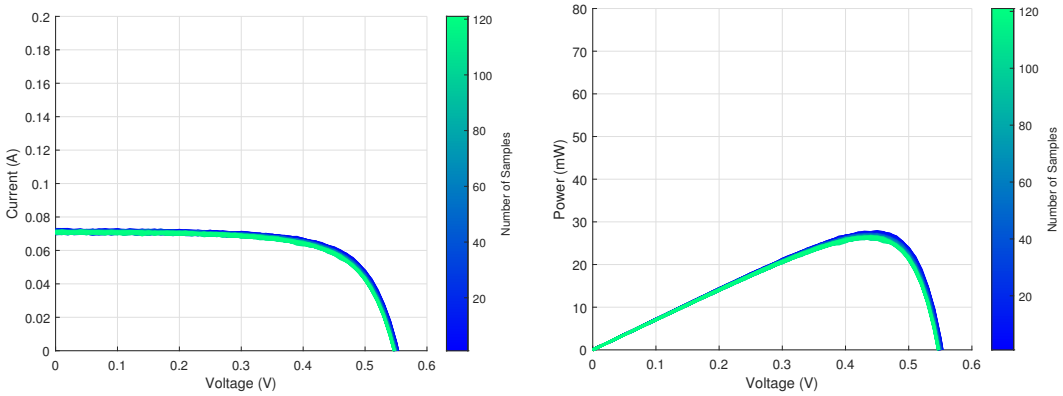



Figure 8: 450 W case: measured cell temperature at MPP.




(a) Characteristic current–voltage curves

(b) Characteristic power–voltage curves

Figure 9: 550 W case: current–voltage and power–voltage curves from 550 W applied to PV reference cell.

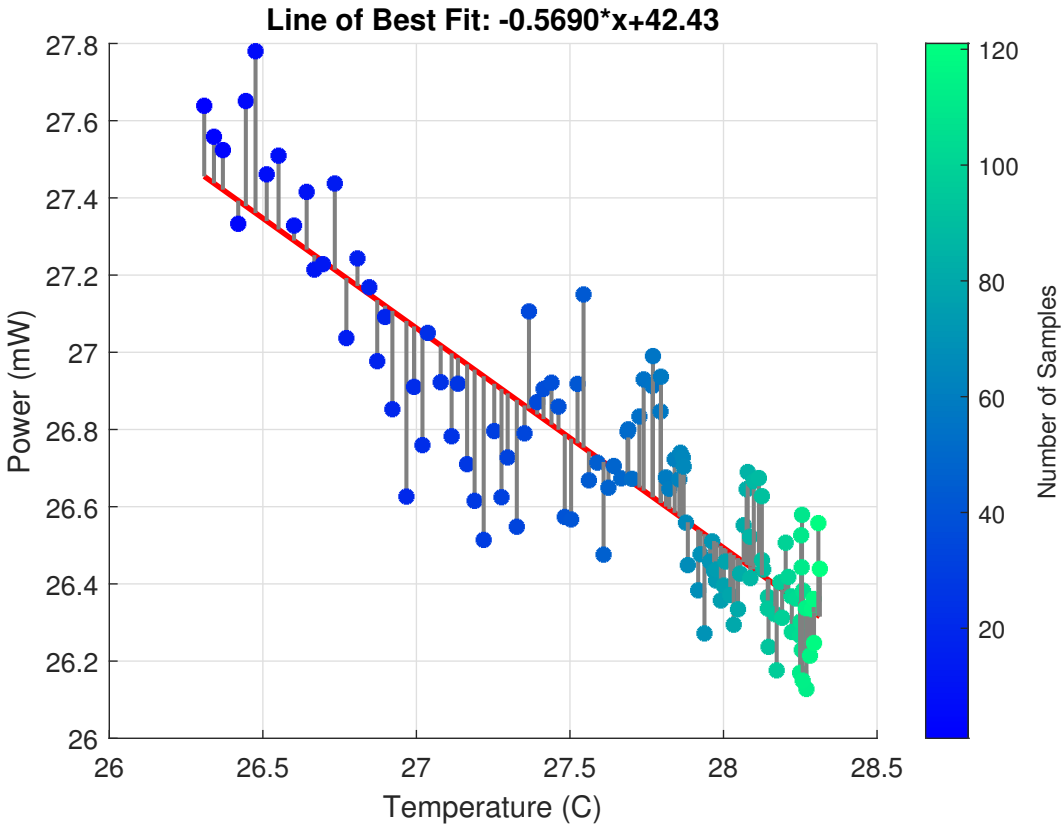
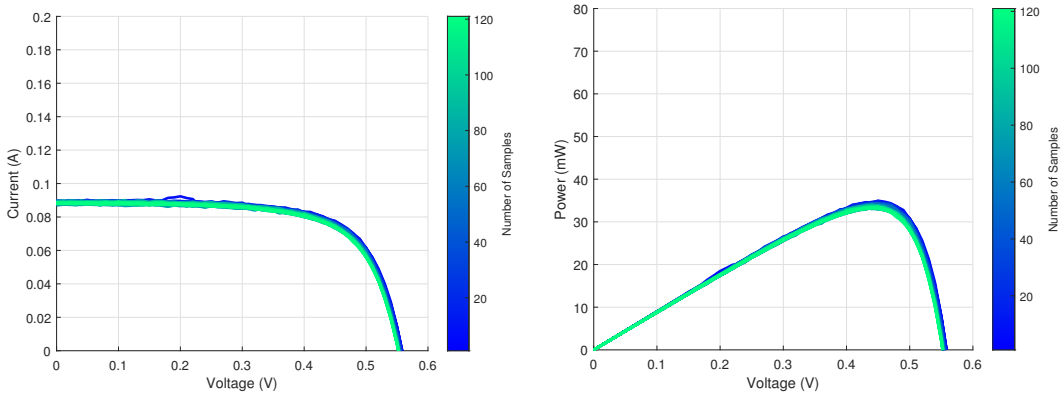



Figure 10: 550 W case: measured cell temperature at MPP.




(a) Characteristic current–voltage curves

(b) Characteristic power–voltage curves

Figure 11: 650 W case: current–voltage and power–voltage curves from 650 W applied to PV reference cell.

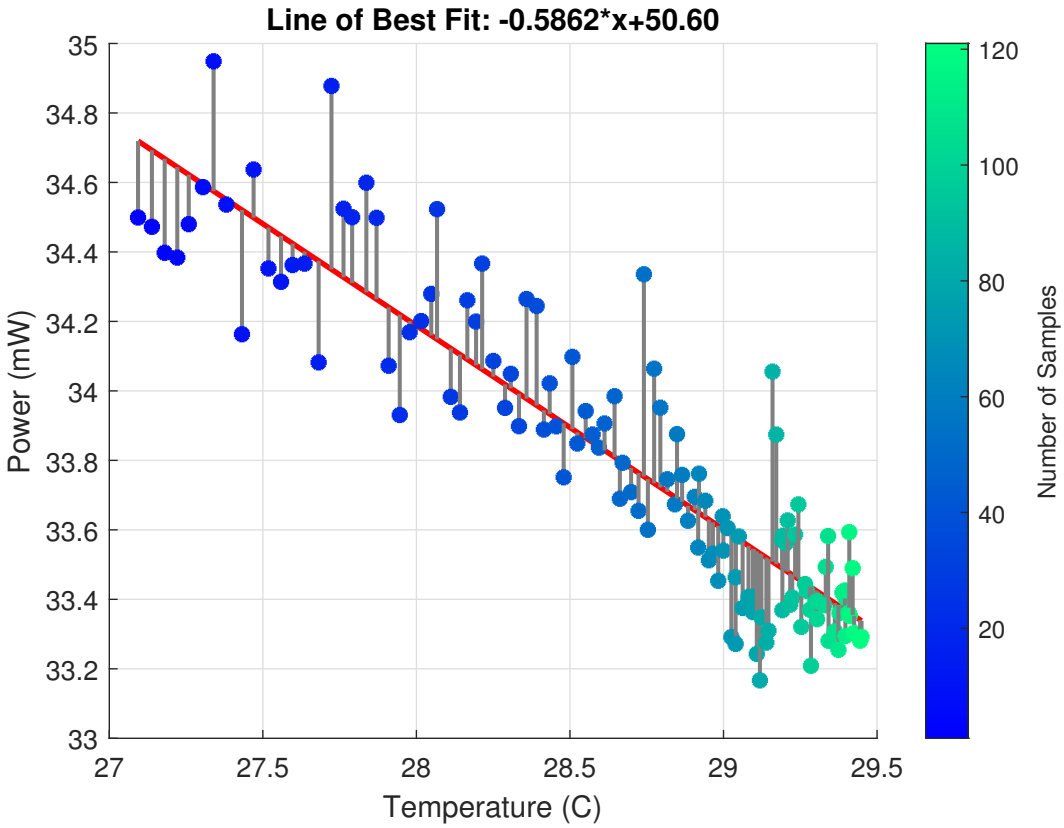
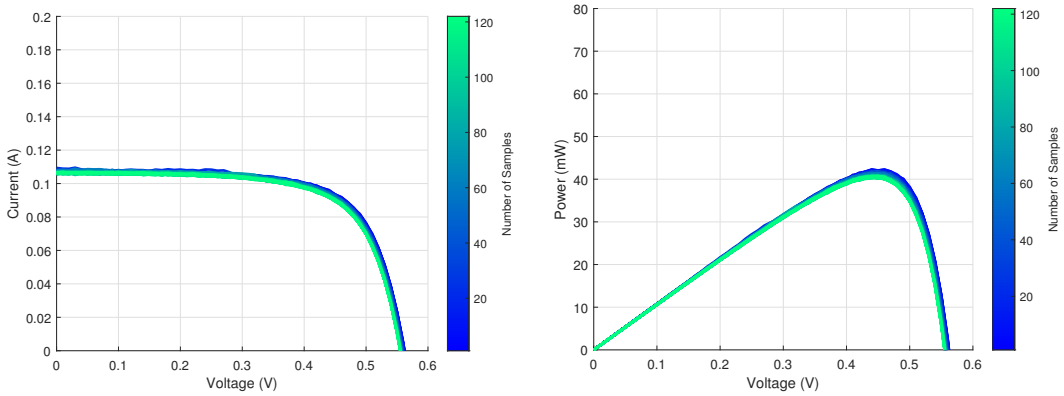



Figure 12: 650 W case: measured cell temperature at MPP.




(a) Characteristic current–voltage curves

(b) Characteristic power–voltage curves

Figure 13: 750 W case: current–voltage and power–voltage curves from 750 W applied to PV reference cell.

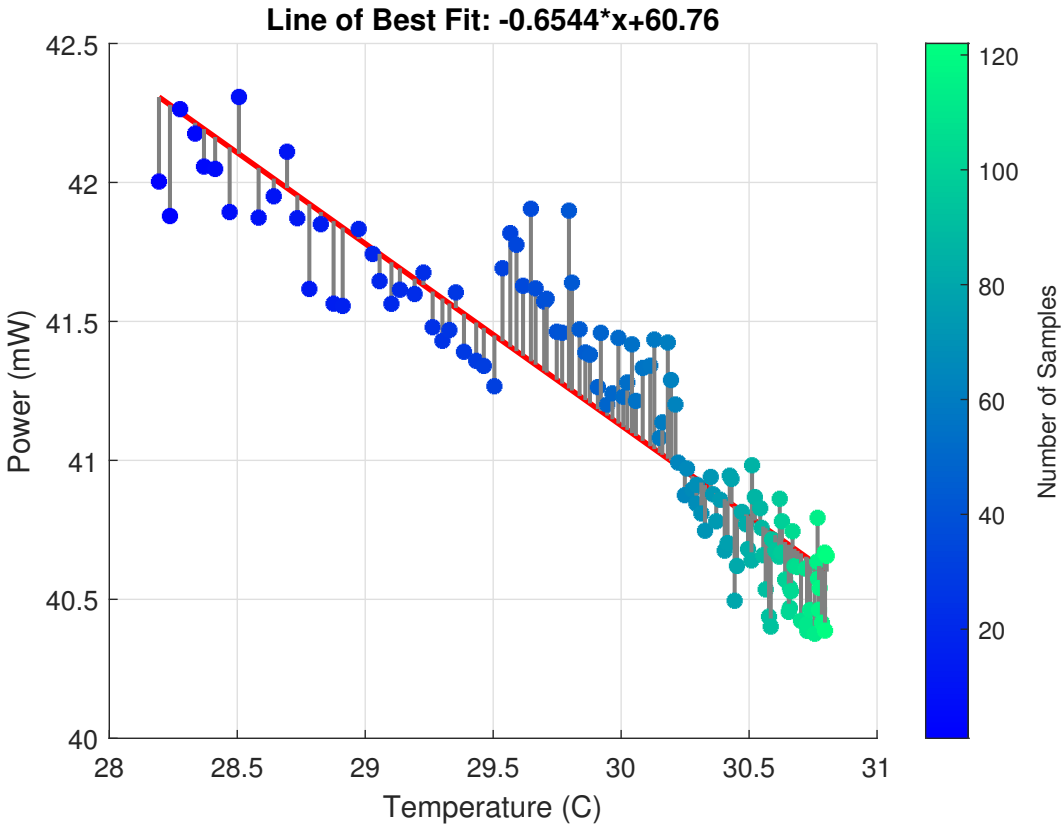
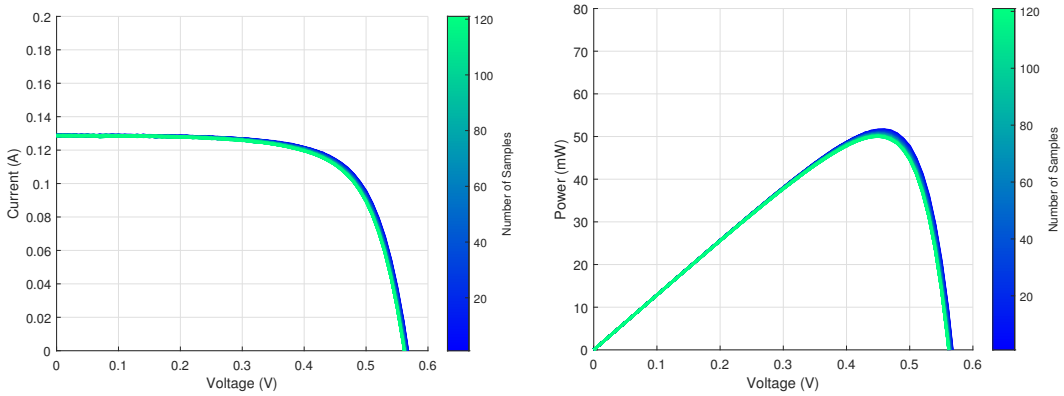



Figure 14: 750 W case: measured cell temperature at MPP.




(a) Characteristic current–voltage curves

(b) Characteristic power–voltage curves

Figure 15: 850 W case: current–voltage and power–voltage curves from 850 W applied to PV reference cell.

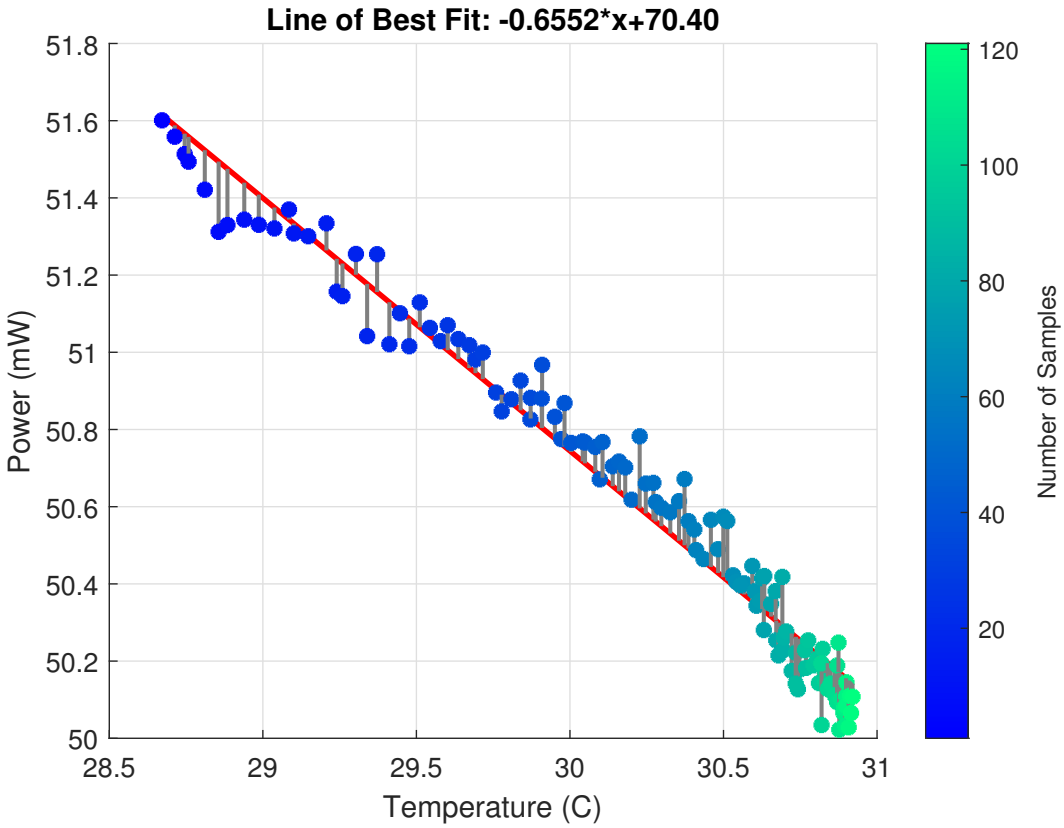
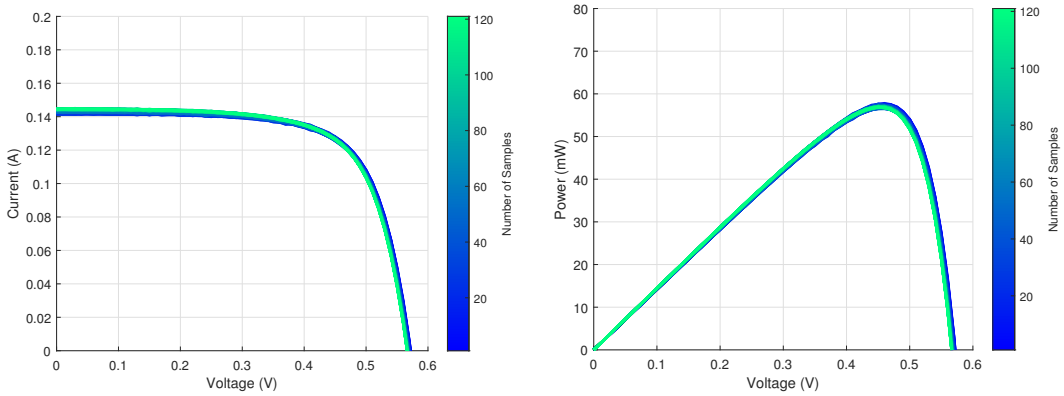



Figure 16: 850 W case: measured cell temperature at MPP.




(a) Characteristic current–voltage curves

(b) Characteristic power–voltage curves

Figure 17: 950 W case: current–voltage and power–voltage curves from 950 W applied to PV reference cell.

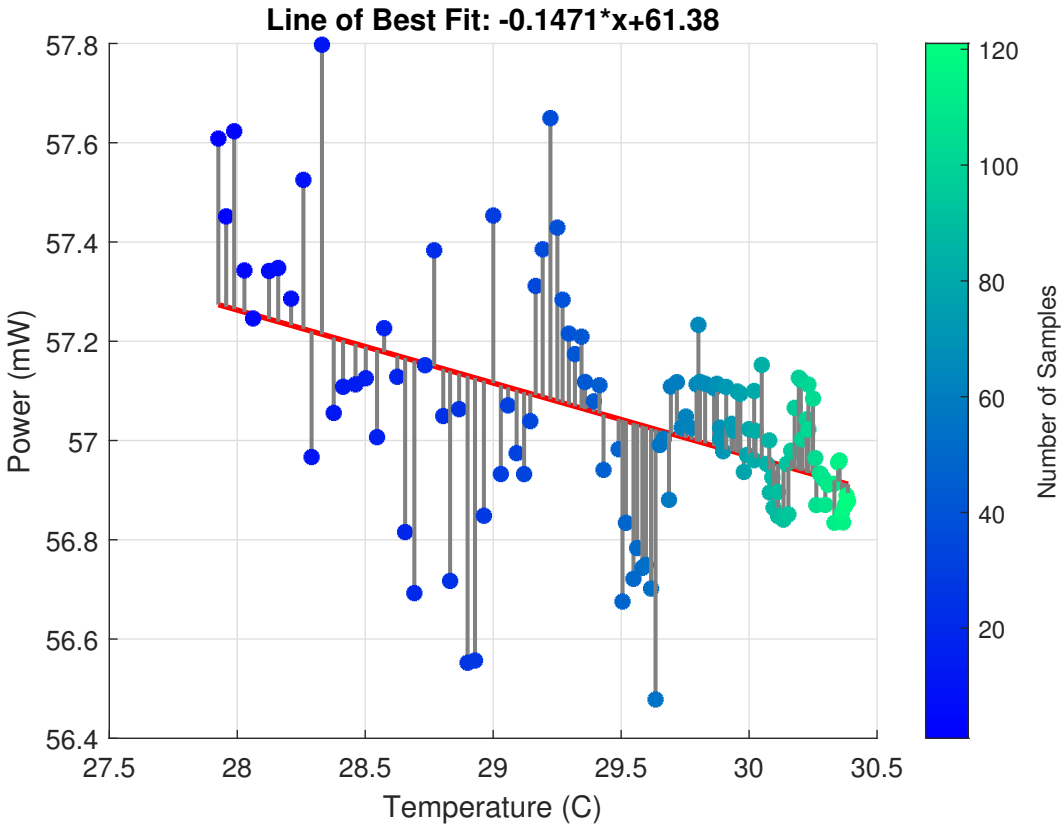
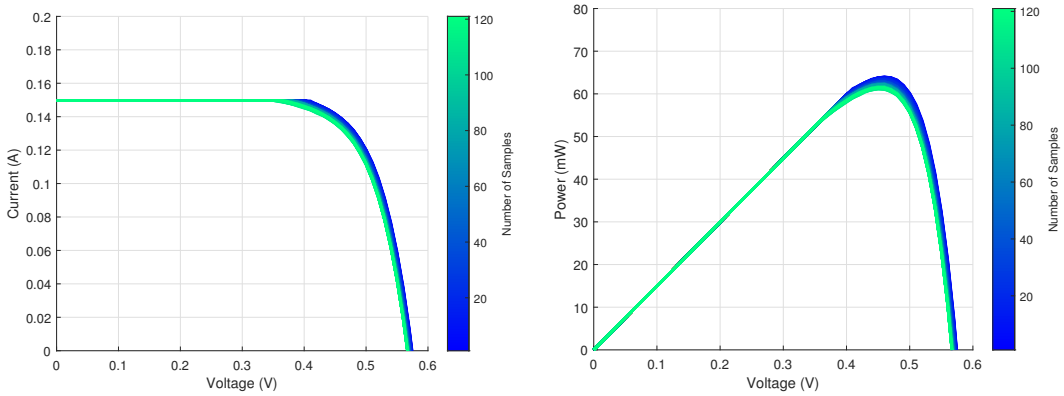



Figure 18: 950 W case: measured cell temperature at MPP.




(a) Characteristic current–voltage curves

(b) Characteristic power–voltage curves

Figure 19: 1025 W case: current–voltage and power–voltage curves from 1025 W applied to PV reference cell.

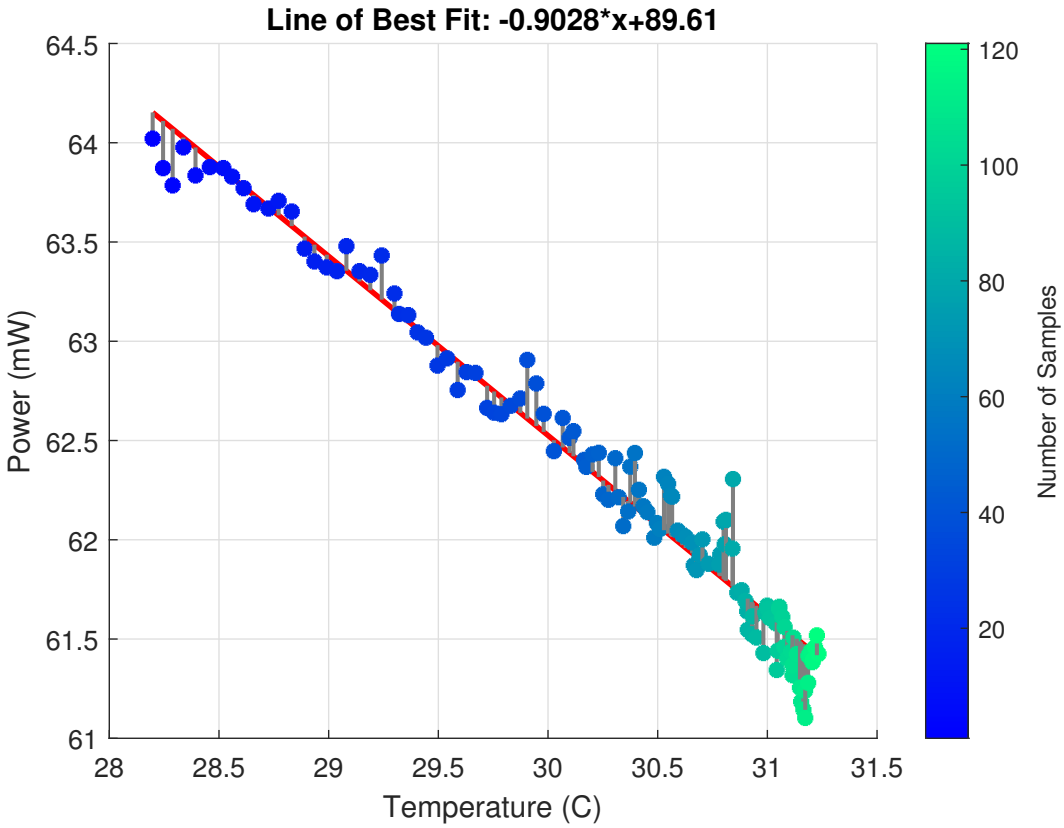


Figure 20: 1025 W case: measured cell temperature at MPP.

During irradiation, the reference cell temperature gradually increased, resulting in a corresponding decrease in cell efficiency. This temperature increase correlated with a linearly decreasing maximum power output. Variations in the distribution of data points were observed between characterizations. The 1025, 850, and 750 W characterizations exhibited a tighter distribution of sample points compared with the 950, 650, 550, 450, and 350 W characterizations. The 950 W characterization demonstrated the widest distribution and poorest fit, likely attributable to differences in variable environmental/operational conditions. The lack of precise thermal regulation in the experimental environment contributed to these variations, limiting the ability to maintain consistent testing conditions.

## 3.2 Energy and Power Characterizations

Data from the 950 and 1025 W voltage and current characterizations will be used to develop energy and power characterizations and inform the development of a thermal model for the PV reference cell. The laboratory ambient temperature was estimated to be approximately 28.5 °C, based on the initial cell temperatures recorded in Figures 18 and 20. This temperature was within 25% of standard test conditions; therefore, the approximation may have limited accuracy. Supplying 1000 W to the arc lamp was expected to produce an irradiance of 1 sun, equivalent to 1000 W/m$^2$. Consequently, 1025 W input corresponded to an irradiance of 1025 and 950 W input corresponds to 950 W.

Analysis of the current–voltage curves for the 1025 and 950 W characterizations yielded mean open-circuit voltages ($V_{oc}$) of 0.5693 and 0.5682 V, and mean short-circuit currents ($I_{sc}$) of 0.1496 and 0.1436 A, respectively. Interpolation of these values estimates $V_{oc}$ and $I_{sc}$ at 1000 W/m$^2$ to be 0.5690 V and 0.1476 A.

The mean temperature coefficients for $V_{oc}$ were −0.46 %/°C and −0.48 %/°C, while those for $I_{sc}$ were 1.49 %/°C and 0.75 %/°C. Interpolation provides temperature coefficient estimates of $\alpha_{V_{oc}} = -0.47$ %/°C and $\alpha_{I_{sc}} = 0.26$ %/°C at 1000 W/m$^2$.

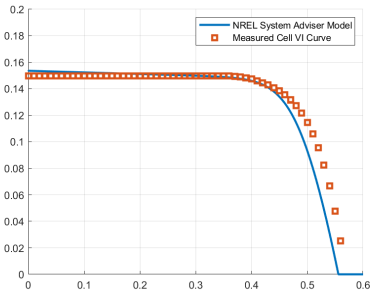
The mean voltage ($V_{mp}$) and current ($I_{mp}$) at maximum power were 0.4500 $V$ and 0.1384 $A$ at 1025 W, and 0.4550 V and 0.1254 A at 950 W. Interpolation estimates $V_{mp}$ and $I_{mp}$ at 1000 W/m$^2$ to be 0.4517 V and 0.1340 A.

Finally, the mean maximum power ($P_{max}$) was 62.3 and 57.0 mW, with interpolation estimating $P_{max}$ at 1000 W/m$^2$ to be 60.5 mW. These parameters characterizing the PV reference cell are summarized in Table 5.

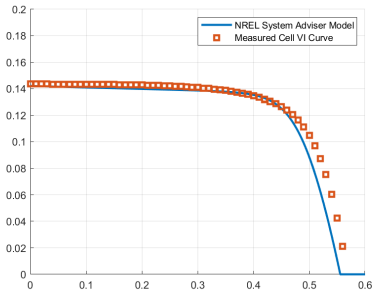
Table 5: Approximate PV reference cell parameters.

| Description | Variable | Value | Units |
|---|---|---|---|
| Maximum power | $P_{max}$ | 60.5 | mW |
| Open circuit voltage | $V_{oc}$ | 0.5690 | $V$ |
| Short circuit current | $I_{sc}$ | 0.1476 | A |
| Voltage at MPP | $V_{mp}$ | 0.4517 | V |
| Current at MPP | $I_{mp}$ | 0.1340 | A |
| Temperature coefficient at $V_{oc}$ | $\alpha_{V_{oc}}$ | $-0.47$ | $\%/^{o}$C |
| Temperature coefficient at $I_{sc}$ | $\alpha_{I_{sc}}$ | 0.26 | $\%/^{o}$C |
| No. cells per module | $N_{cell}$ | 1 | # |
| No. series string | $N_{ser}$ | 1 | # |
| No. parallel string | $N_{par}$ | 1 | # |

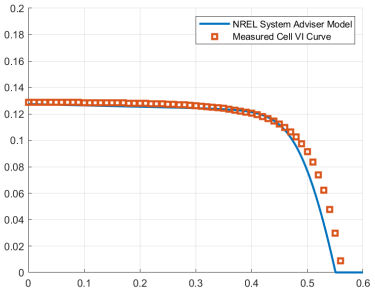
Using the PV Array block from MATLAB/Simulink[13] (which is based on the National Renewable Energy Laboratory System Advisor Model [2018]) in combination with the approximated PV reference cell parameters, the mathematical model may be configured and simulated. The simulated results were then compared with the measured current–voltage and power–voltage curves obtained, as shown in Figures 21 and 22.



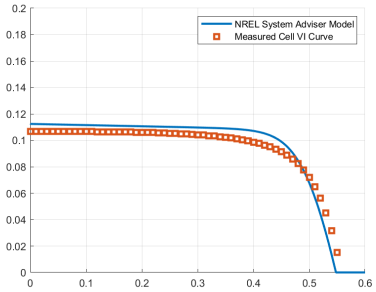

(a) 1025 W/m$^2$



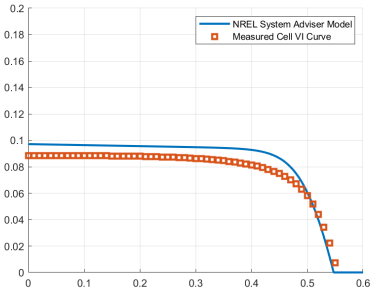

(b) 950 W/m$^2$



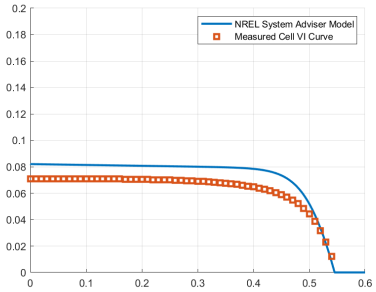

(c) 850 W/m$^2$



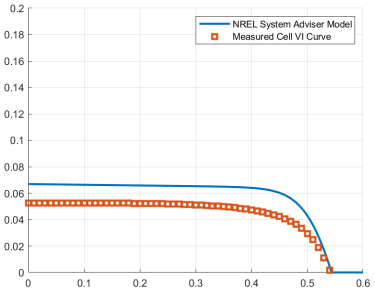

(d) 750 W/m$^2$



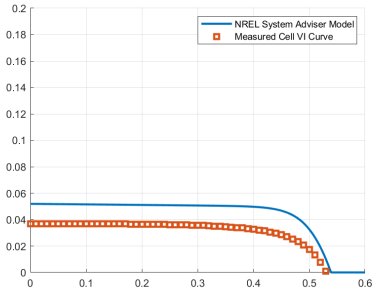

(e) 650 W/m$^2$




(f) 550 W/m$^2$

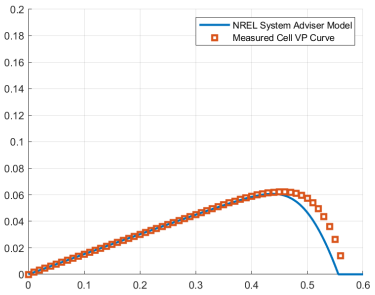



(g) 450 W/m$^2$

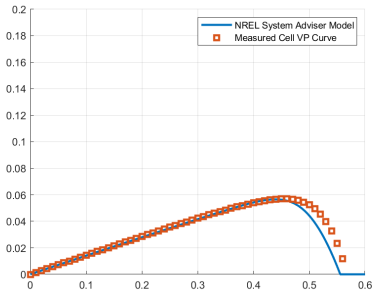



(h) 350 W/m$^2$

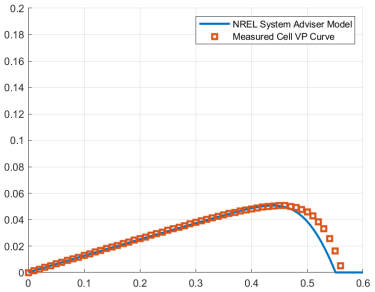
Figure 21: A comparison between the manufacturer data sheet representative voltage–current (current–voltage) curves compared with the configured Simulink subject to an irradiance ranging from 1025 to 350 W/m$^2$.



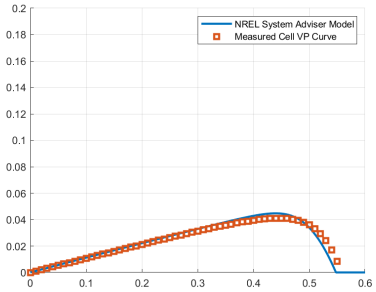

(a) 1025 W/m$^2$



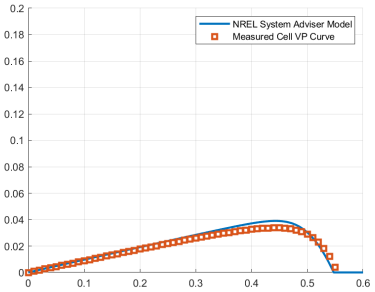

(b) 950 W/m$^2$



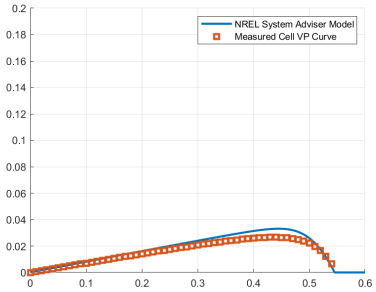

(c) 850 W/m$^2$



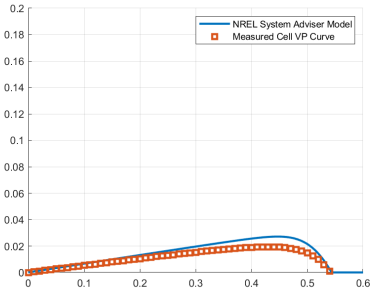

(d) 750 W/m$^2$



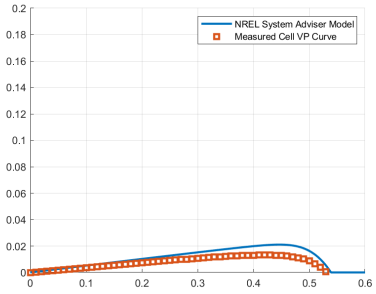

(e) 650 W/m$^2$




(f) 550 W/m$^2$




(g) 450 W/m$^2$




(h) 350 W/m$^2$

Figure 22: A comparison between the manufacturer data sheet representative voltage–power (power–voltage) curves compared with the configured Simulink subject to an irradiance ranging from 1025 to 350 W/m$^2$.

Analysis of Figures 21 and 22 indicates the approximated PV reference cell parameters adequately model performance at irradiance levels from 1025 to 650 W/m$^2$. However, the model underpredicts performance at lower irradiance levels. This degradation is likely attributable to the model's sensitivity to series and shunt resistance and to limitations in measurement and machine precision. At lower irradiance, series resistance exerts a more significant impact on power output, while shunt resistance becomes proportionally more influential. Furthermore, reduced measurement precision can propagate errors into parameter approximations, particularly affecting temperature coefficients for open-circuit voltage and short-circuit current. Standard test conditions specify an air mass of 1.5 and an ambient temperature of 25 °C when determining these constants. Air mass and average ambient temperature were not recorded during testing, which spanned multiple days with varying temperature conditions. Further investigation is required to fully elucidate the mechanisms underlying the model's performance limitations.

## 3.3 Summary

A predictive mathematical model of PV reference cell performance was developed through combined current–voltage and power–voltage characterizations. A detailed current–voltage analysis, using a Newport arc lamp solar simulator across an irradiance range of 350 to 1025 W, generated a robust dataset of current–voltage curves via a repeatable measurement routine with controlled irradiation and voltage sweeps. This dataset was then leveraged to derive key parameters (including open-circuit voltage, short-circuit current, maximum power point, and temperature coefficients) for energy and power characterization and subsequent model configuration within MATLAB/Simulink.

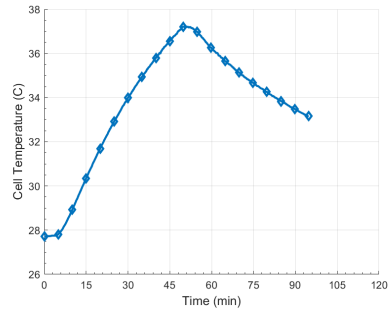
The resulting model demonstrated strong agreement with measured performance at higher irradiance levels but underpredicted performance at lower levels. This discrepancy is likely due to the increased influence of series and shunt resistance and limitations in measurement precision. While providing a valuable foundation for predicting PV reference cell behavior, further investigation is required to refine the model's accuracy, particularly at lower irradiance levels, and to fully account for environmental factors and machine precision.

## 4. Thermal Characterizations

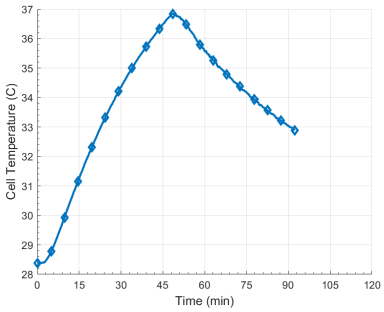
The same arc lamp class AAA solar simulator manufactured by Newport was once again used for temperature characterization of the PV reference cell. While the arc lamp is traditionally controlled and regulated using the Oriel instrumentation software package through the creation of a recipe, the thermal characterization did not use one. As was done previously, the arc lamp was regulated and controlled to operate at a fixed rated power level.

At this point the arc lamp aperture was opened, thus irradiating the PV reference cell. The aperture remained open for approximately 45 min. During this period, the PV thermal reference cell voltage remained unregulated or modulated. This effectively enabled the PV thermal reference cell to be continuously irradiated with a known irradiance value for a fixed period, enabling energy from the arc lamp to be transferred to the PV reference cell, thus increasing the cell temperature. The aperture was closed after 45 min had passed. The PV reference cell was then permitted to rest for approximately 45 min, during which time the PV reference cell thermal temperature was allowed to decay toward the ambient conditions.

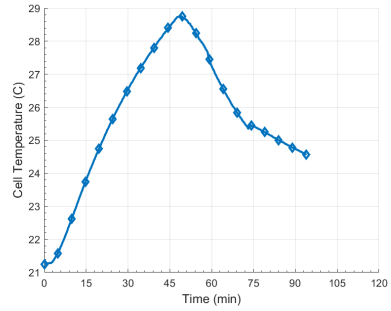
The reference cell was subjected to 350 W, (Figure 23h), 450 W (Figure 23g), 550 W (Figure 23f), 650 W (Figure 23e), 750 W (Figure 23d), 850 W (Figure 23c), 950 W (Figure 23b), and 1025 W (Figure 23a). The solar cell was not regulated during the irradiation, enabling the reference cell's thermal behavior to perhaps be characterized as a function of time, ignoring energy generation.



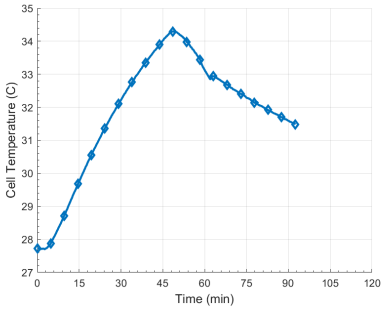

(a) 1025 W/m$^2$



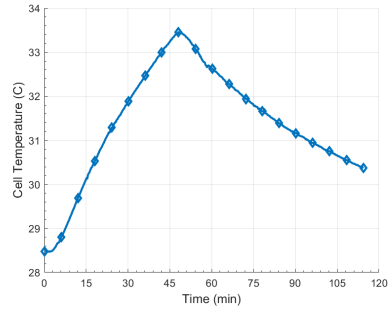

(b) 950 W/m$^2$



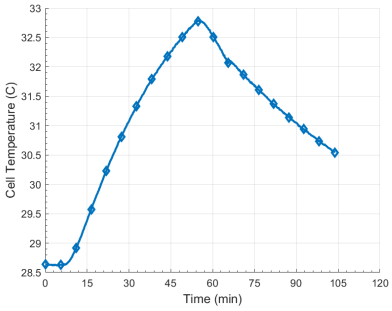

(c) 850 W/m$^2$



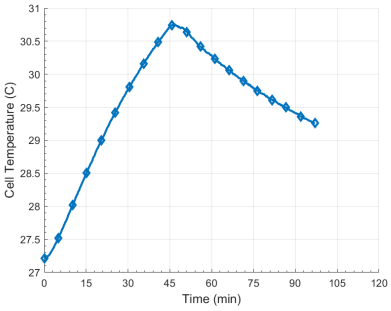

(d) 750 W/m$^2$



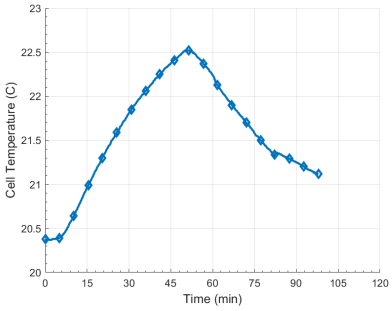

(e) 650 W/m$^2$




(f) 550 W/m$^2$




(g) 450 W/m$^2$



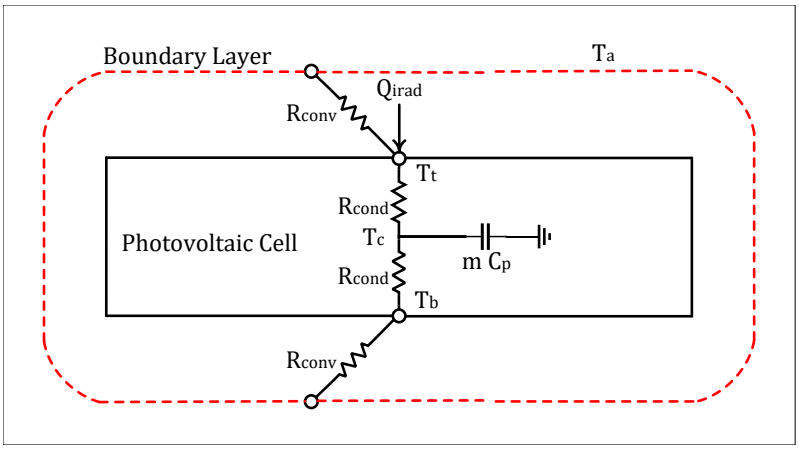

(h) 350 W/m$^2$

Figure 23: Measured cell temperature, subjected to an irradiance ranging from 1025 to 350 W/m$^2$.

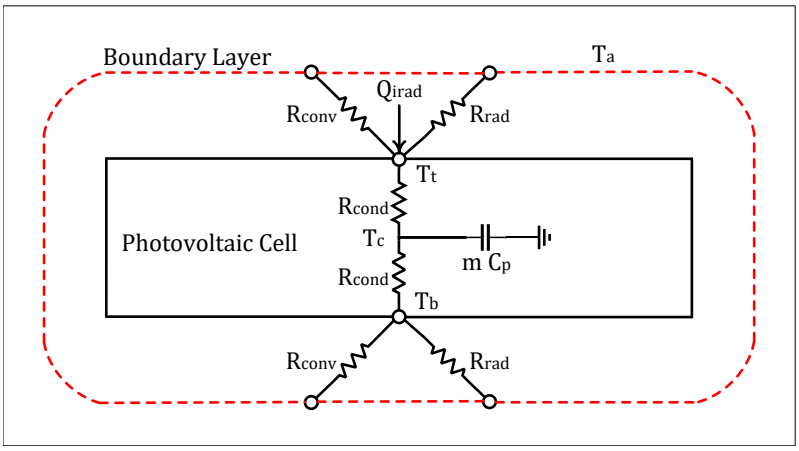
For all observed thermal characterizations, the thermal reference cell's temperature increases nonlinearly with respect to time while irradiated. It similarly decreases nonlinearly with respect to time after the aperture was closed, allowing the thermal reference cell to naturally decay toward the ambient conditions. Larger temperature differences were observed when the arc lamp was subjected to increased power levels. The nonlinear increase and decrease appear to loosely follow a characteristic first order exponential response, consistent with typical 1D heat and mass transfer principles.

Interestingly, multiple thermal characterizations responses of the PV reference cell exhibited sustained and clear perturbations, leading to multiple different thermal decay rates. This can be observed upon inspection of the thermal characterization 850 W (Figure 23c), 750 W (Figure 23d), and 350 W (Figure 23h). It is believed that this behavior caused forced fluid flow convection resulting from the cooling apparatus of the lamp or bulb and possibly a reduction of resistance encountered within the Data AcQuisition caused by disabling an analog display monitoring the cell temperature.

Using the PV reference cell thermal characterization time series data, two lumped parameter 1D thermal models were defined as shown in Figure 24. The only difference between the thermal models includes the presence of radiation heat transfer terms for both top and bottom surfaces of PV reference cell. For production PV modules, the bottom surface often incorporates a low-emissivity layer used to minimize heat loss, while the top surface maintains high emissivity to maximize energy absorption.




(a) Model A




(b) Model B

Figure 24: Lumped parameter 1D thermal models postulated for approximating the thermal behavior of the PV reference cell.

In accordance with 1D heat transfer mechanics, conduction heat transfer is governed by Equation 1:

$$Q_{cond} = R_{cond}\,(T_1 - T_2) \tag{1}$$

where $R_{cond}$ represents the conduction thermal resistance, $T_1$ and $T_2$ represent the temperatures of respective surfaces or planes, and $Q_{cond}$ represents the heat flow resulting from conduction. The conduction thermal resistance is then defined as shown in Equation 2:

$$R_{cond} = \frac{k \cdot A}{t} \tag{2}$$

where $k$ represents the thermal conductivity, $A$ represents the surface area, and $t$ represents the material thickness. Convection heat transfer is then governed by Equation 3:

$$Q_{conv} = R_{conv} \left(T_1 - T_2\right) \tag{3}$$

where $R_{conv}$ represents the convective thermal resistance and $Q_{conv}$ represents the heat flow resulting from convection. The convection thermal resistance is then defined as shown in Equation 4:

$$R_{conv} = h \cdot A \tag{4}$$

where $h$ represents the heat transfer coefficient. Radiation heat transfer is then governed by Equation 5:

$$Q_{rad} = R_{rad} \left(T_1^4 - T_2^4\right) \tag{5}$$

where $R_{rad}$ represents the radiation thermal resistance and $Q_{rad}$ represents the heat flow resulting from radiation. The radiation thermal resistance is then defined as shown in Equation 6:

$$R_{rad} = \epsilon \cdot \sigma \cdot A \tag{6}$$

where $\epsilon$ represents the emissivity and $\sigma$ represents the Stefan–Boltzmann. From analysis of the lumped parameter thermal models as seen in Figure 24, it can be inferred that the thermal network can be modeled by a single differential equation in the form of Equation 7:

$$m \cdot C_p \cdot \frac{dT_c}{dt} = R_{cond} \cdot (T_t - T_c) + R_{cond} \cdot (T_b - T_c) \tag{7}$$

where $m$ represents the mass, $C_p$ represents the average specific heat, $T_c$ represents the cell temperature, and $T_t$ and $T_b$ represent the top and bottom surface temperatures of the cell, respectively. To simulate the lumped parameter thermal model, the intermediate temperature values of $T_t$ and $T_b$ need to be computed, which vary based on Thermal Model A or B. To achieve this, nodal analysis is completed around each of the two nodes, leading to Equations 8 and 9, which are only applicable to Thermal Model A:

$$R_{cond}\,(T_c - T_t) = R_{conv}\,(T_t - T_a) + Q_{irad} \tag{8}$$

$$R_{cond}\,(T_c - T_b) = R_{conv}\,(T_b - T_a) \tag{9}$$

while Equations 10 and 11 are applicable to Thermal Model B:

$$R_{cond}\,(T_c - T_t) = R_{conv}\,(T_t - T_a) + R_{rad}\left(T_t^4 - T_a^4\right) + Q_{irad} \tag{10}$$

$$R_{cond}\,(T_c - T_b) = R_{conv}\,(T_b - T_a) + R_{rad}\left(T_b^4 - T_a^4\right) \tag{11}$$

Within the previous equations, $Q_{irad}$ represents the power delivered via a light source, which is approximated as Equation 12, where $G_a$ represents the solar irradiation:

$$Q_{irad} = A \cdot G_a \tag{12}$$

Equations 8 and 9 or 10 and 11 can be solved symbolically using either MATLAB/Simulink or Wolfram Mathematic. An LLM was used to construct a c-coded

Runge–Kutta integration schema capable of solving the differential equation, as defined in Equation 7. Alternatively, MATLAB's ode45 could be used to solve the differential system of equations. Information gathered from the manufacturer indicated that the PV reference cell physical parameters are defined as shown in Table 6.

Table 6: Approximate PV reference cell physical parameters.

| Description | Variable | Value | Units |
|---|---|---|---|
| Length | $L$ | 2 | cm |
| Width | $W$ | 2 | cm |
| Area | $A$ | 4 | $cm^2$ |
| Thickness | $t$ | 190 | $\mu$m |

## 4.1 Thermal Model A Characterizations

The thermal capacitance, thermal conductivity, and heat transfer coefficient are unknown parameters for this model. However, these parameters can be approximated using a global optimization routine, specifically a genetic algorithm (GA). Employing the differential equation (Equation 7) in conjunction with Equations 8 and 9 and the GA optimization routine, approximate thermal constants for the thermal reference cell were determined. Thermal capacitance and conductivity represent inherent physical properties of the PV reference cell and are therefore assumed to remain constant regardless of operating conditions. Conversely, the heat transfer coefficient is expected to vary based on operational factors such as airflow and ambient temperature.

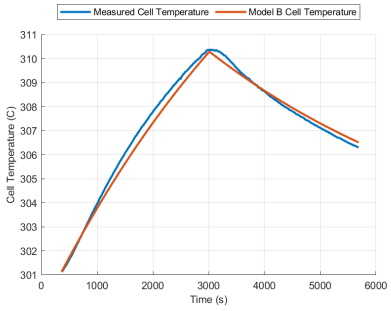
The solution to the differential equations that resulted in the minimum mean squared rror (MSE) between the measured and modeled cell temperature includes the physical constants as shown in Table 7, which ultimately results in the comparison between the measured and approximated cell temperature profiles provided in Figure 25.

Analysis of the thermal profiles (Figure 25) indicates the thermal model accurately approximates thermal reference cell temperatures for three of the five simulated irradiance levels: 1025, 950, and 450 $W/m^2$. Greater discrepancies were observed at 650 and 550 $W/m^2$, likely due to the ambient temperature variations encountered

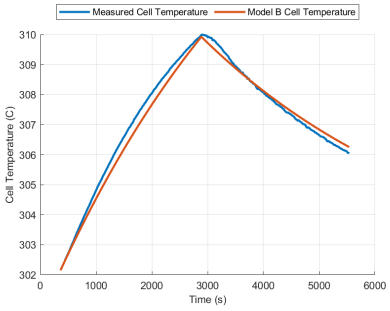
during testing. Future studies will incorporate ambient temperature measurement to mitigate this uncertainty. Furthermore, the model consistently fails to capture the dynamic thermal response observed during irradiance transitions—specifically, the lag between full irradiance and complete obstruction that happens nearly instantaneously. This suggests an missing dynamic component within the model and indicates the presence of additional, currently unmodeled, dynamic thermal characteristics. It can also be observed that the model is incomplete because at lower irradiance values, the heat transfer coefficient has converged toward $25\frac{W}{m^2 \cdot K}$, which was the upper limit imposed on the GA assumed to be an approximate limit for the free convective heat transfer coefficient. Larger heat transfer coefficients are typically more indicative of forced heat transfer. Additionally, the thermal conductivity converged toward $0.05\frac{W}{m \cdot K}$, which was the lower limit imposed on the GA.

Table 7: Approximate PV reference cell Thermal Model A thermal constant parameters.

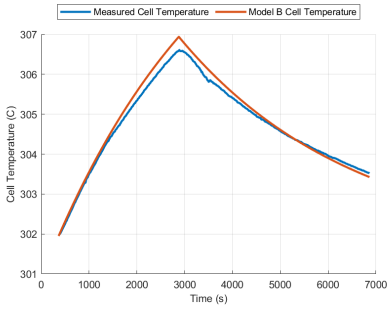
| Description | Variable | Value | Units |
|---|---|---|---|
| Thermal capacitance | $m \cdot C_p$ | 94.1460 | $\frac{J}{K}$ |
| Thermal conductivity | $k$ | 0.0500 | $\frac{W}{m \cdot K}$ |
| Heat transfer coefficient at 1025 W/m$^2$ | $h$ | 20.0972 | $\frac{W}{m^2 \cdot K}$ |
| Heat transfer coefficient at 950 W/m$^2$ | $h$ | 23.0606 | $\frac{W}{m^2 \cdot K}$ |
| Heat transfer coefficient at 650 W/m$^2$ | $h$ | 25.0000 | $\frac{W}{m^2 \cdot K}$ |
| Heat transfer coefficient at 550 W/m$^2$ | $h$ | 25.0000 | $\frac{W}{m^2 \cdot K}$ |
| Heat transfer coefficient at 450 W/m$^2$ | $h$ | 25.0000 | $\frac{W}{m^2 \cdot K}$ |



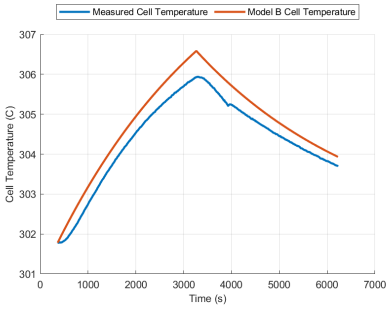

(a) 1025 W/m$^2$



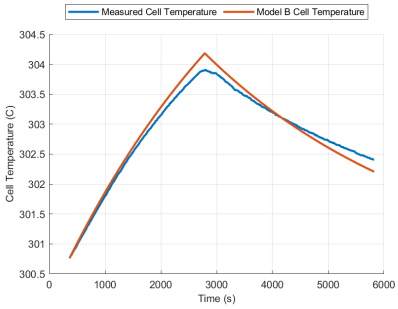

(b) 950 W/m$^2$




(c) 650 W/m$^2$




(d) 550 W/m$^2$




(e) 450 W/m$^2$

Figure 25: A comparison between the measured and approximated cell temperature, subjected to an irradiance of 1025, 950, 650, 550, or 450 W/m$^2$ and Thermal Model A.

## 4.2 Thermal Model B Characterizations

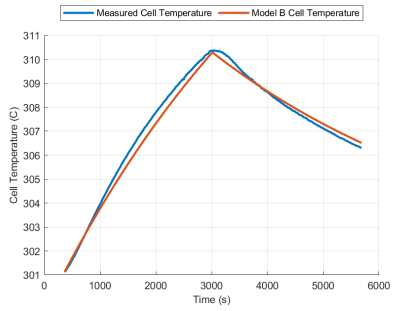
The thermal capacitance, thermal conductivity, surface emissivity, and heat transfer coefficient are unknown parameters for this model. These parameters can again be approximated using GA. Employing the differential equation (Equation 7) in conjunction with Equations 10 and 11 and the GA optimization routine, approximate thermal constants for the thermal reference cell were determined. While thermal capacitance, thermal conductivity, and surface emissivity are assumed to remain constant under varying operating conditions, the heat transfer coefficient is expected to fluctuate. This assumption aligns with typical PV cell design, where the bottom surface often incorporates a low-emissivity plastic layer to minimize heat loss, while the top surface maintains high emissivity to maximize energy absorption.

Table 8: Approximate PV reference cell Thermal Model B thermal constant parameters.

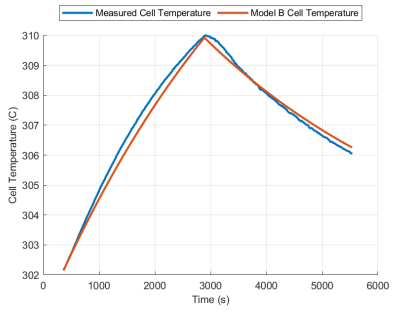
| Description | Variable | Value | Units |
|---|---|---|---|
| Thermal capacitance | $m \cdot C_p$ | 91.9156 | $\frac{J}{K}$ |
| Thermal conductivity | $k$ | 56.6691 | $\frac{W}{m \cdot K}$ |
| Top surface emissivity | $\epsilon_t$ | 0.9897 | ... |
| Bottom surface emissivity | $\epsilon_b$ | 0.9894 | ... |
| Heat transfer coefficient at 1025 W/m$^2$ | $h$ | 15.6593 | $\frac{W}{m^2 \cdot K}$ |
| Heat transfer coefficient at 950 W/m$^2$ | $h$ | 18.5891 | $\frac{W}{m^2 \cdot K}$ |
| Heat transfer coefficient at 650 W/m$^2$ | $h$ | 24.9992 | $\frac{W}{m^2 \cdot K}$ |
| Heat transfer coefficient at 550 W/m$^2$ | $h$ | 24.9937 | $\frac{W}{m^2 \cdot K}$ |
| Heat transfer coefficient at 450 W/m$^2$ | $h$ | 21.4023 | $\frac{W}{m^2 \cdot K}$ |

The approximate thermal constants representing the thermal reference cell were determined by employing the differential equation (Equation 7) in conjunction with Equations 10 and 11 and a GA optimization routine. Thermal capacitance, thermal conductivity, and top and bottom surface emissivity are assumed to remain constant, as these represent inherent physical properties of the PV reference cell. However, the heat transfer coefficient is expected to vary with operating conditions, specifically airflow and ambient temperature.

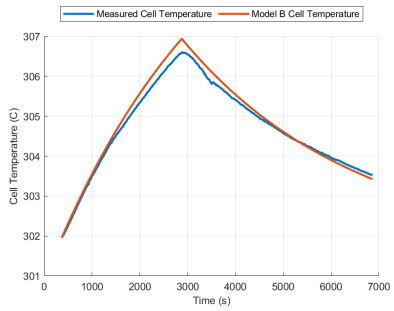
The solution to the differential equations that resulted in the minimum MSE error between the measured and modeled cell temperature includes the physical constants as shown in Table 8, which ultimately results in the comparison between the measured and approximated cell temperature profiles shown in Figure 26.



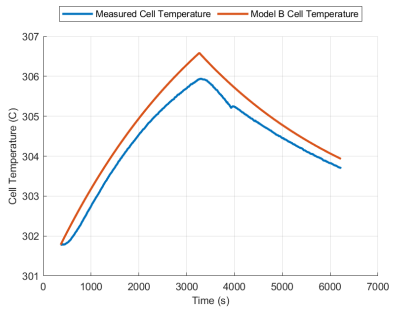

(a) 1025 W/m$^2$



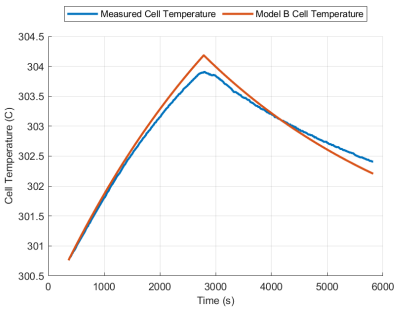

(b) 950 W/m$^2$




(c) 650 W/m$^2$




(d) 550 W/m$^2$




(e) 450 W/m$^2$

Figure 26: A comparison between the measured and approximated cell temperature, subjected to an irradiance of 1025, 950, 650, 550, or 450 W/m$^2$ and Thermal Model B.

Analysis of the thermal profiles (Figure 26) indicates the thermal model accurately approximates thermal reference cell temperatures for four of the five simulated

irradiance levels: 1025, 950, 650, and 450 W/m$^2$. Greater discrepancies were observed at 550 W/m$^2$, likely due to unmonitored ambient temperature variations during testing. This alternative model consistently fails to capture the dynamic thermal response observed during irradiance transitions—specifically, the lag between full irradiance and complete obstruction. This again suggests an incomplete dynamic component within the model and indicates the presence of additional, currently unmodeled, dynamic thermal characteristics. The top and bottom emissivity values are nearly identical and indicate that there is minimal difference between the top and bottom surface, indicating the PV reference cell does not possess the bottom surface protective coating aimed to reduce heat loss within the test cell, assuming Thermal Model B is an accurate lumped parameter thermal model for the PV reference cell.

## 4.3 Summary

Thus, Thermal Model B is better for approximating the thermal characteristics of the PV reference cell as opposed to Thermal Model A. The computed thermal constants represent approximately lumped parameters that produce characteristic thermal behavior when compared with the measured PV reference cell. The mass of PV reference cells is unknown and the PV reference cell itself is contained within an all-in-one assembly that contains a thermal couple measurement leads that is compatible with the solar simulator. As a result, the measuring of the PV reference cell temperature in this way may not be accurately characterized by the PV reference cell. To understand if this is the case or not, the PV reference cell would need to be removed from the assembly and tested with the absence of the full assembly while still maintaining the ability to measure the cell temperature. The applied model still fails to accurately portray the dynamic thermal response observed during irradiance transitions, and it is speculated that this dynamic can partly be attributed to a nonconstant ambient temperature and primarily attributed to the absence of additional differential equations aimed at approximating the dissimilar layers of material that are sandwiched together to form a singular PV cell. A more accurate thermal model of a PV array could be derived if more detailed information from the manufacturer were known, which unfortunately limits the usefulness of the thermal model.

To improve the usefulness of the model, at minimal the mass of the thermal cell must be known. If known using principles of fluid dynamics, the physical parameters could be scaled to a production grade PV cell and ultimately enable more accurate thermal predictive capabilities that could in turn improve the energy predictions. Further research is required but the work complete thus far represents an initial first step at understanding the behavior of the PV reference cell thermal characterization.

## 5. FLIR Characterizations

A FLIR camera was deployed at two distinct sites. The first site featured a PV array currently situated on an X-story building at USMA in West Point, New York. In contrast to the "near ocean" location of the USMA site, the second site contained a PV array deployed in a high desert environment. At the desert site, the FLIR camera was paired with the AIHPA Testbed, a sensor suite concurrently measuring atmospheric conditions (pressure, temperature, wind speed, and direction). The AIHPA Testbed also included a PV array, energy storage, and resistive load bank with electrical infrastructure enabling voltage and current measurements throughout the system. A back-panel temperature probe monitored the temperature of a single cell on the PV array.

The PV array located at USMA consisted of six individual PV modules; each module contained 50 cells arranged into a grid of 5 rows and 10 columns, as depicted in Figure 27. 2D array notation was used to specify individual cells, with the origin of this coordinate system assumed to be the top-left corner of the PV panel. Conversely, the PV array included within the AIHPA Testbed consisted of a single PV module featuring 72 cells arranged into a grid of 6 rows and 12 columns, as depicted in Figure 28. Using matrix notation, each cell was assigned a symbolic variable designation, $T_c(i, j)$, where $i$ represents the row number and $j$ represents the column number. This symbolic variable designation was ultimately used to extract the individual cell temperature approximations observed by the FLIR camera, which was then compared with measured temperature conditions from the local resources (AIHPA Testbed for the desert site). The remainder of this section is divided into subsections, each containing a small subset of the observed FLIR thermal responses

captured on 30 May 2024 (Section 5.1), 22 July 2024 (Section 5.2), 23 July 2024 (Section 5.3), and 25 July 2024 (Section 5.4), concluding with an analysis and assessment of the results (Section 5.5).

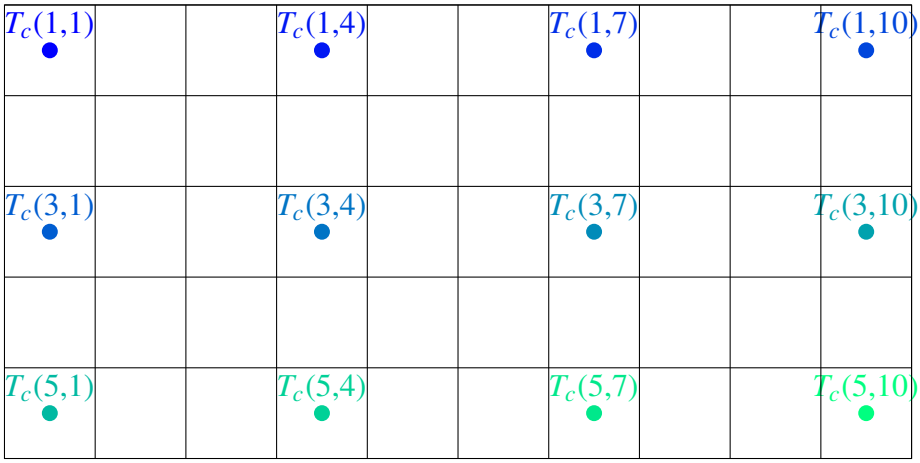


Figure 27: The approximate configuration of the PV array located on an academic building at USMA.

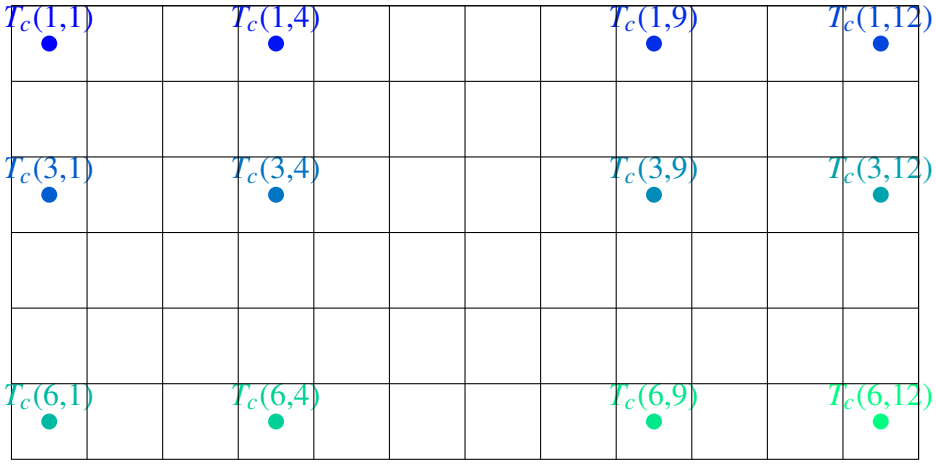
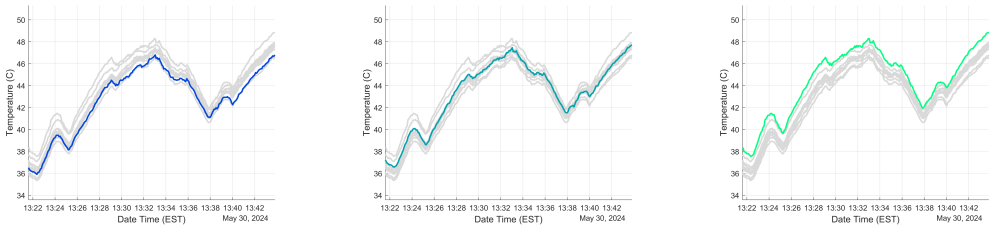


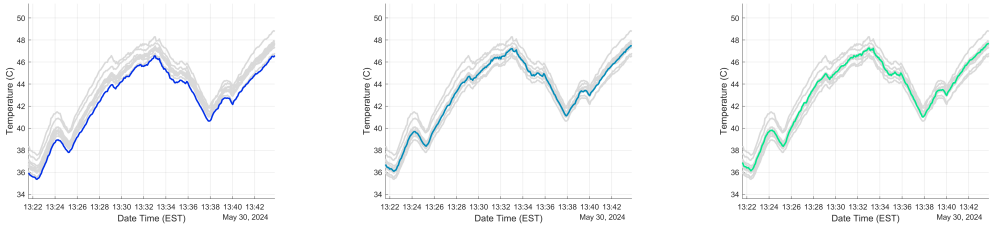
Figure 28: The approximate configuration of the PV array included within the AIHPA Testbed.

## 5.1 FLIR Characterizations for 30 May 2024

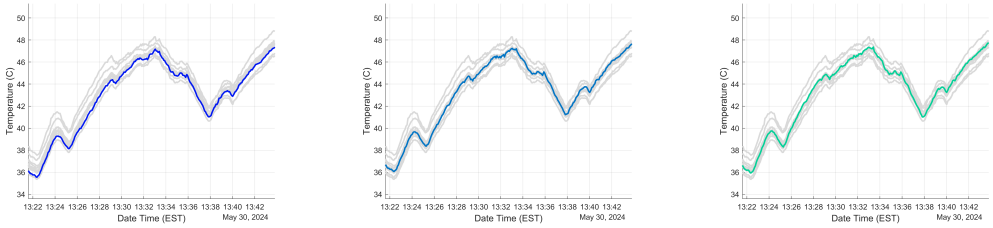
The FLIR camera was deployed to USMA for a relatively short period on 30 May 2024 from 1321 to 1343 EST. This deployment was primarily used to determine whether the FLIR camera could approximate the thermal behavior of the PV array. PV arrays use a protective lamination over the individual cells, commonly referred to as glass. While ordinary glass reflects IR radiation—meaning materials beneath it cannot normally be observed directly—IR radiation does contribute to solar irradiance. Therefore, the lamination must be transmissive to IR to some degree, a property achievable with materials like floating silica glass. The approximate time-series response of the individual cell temperatures is provided in Figure 29, which was derived from multiple sequential FLIR images. A small subset of these observed FLIR images is provided in Figures 30 and 31.



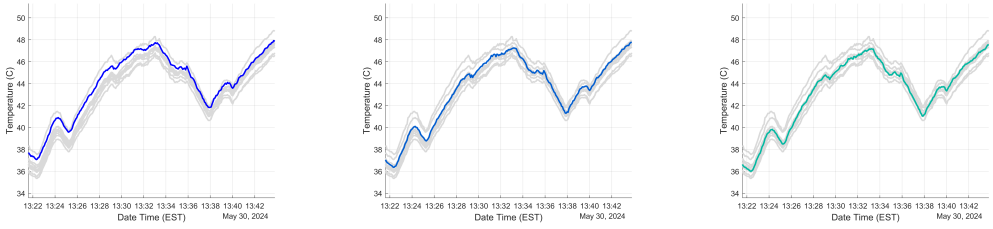

(a) $T_c(1,10)$ (b) $T_c(3,10)$ (c) $T_c(5,10)$




(d) $T_c(1,7)$ (e) $T_c(3,7)$ (f) $T_c(5,7)$




(g) $T_c(1,4)$ (h) $T_c(3,4)$ (i) $T_c(5,4)$




(j) $T_c(1,1)$ (k) $T_c(3,1)$ (l) $T_c(5,1)$

Figure 29: The observed PV panel cell temperatures obtained via the FLIR camera as deployed to USMA on 30 May 2024 from 1321 through 1343 EST.

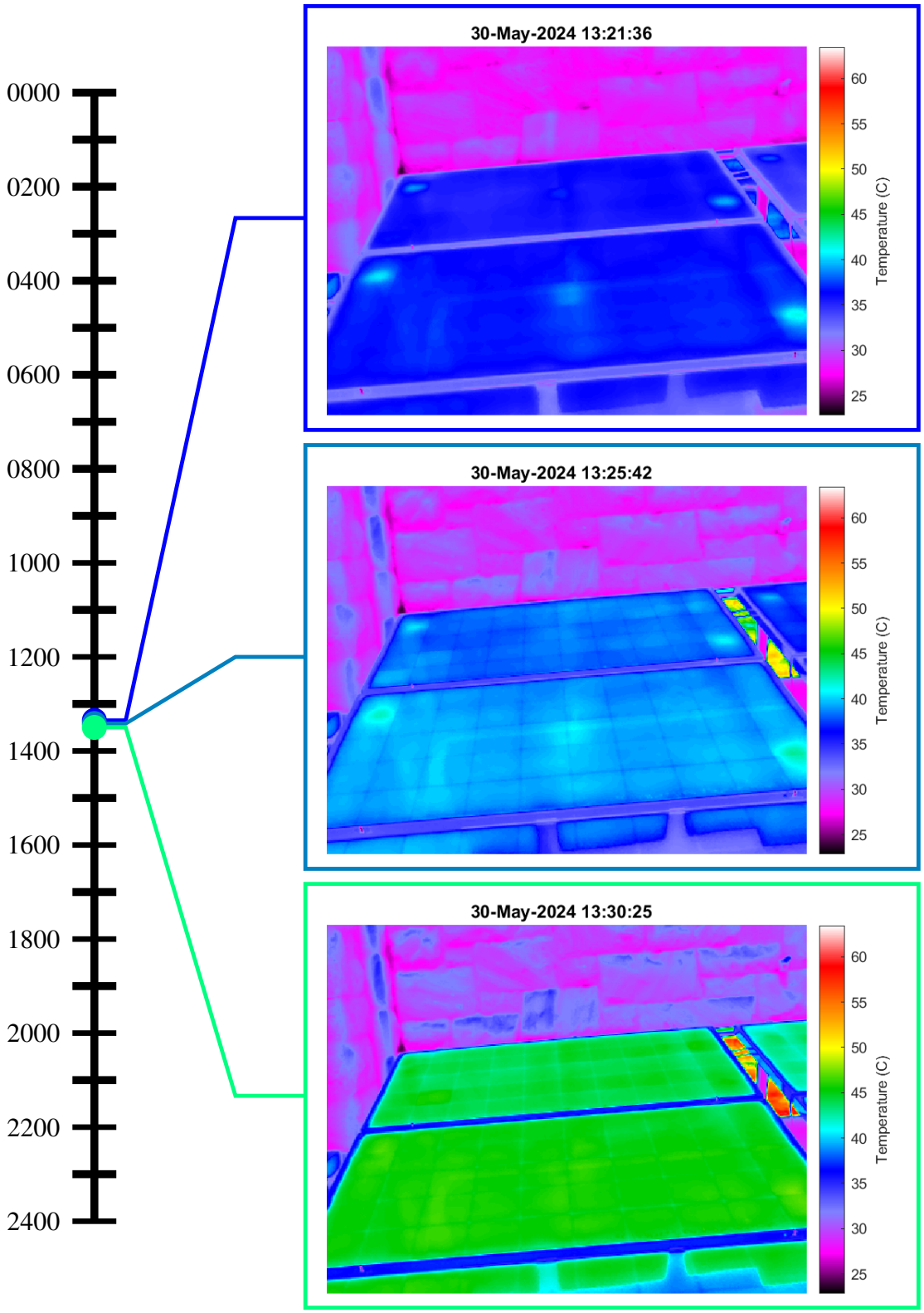



Figure 30: The observed PV panel cell temperatures obtained via the FLIR camera as deployed to AIHPA Testbed on 30 May 2024 from 1300 through 1400 EST.

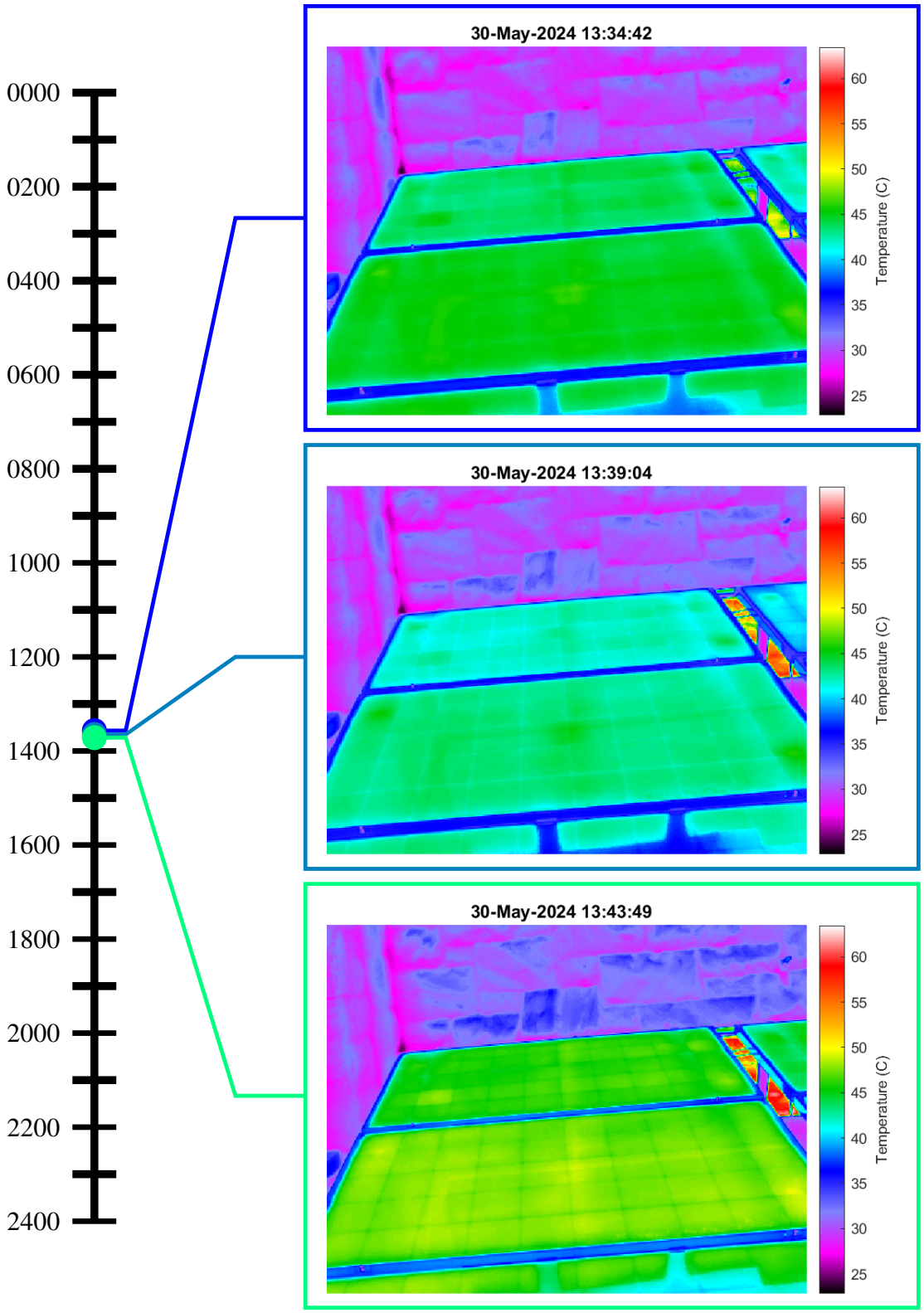
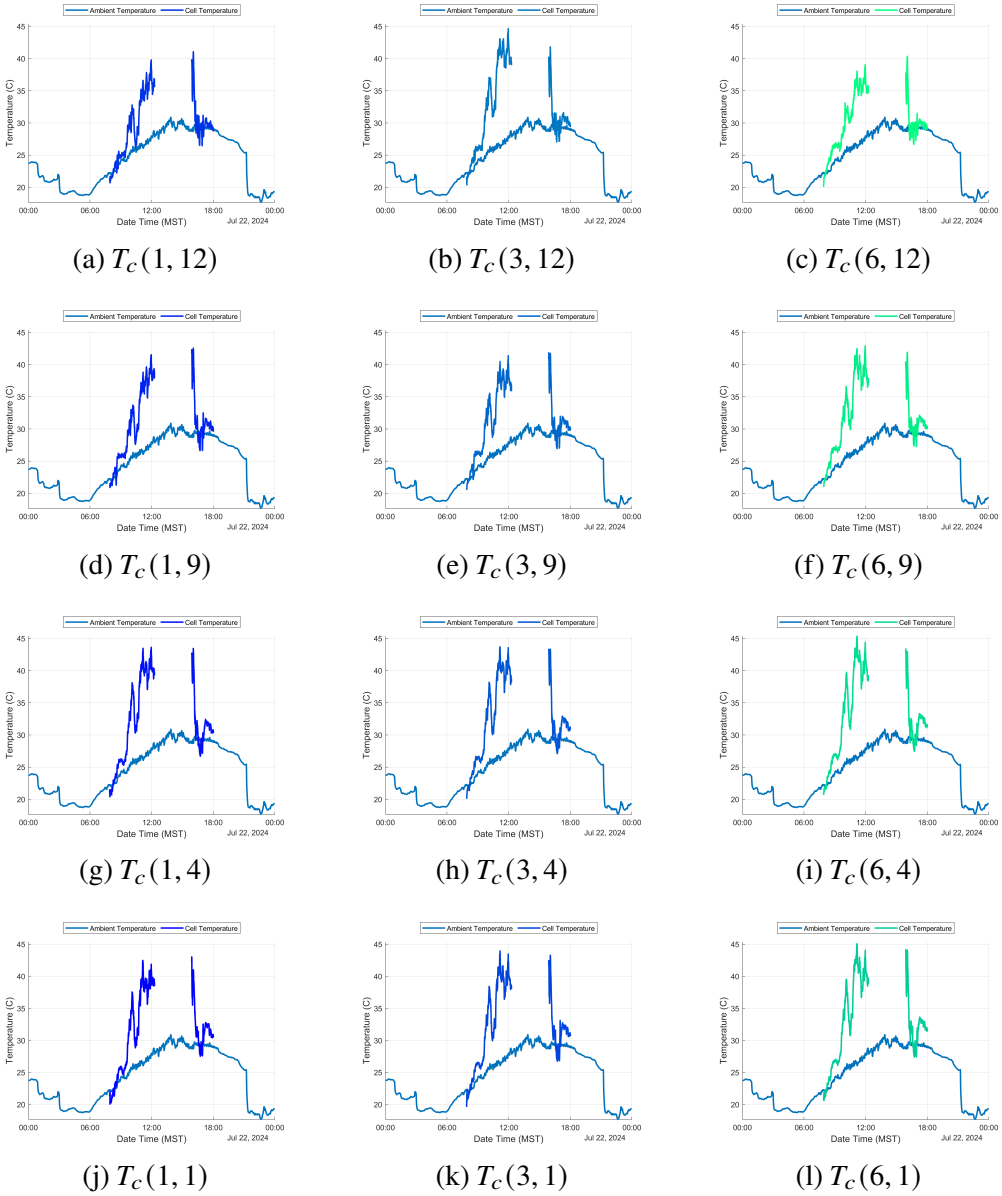



Figure 31: The observed PV panel cell temperatures obtained via the FLIR camera as deployed to AIHPA Testbed on 30 May 2024 from 1300 through 1400 EST.

## 5.2 FLIR Characterizations for 22 July 2024

The FLIR camera was deployed to the AIHPA Testbed for a relatively short period on 22 July 2024 from 0700 through 1800 MST. The approximate time-series response of the individual cell temperatures is provided in Figure 32, which was ultimately derived from multiple sequential FLIR images. A small subset of the observed FLIR images is provided in Figures 33 through 36.




(a) $T_c(1,12)$ (b) $T_c(3,12)$ (c) $T_c(6,12)$

(d) $T_c(1,9)$ (e) $T_c(3,9)$ (f) $T_c(6,9)$

(g) $T_c(1,4)$ (h) $T_c(3,4)$ (i) $T_c(6,4)$

(j) $T_c(1,1)$ (k) $T_c(3,1)$ (l) $T_c(6,1)$

Figure 32: The observed PV panel cell temperatures obtained via the FLIR camera as deployed to AIHPA Testbed on 22 July 2024 from 0700 through 1800 MST.

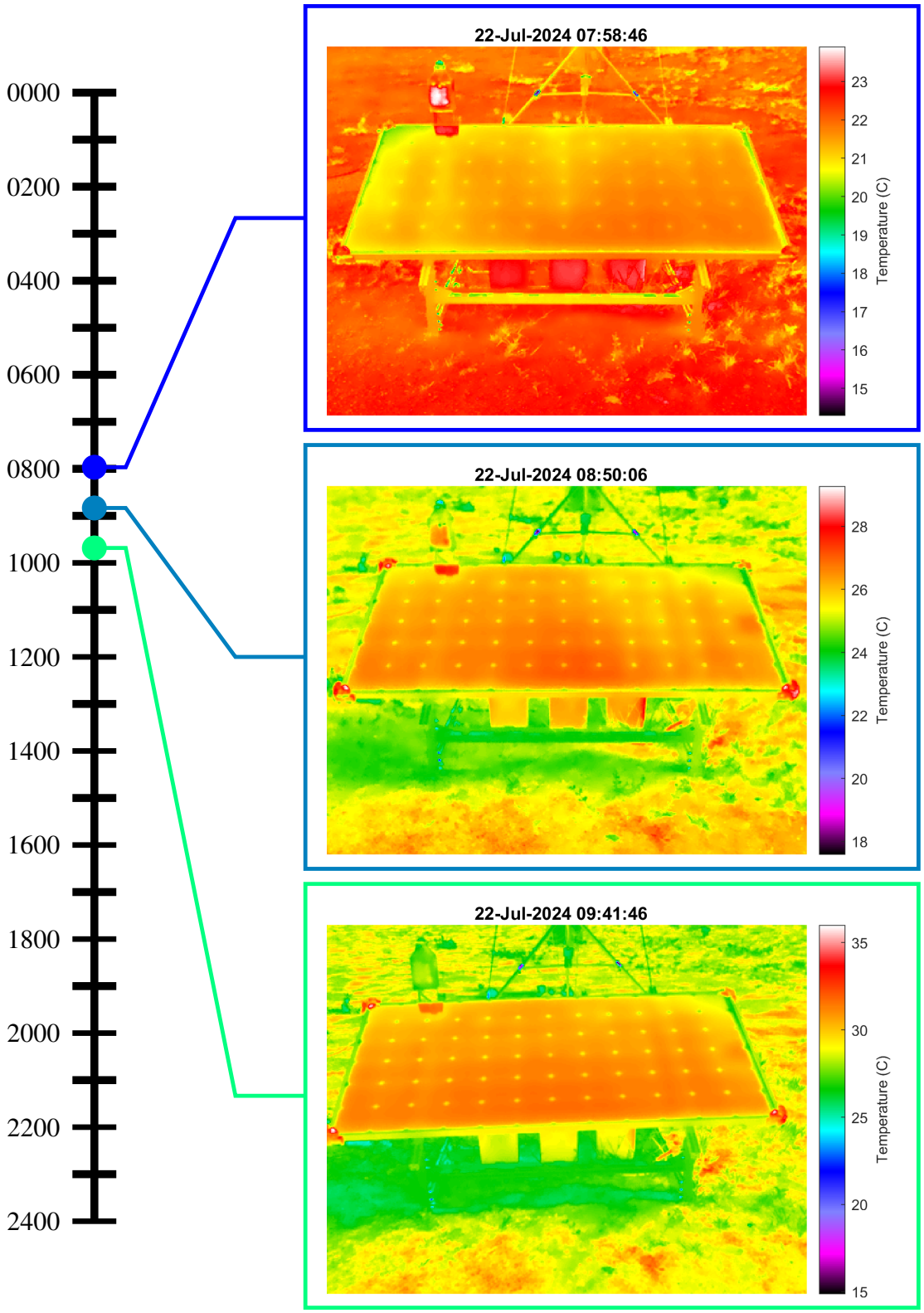



Figure 33: The observed PV panel cell temperatures obtained via the FLIR camera as deployed to AIHPA Testbed on 22 July 2024 from 0700 through 1800 MST.

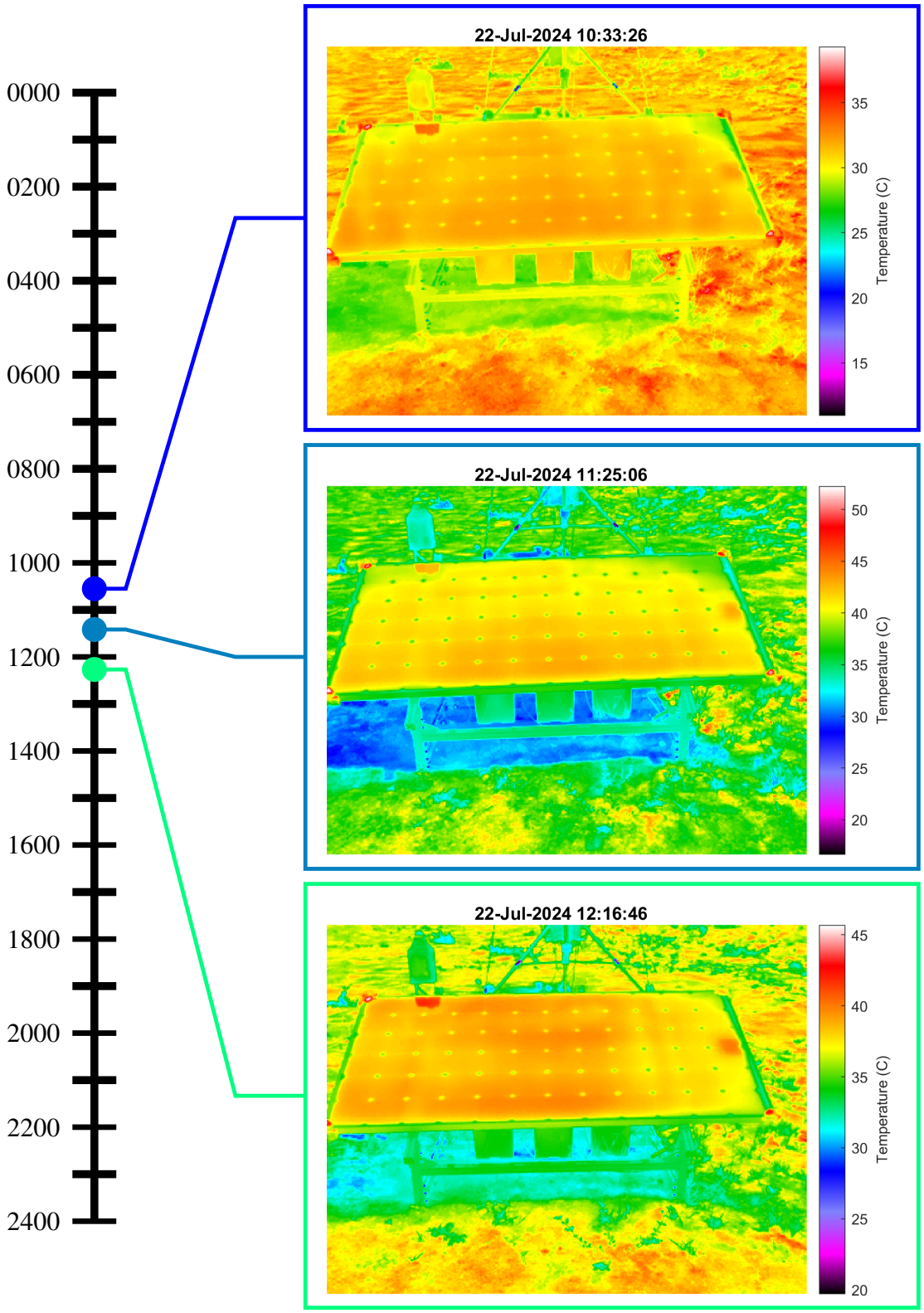



Figure 34: The observed PV panel cell temperatures obtained via the FLIR camera as deployed to AIHPA Testbed on 22 July 2024 from 0700 through 1800 MST.

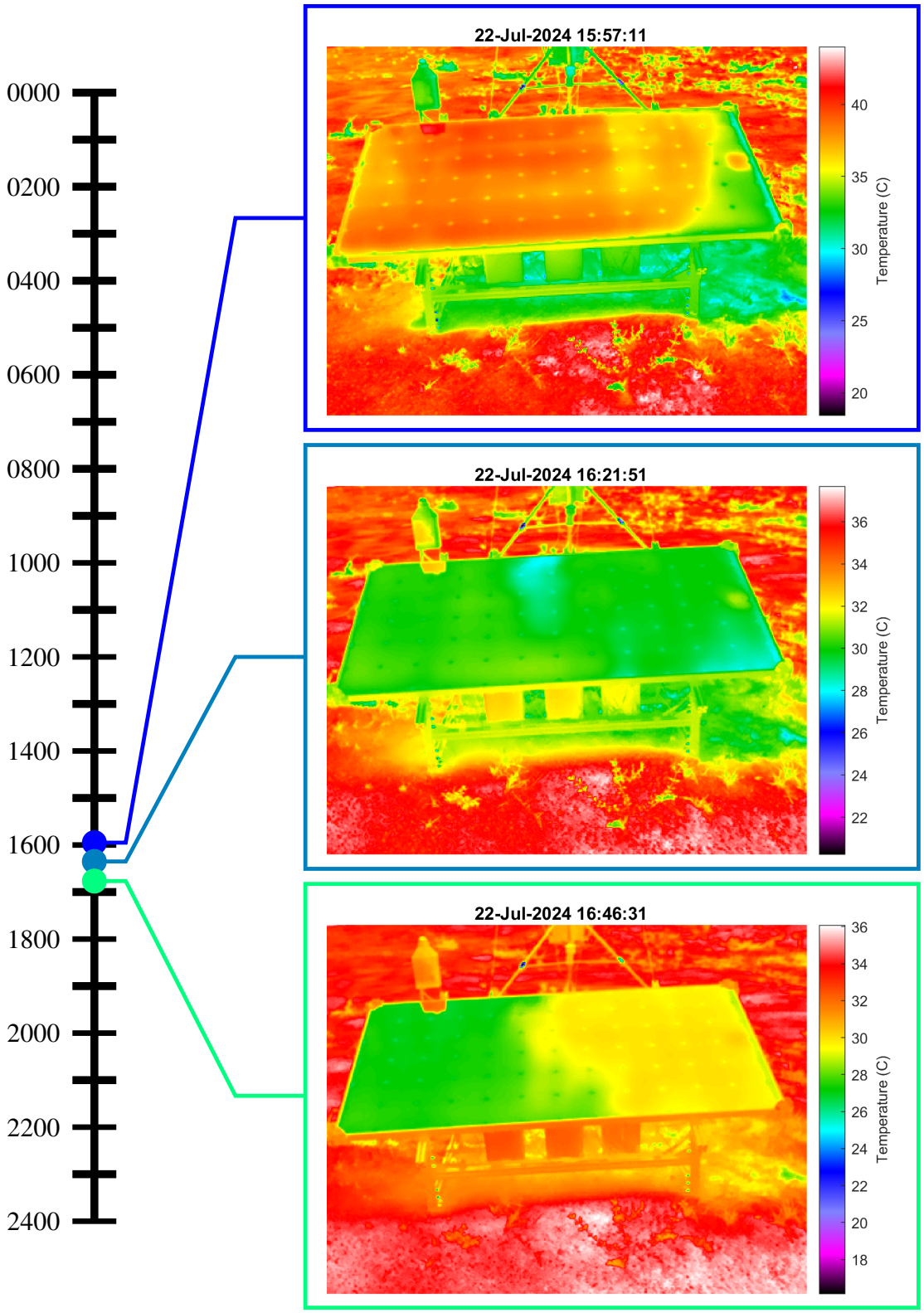



Figure 35: The observed PV panel cell temperatures obtained via the FLIR camera as deployed to AIHPA Testbed on 22 July 2024 from 0700 through 1800 MST.

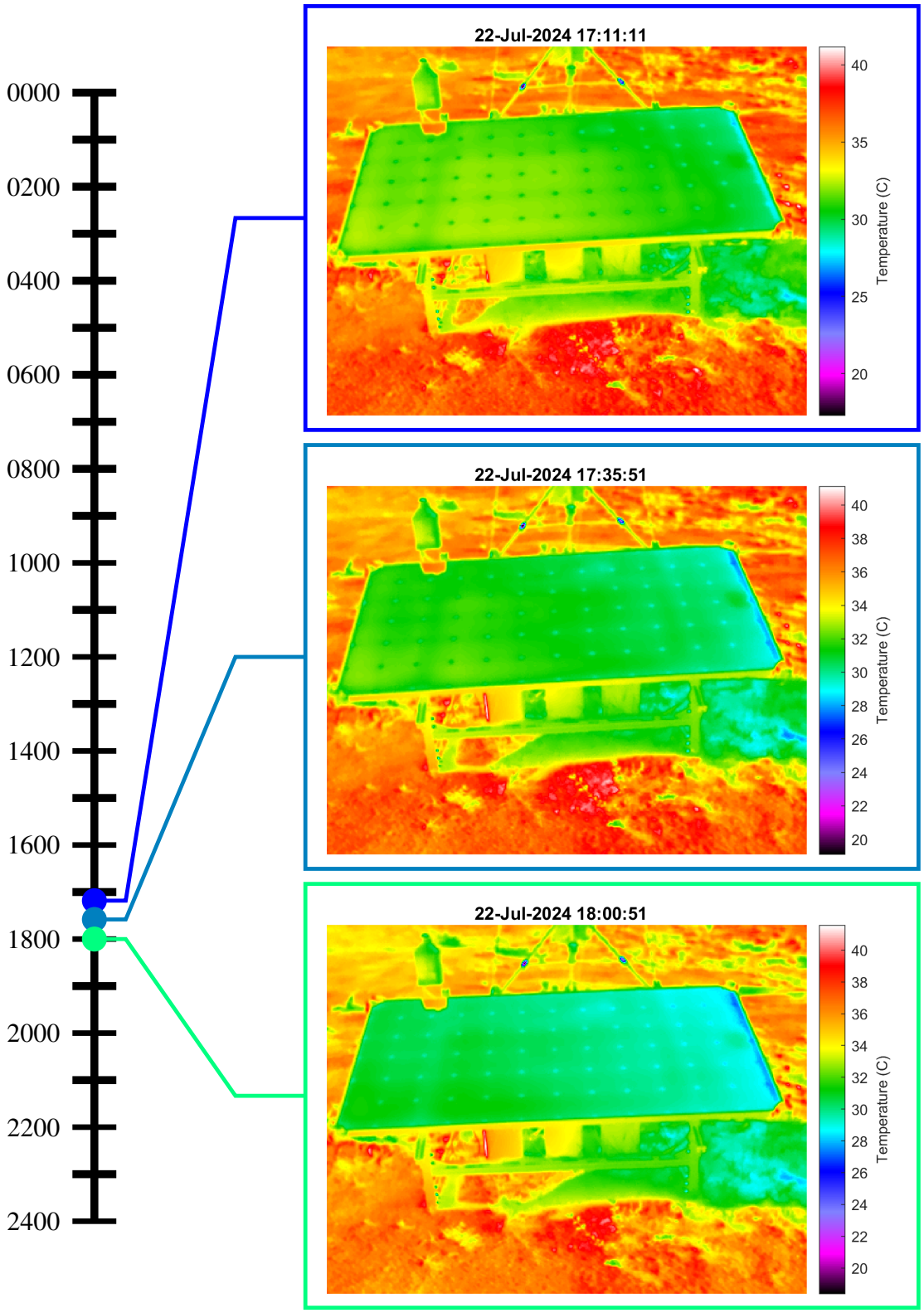
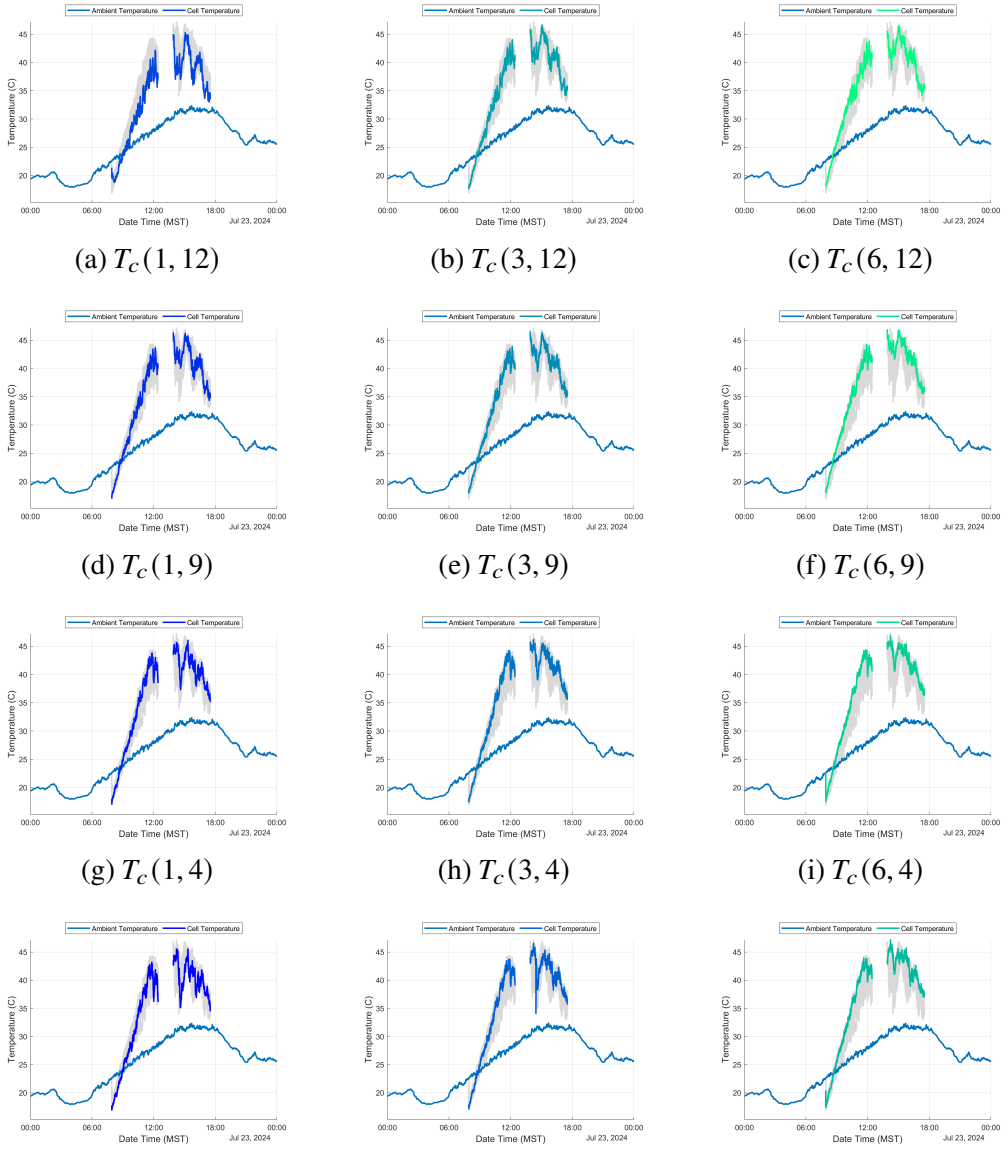



Figure 36: The observed PV panel cell temperatures obtained via the FLIR camera as deployed to AIHPA Testbed on 22 July 2024 from 0700 through 1800 MST.

## 5.3 FLIR Characterizations for 23 July 2024

The FLIR camera was deployed to the AIHPA Testbed for a relatively short period on 23 July 2024 from 0700 through 1800 MST. The approximate time-series response of the individual cell temperatures is provided in Figure 37, which was ultimately derived from multiple sequential FLIR images. A small subset of the observed FLIR images is provided in Figures 38–41.




(a) $T_c(1,12)$ (b) $T_c(3,12)$ (c) $T_c(6,12)$

(d) $T_c(1,9)$ (e) $T_c(3,9)$ (f) $T_c(6,9)$

(g) $T_c(1,4)$ (h) $T_c(3,4)$ (i) $T_c(6,4)$

(j) $T_c(1,1)$ (k) $T_c(3,1)$ (l) $T_c(6,1)$

Figure 37: The observed PV panel cell temperatures obtained via the FLIR camera as deployed to AIHPA Testbed on 23 July 2024 from 0700 through 1800 MST.

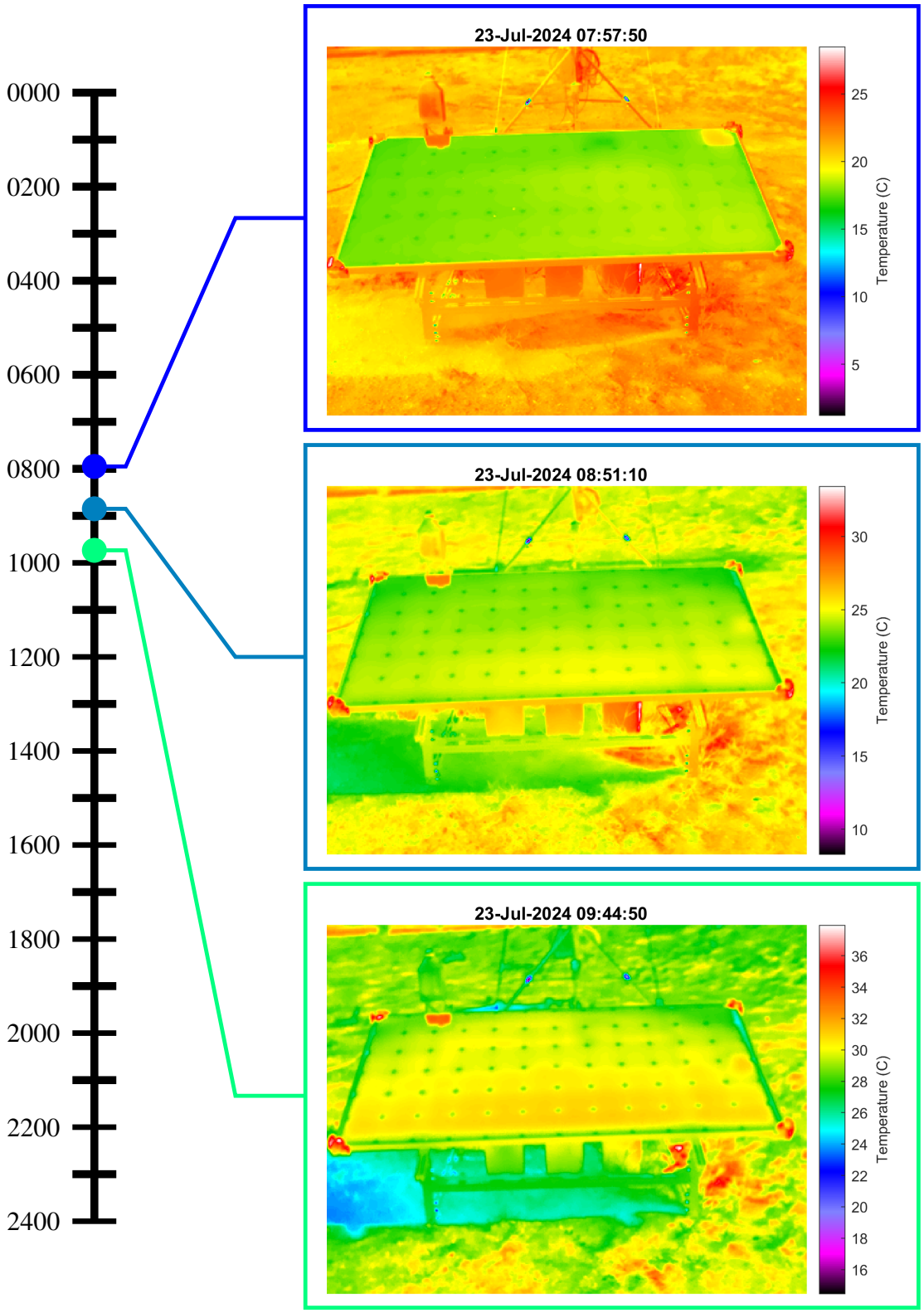



Figure 38: The observed PV panel cell temperatures obtained via the FLIR camera as deployed to AIHPA Testbed on 23 July 2024 from 0700 through 1800 MST.

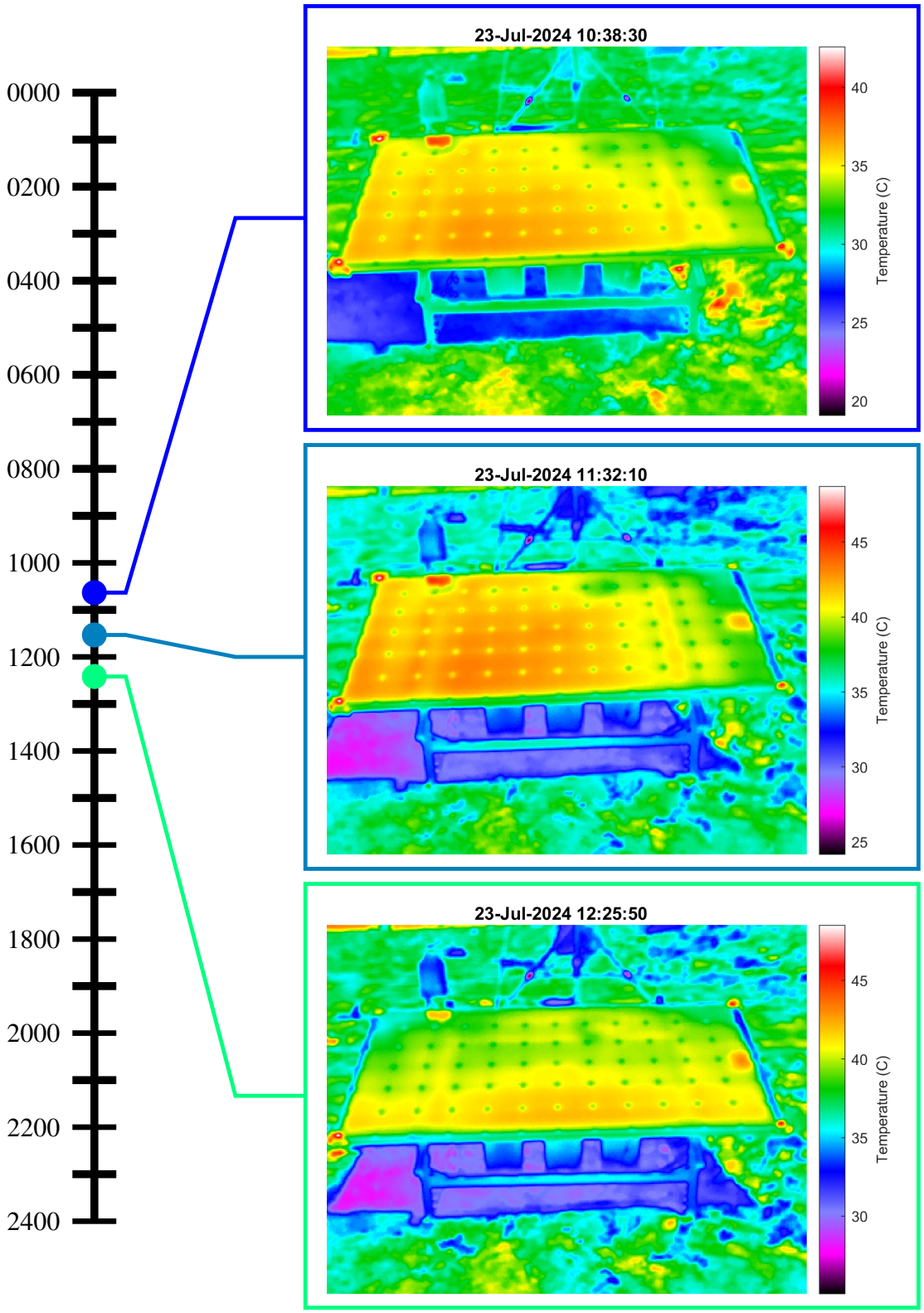



Figure 39: The observed PV panel cell temperatures obtained via the FLIR camera as deployed to AIHPA Testbed on 23 July 2024 from 0700 through 1800 MST.

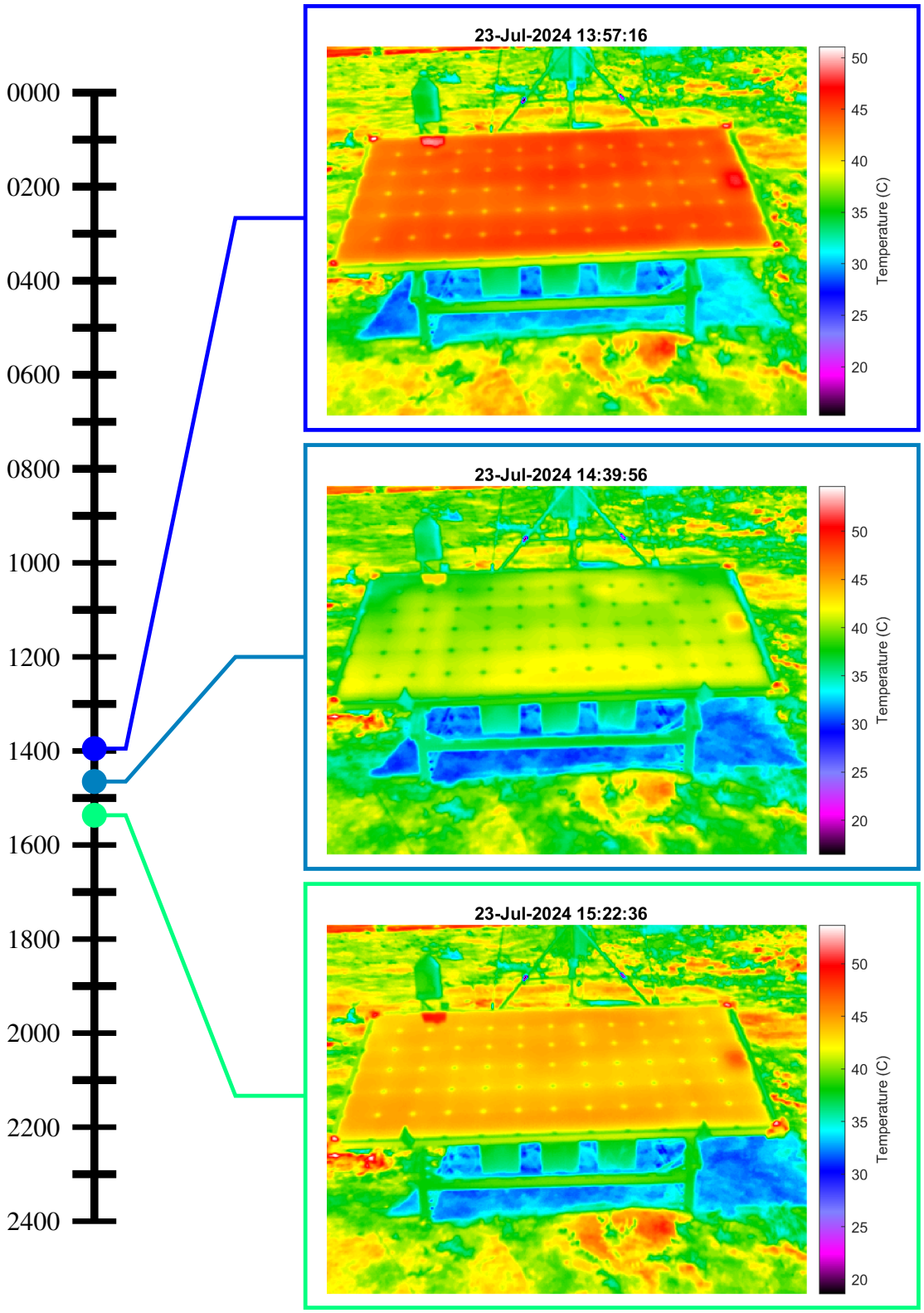



Figure 40: The observed PV panel cell temperatures obtained via the FLIR camera as deployed to AIHPA Testbed on 23 July 2024 from 0700 through 1800 MST.

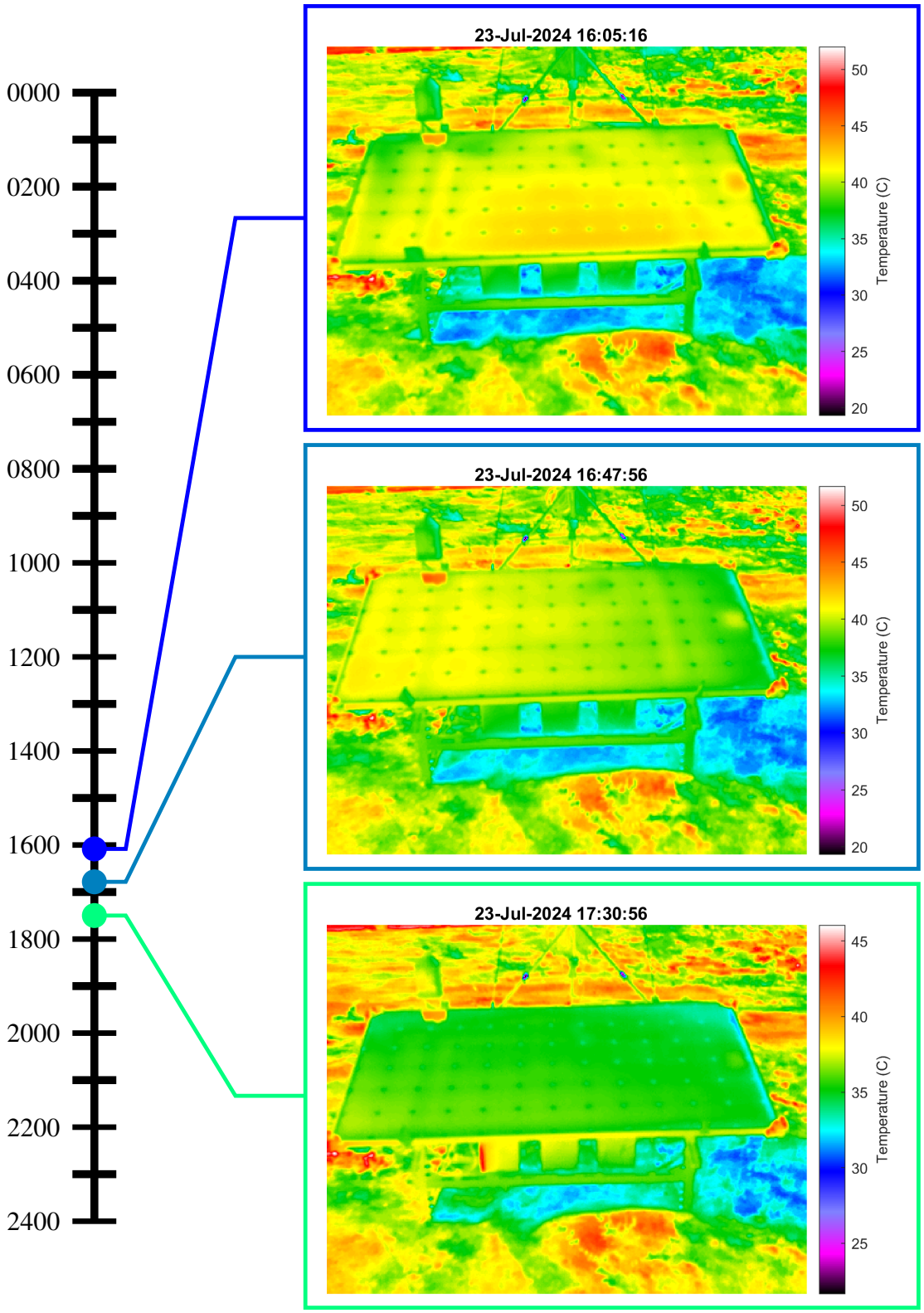
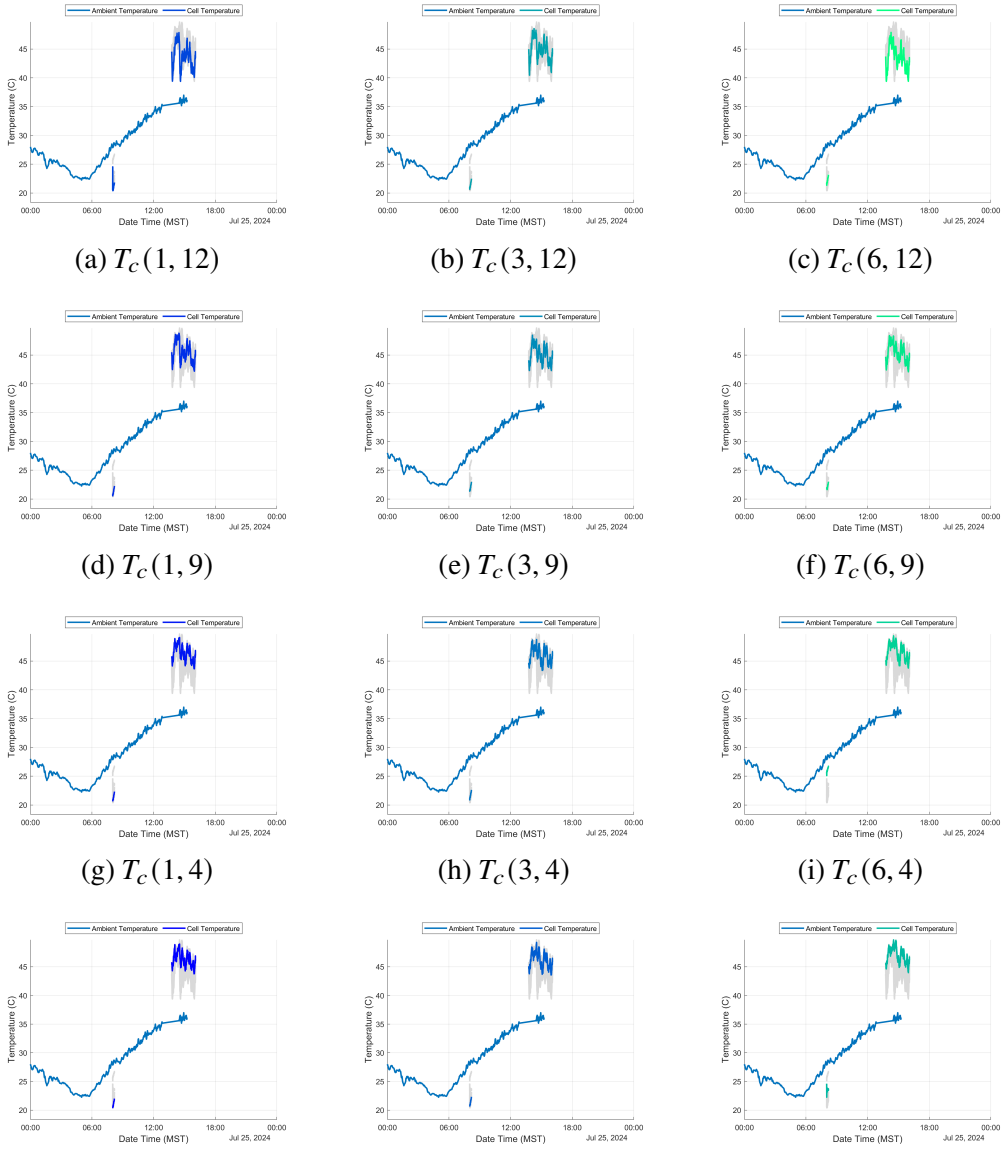



Figure 41: The observed PV panel cell temperatures obtained via the FLIR camera as deployed to AIHPA Testbed on 23 July 2024 from 0700 through 1800 MST.

## 5.4 FLIR Characterizations for 25 July 2024

The FLIR camera was deployed to the AIHPA Testbed for a relatively short period on 25 July 2024 from 0700 through 1800 MST. The approximate time-series response of the individual cell temperatures is provided in Figure 42, which was ultimately derived from multiple sequential FLIR images. A small subset of the observed FLIR images is provided in Figures 43–45.




(a) $T_c(1,12)$ (b) $T_c(3,12)$ (c) $T_c(6,12)$

(d) $T_c(1,9)$ (e) $T_c(3,9)$ (f) $T_c(6,9)$

(g) $T_c(1,4)$ (h) $T_c(3,4)$ (i) $T_c(6,4)$

(j) $T_c(1,1)$ (k) $T_c(3,1)$ (l) $T_c(6,1)$

Figure 42: The observed PV panel cell temperatures obtained via the FLIR camera as deployed to AIHPA Testbed on 25 July 2024 from 0700 through 1800 MST.

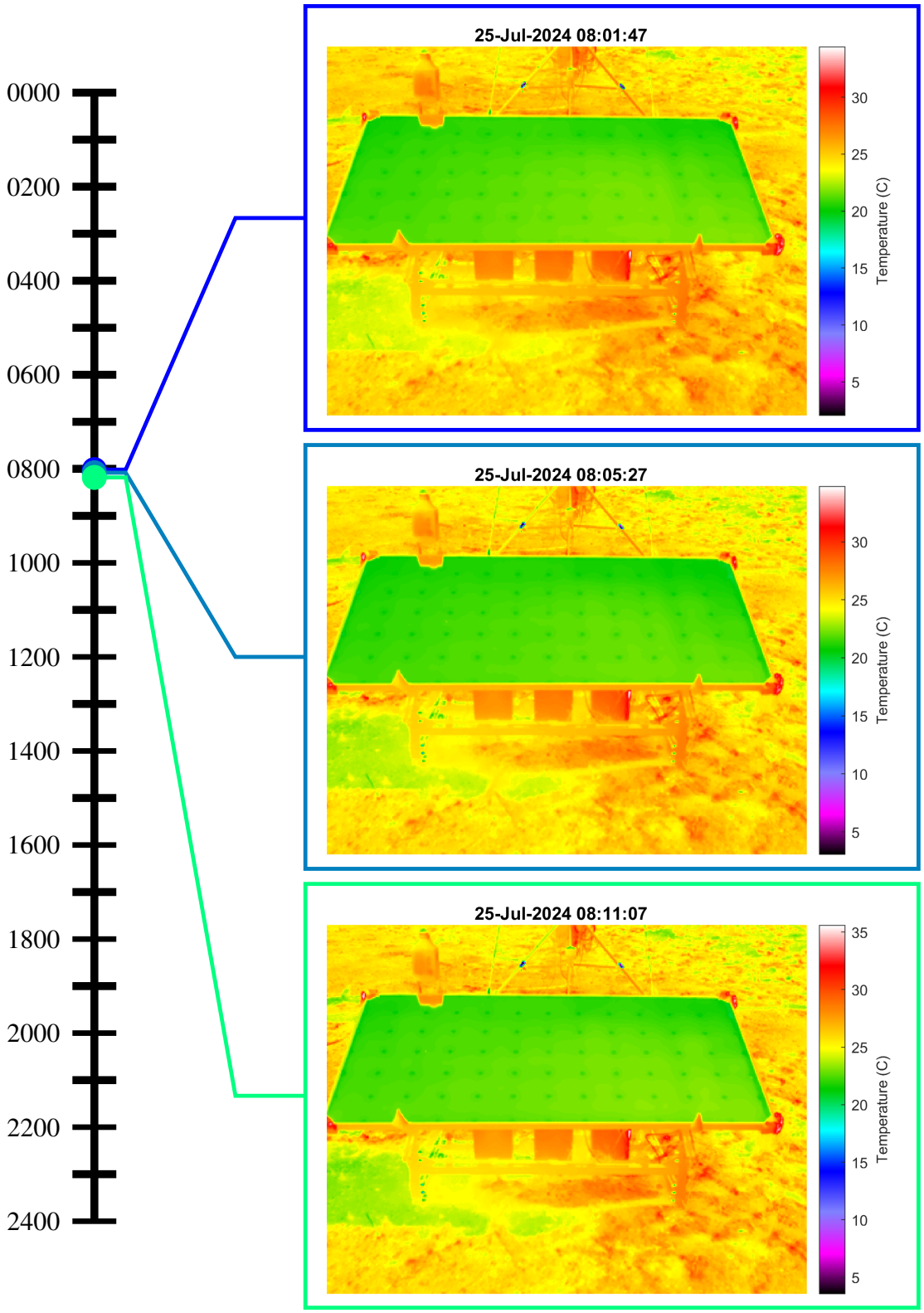



Figure 43: The observed PV panel cell temperatures obtained via the FLIR camera as deployed to AIHPA Testbed on 25 July 2024 from 0700 through 1800 MST.

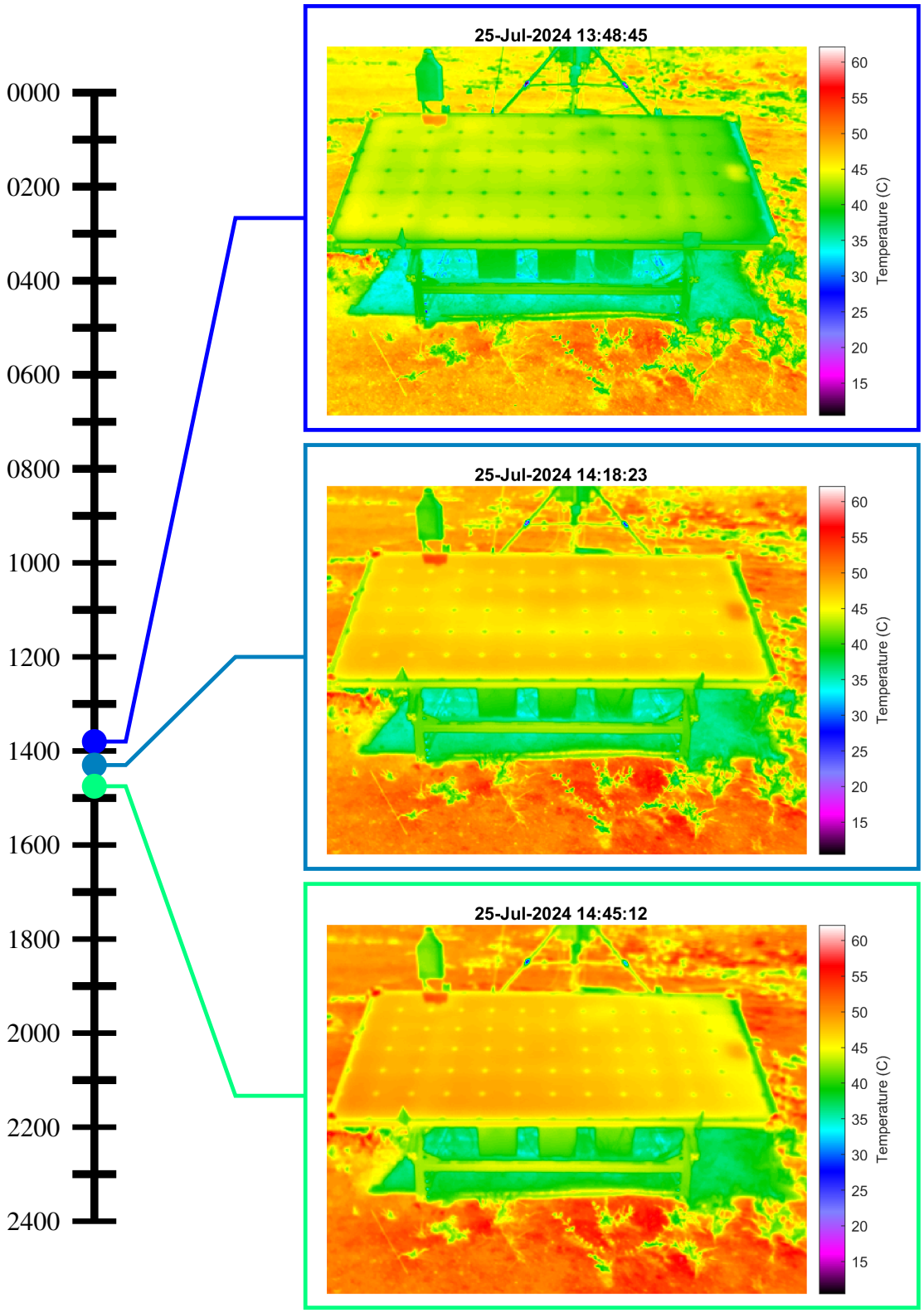



Figure 44: The observed PV panel cell temperatures obtained via the FLIR camera as deployed to AIHPA Testbed on 25 July 2024 from 0700 through 1800 MST.

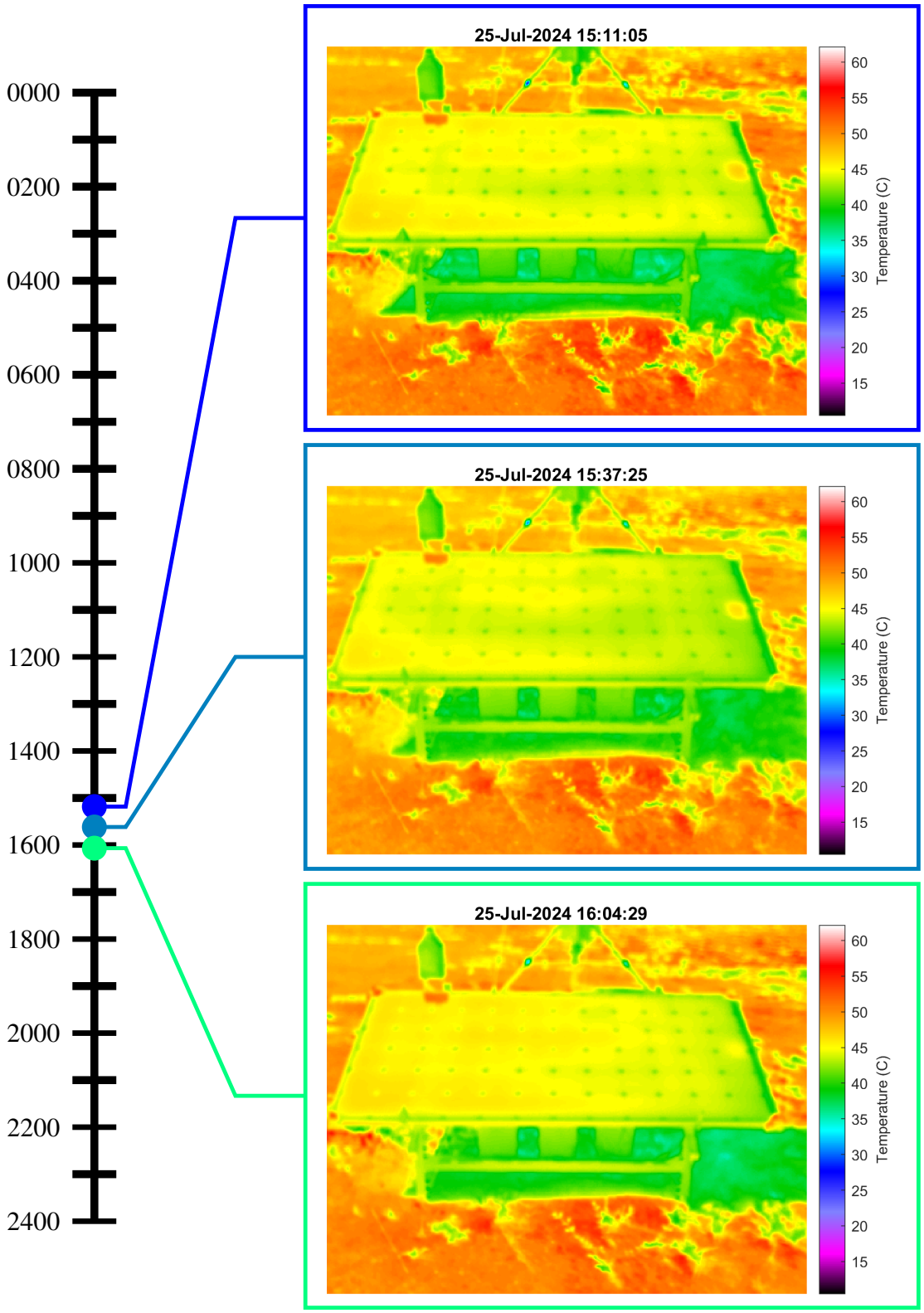



Figure 45: The observed PV panel cell temperatures obtained via the FLIR camera as deployed to AIHPA Testbed on 25 July 2024 from 0700 through 1800 MST.

## 5.5 Summary

Deployment of the FLIR thermal imager allowed extended monitoring of the PV array's temperature distribution. However, the array's measured temperatures may not accurately reflect the true temperature of the PV cells themselves. PV arrays are designed with high emissivity in the near-IR spectrum and use IR-permissive glass lamination to protect the cells from the environment. This lamination results in a highly emissive and reflective front surface. Consequently, it remains uncertain whether the FLIR measurements accurately represent cell temperature. This uncertainty is exacerbated by the failure of the back-panel temperature probe within the AIHPA Testbed, preventing direct temperature validation during the FLIR deployment.

Cell temperature profiles obtained from the FLIR thermal imager exhibit a strong correlation with panel temperature time series recorded on other days via the AIHPA MMT, as illustrated in Figures 46–48. This suggests the FLIR thermal imager accurately observes the thermal behavior of the PV cells; however, this conclusion is based solely on data collected during its deployment within proximity to the AIHPA Testbed. In contrast, FLIR images captured during deployment at USMA did not accurately reflect PV cell thermal behavior, likely due to reflections from adjacent building and roof structures visible in the lower-right corner of the images. These reflections significantly compromise the reliability of the measured temperatures. Fortunately, AIHPA Testbed FLIR images were free of such perturbations, attributable to the absence of nearby structures.

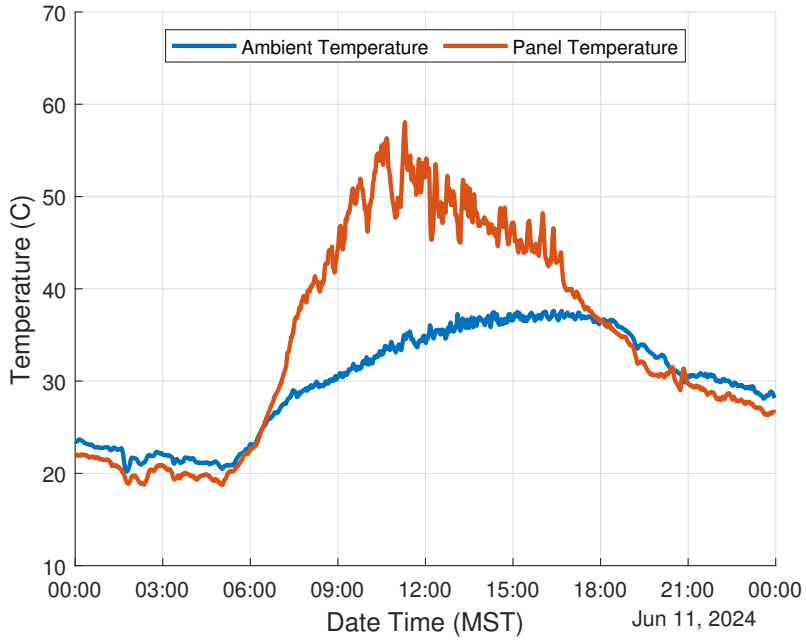



Figure 46: The observed ambient and panel temperature time series as measured via the MMT for 11 June 2024.

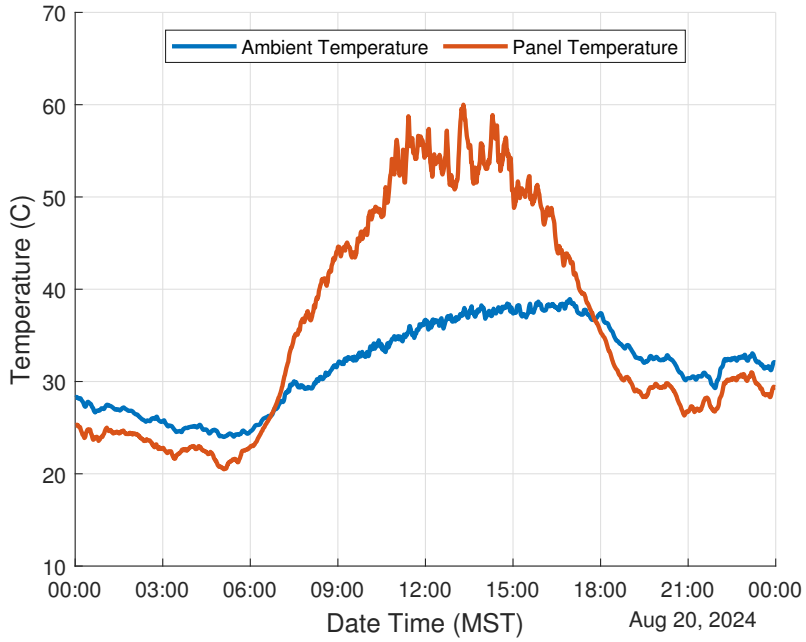



Figure 47: The observed ambient and panel temperature time series as measured via the MMT for 20 August 2024.

Currently, a variant of the AIHPA Testbed is being established at USMA. Upon completion, the testbed will incorporate at least four temperature probes mounted

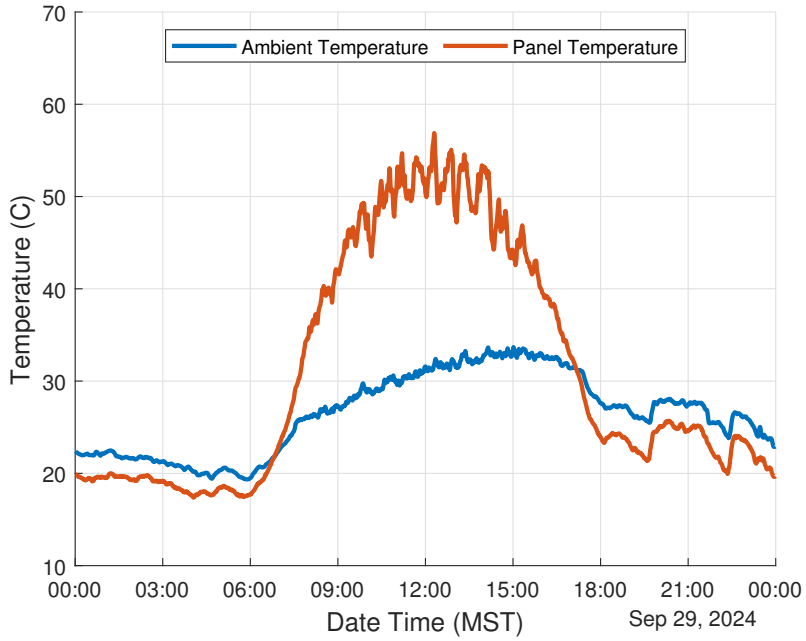


Figure 48: The observed ambient and panel temperature time series as measured via the MMT for 29 September 2024.

to the corners of the PV module. Following this, the FLIR thermal imager will be redeployed to the testbed to investigate the thermal response of the PV panel and determine precisely what the imager is measuring and its relationship to cell temperature. While the thermal imager may not directly measure cell temperature due to the high emissivity and reflectivity of a PV module, the observed thermal signature closely resembles expected cell temperature behavior. This correlation could provide valuable insight into the PV module's thermal characteristics, ultimately enabling more comprehensive and accurate power and energy predictions.

## 6. Conclusions

Inefficient energy use in constrained and contested environments degrades capabilities across all operational domains and echelons, a challenge compounded by the finite nature of energy resources and by adversarial actions that disrupt operations and logistics. Hybridized energy networks—integrating traditional and nontraditional E&P solutions—enable tactical energy generation, but their effective utilization requires sophisticated control and regulation systems capable of harmonizing distributed assets. Modern approaches leverage historical data, state estimation, and emerging

technologies such as AI/ML. Because nontraditional resources (such as PV arrays, wind turbines, and wave energy converters) depend heavily on dynamic operational conditions. The ability to forecast those conditions is what enables optimal energy generation, thus allowing the Warfighter to generate power at the tactical edge and reducing reliance on sole-source fuels such as jet propellant-8, whose distribution may be restricted by adversarial action against logistical supply operations.

This report investigated the characterization of a PV array, motivated by the finding that a manufacturer-configured power model–while accurate at high irradiance–failed to predict panel power across all conditions. This shortfall pointed to the cell temperature as the unmodeled variable (see Section 2). The technical literature similarly identified cell temperature and solar irradiance as the dominant factors governing the energy and power efficiency of PV arrays. While solar irradiance is the primary limit on PV production—and cloud propagation and tracking are receiving increased attention due to emerging capabilities such as high-energy lasers (HELs), high-powered microwaves, wireless power transfer, and power beaming—research into predicting atmospheric thermal behavior and PV cell temperature remains comparatively limited. Accordingly, this report pursued three contributions, summarized below.

First, the E&P generation of a PV reference cell was characterized. Using an arc-lamp class AAA solar simulator and a PV reference cell, the cell's voltage and current behavior was measured across a range of temperatures, yielding an E&P characterization capable of approximating the reference cell's performance. The characterization accurately predicted performance at high irradiance levels but underpredicted performance at lower levels, most likely because the cell was not characterized at standard test conditions (STC). Despite this limitation, the resulting model adequately approximated E&P capability.

Second, a lumped-parameter thermal model was developed. Using the same solar simulator, the PV reference cell was irradiated for approximately 45 min and then allowed to cool to ambient temperature; the resulting data were used to estimate the model's thermal constants. The model accurately predicted thermal behavior for four of five operational conditions. However, all thermal characterizations failed to capture

the dynamic thermal response during rapid irradiance transitions—specifically, the lag between full irradiance and complete obstruction—indicating an incomplete dynamic component within the model. Further research is needed to extend the characterization and develop a scalable model applicable to a wider range of PV modules and cells.

Third, a FLIR thermal imager was used to characterize a PV module at the array level. Two modules were observed under significantly different atmospheric conditions: one at USMA and another at a desert location. The initial USMA deployment was intended primarily to assess the imager's general performance, but the module's proximity to buildings that reflected thermal radiation limited the accuracy of the resulting characterizations. In contrast, the desert deployment proved insightful. There, the imager was collocated with the AIHPA Testbed and its back-panel temperature probe; although the probe malfunctioned during the FLIR test—preventing a direct comparison of observed and measured temperatures—the testbed's extended operational history enabled comparisons against representative data. This comparison indicated that the FLIR imager detected thermal behavior consistent with typical back-panel temperature probe readings. These results suggested that the FLIR is a promising means of observing array-level thermal behavior under field conditions.

Taken together, these characterizations advance the ability to predict PV cell temperature and, in turn, forecast both energy supply and the thermal demand that drives systems such as environmental control units. More accurate thermal prediction directly supports the optimal regulation of hybrid energy networks, ultimately reducing the Warfighter's reliance on contested fuel logistics at the tactical edge.

# 7. Future Work

Several avenues for future work remain. Near-term efforts will focus on resolving the limitations identified above: characterizing the PV reference cell at STC to improve low-irradiance prediction, and augmenting the lumped-parameter thermal model with the dynamic component needed to capture rapid irradiance transitions.

A significant opportunity is presented by the recent fielding of a variant of the AIHPA Testbed at an alternative location at USMA. This variant has been deployed to multiple ranges for continuous operation and supported academic HEL missions. A fully instrumented variant is expected to be operational by the end of FY26. This variant will include the corner-mounted back-panel temperature probes absent from prior deployments, thus enabling the direct FLIR-to-probe validation that the present effort could not complete.

Beyond thermal validation, the USMA testbed is positioned to serve as a broader research and education platform. Anticipated efforts include additional HEL missions; uncrewed aerial system studies; and battery sciences research, development, and experimentation. The testbed will support both internal research and collaborative teaching across multiple USMA departments, bridging the gap between tactical power experimentation and cadet education. Specifically, the platform supports high-energy and pulsed-power academic missions while offering cadets hands-on opportunities to integrate and deploy alternative energy storage and novel materials. These collaborative cadet projects will directly inform the development and design of future mobilized testbeds.

## 8. References


1. Vaucher GT, D'Arcy MS, Berman MS. In-situ atmospheric intelligence for hybrid power grids: volume 1 (feasibility study). DEVCOM Army Research Laboratory (US). 2019 Dec. Report No: ARL-TR-8864.
2. Vaucher GT et al. In-situ atmospheric intelligence for hybrid power grids: volume 2 (automated data flow tests). DEVCOM Army Research Laboratory (US). 2020 Sep. Report No.: ARL-TR-9060.
3. Vaucher GT, Lee MD, Goodman H. In-situ atmospheric intelligence for hybrid power grids: volume 3 (analysis of whole sky image compression). DEVCOM Army Research Laboratory (US). 2021 Dec. Report No: ARL-TR-9360.
4. Vaucher GT, Bergen S. In-situ atmospheric intelligence for hybrid power grids: volume 4 (climate impacts on tactical power generation-part 1), sensor comparison and site characterization. DEVCOM Army Research Laboratory (US). 2022 Feb. Report No.:ARL-TR-9411.
5. Vaucher GT, Jane RS, Whitaker J. In-situ atmospheric intelligence for hybrid power grids: volume 5 (ambient vs. panel temperature in photovoltaic power modeling). DEVCOM Army Research Laboratory (US). 2022 May. Report No.: ARL-TR-9454.
6. Lee MD, D'Arcy MS, Vaucher GT. In-situ atmospheric intelligence for hybrid power grids: volume 6 (convolutional neural networks for whole sky imager data analysis). DEVCOM Army Research Laboratory (US). 2022 June. Report No.: ARL-TR-9475.
7. Jane RS et al. In-situ atmospheric intelligence for hybrid power grids: volume 7 (squad energy and power scenario). DEVCOM Army Research Laboratory (US). 2022 June. Report No.: ARL-TR-9479.
8. Jane RS et al. In-situ atmospheric intelligence for hybrid power grids: volume 8 (micro-grid energy and power scenario). DEVCOM Army Research Laboratory (US). 2022 Sep. Report No.: ARL-TR-9559.
9. Vaucher GT, Lee MS, Goodman H. Atmospheric intelligence for hybrid power advancements: volume 1 (wind impacts on photovoltaic power/panel

temperature). DEVCOM Army Research Laboratory (US). 2023 Jan. Report No.: ARL-TR-9629.

10. Vaucher GT, Hailey Goodman BW, Lee MS. Atmospheric intelligence for hybrid power advancements: volume 2 (whole sky image percent cloud and sun analyses). DEVCOM Army Research Laboratory (US). 2023 May. Report No.: ARL-TR-9682.
11. Vaucher GT, LaRosa J, Lee MS, Jane RS. Atmospheric intelligence for hybrid power advancements: volume 3 (whole sky image percent cloud and blue sky analyses). DEVCOM Army Research Laboratory (US). 2024 June. Report No.: ARL-TR-9925.
12. Vaucher GT et al. Atmospheric intelligence for hybrid power advancements: volume 4 (hydrogen fuel cell background). DEVCOM Army Research Laboratory (US). 2024 Dec. ARL-TR-10040.
13. MathWorks. PV array model. Accessed 2024 May 13. MathWorks. 2024. https://www.mathworks.com/help/sps/powersys/ref/pvarray.html
14. Dave MK. Modeling of pv arrays based on datasheet. In: 2016 ieee 1st international conference on power electronics, intelligent control and energy systems (icpeices); 2016. p. 1–4. https://doi.org/10.1109/ICPEICES.2016.7853617
15. Villalva MG, Gazoli JR, Filho ER. Comprehensive approach to modeling and simulation of photovoltaic arrays. IEEE Transactions on Power Electronics. 2009;24(5):1198–1208. https://doi.org/10.1109/TPEL.2009.2013862
16. Premkumar M, Chandrasekaran K, Sowmya R. Mathematical modelling of solar photovoltaic cell/panel/array based on the physical parameters from the manufacturer's datasheet. International Journal of Renewable Energy Development. 2020;9(1):7.
17. Tian H, Mancilla-David F, Ellis K, Muljadi E, Jenkins P. A cell-to-module-to-array detailed model for photovoltaic panels. Solar Energy. 2012;86(9):2695–2706.
18. Sayed K, Abdel-Salam M, Ahmed M, Ahmed AA. Modeling and simulation of pv arrays. In: Asme international mechanical engineering congress and exposition; 2010. p. 1113–1120.

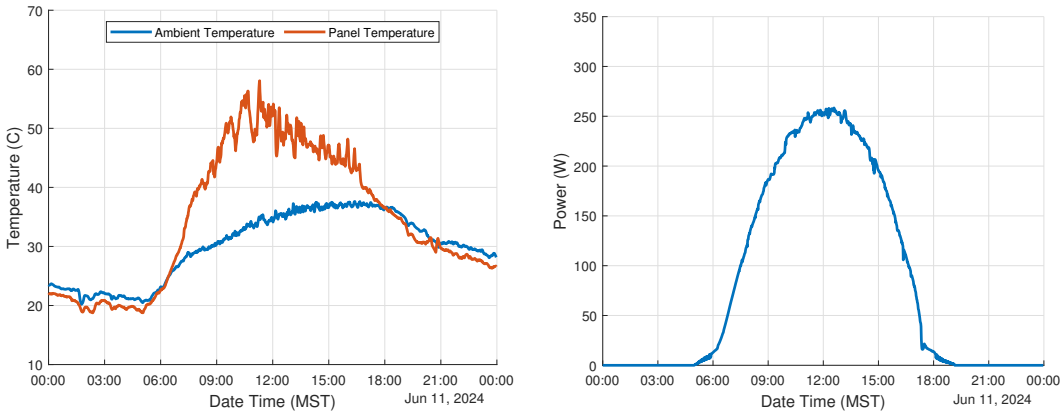
19. Alsayid B. Modeling and simulation of photovoltaic cell/module/array with two-diode model. International Journal of Computer Technology and Electronics Engineering (IJCTEE). 2012;1(3):6–11.
20. Ortiz-Rivera EI, Peng FZ. Analytical model for a photovoltaic module using the electrical characteristics provided by the manufacturer data sheet. In: 2005 ieee 36th power electronics specialists conference; 2005. p. 2087–2091.

# Appendix A: AIHPA Testbed

The Atmospheric Intelligence for Hybrid Power Advancements (AIHPA) Testbed is equipped with a 315-W Sunmodule Pro-Series XL monocrystalline photovoltiac (PV) module, along with sensors to measure voltage, current, temperature (panel and ambient), atmospheric pressure, humidity, irradiance, wind speed, and direction. Example time-series data collected by the AIHPA Testbed are provided in Figures A-1 through A-6.

The first three cases (Figures A-1 through A-3; 11 June 2024, 20 August 2024, and 29 September 2024) represent clear sky conditions. Under the cloud-free conditions, the solar radiation time series resembles a smooth Gaussian-shaped curve, implying uninterrupted heating across a PV panel. To further characterize the atmosphere, concurrent and coincident measurements of pressure, temperature, wind speed and wind direction are provided.

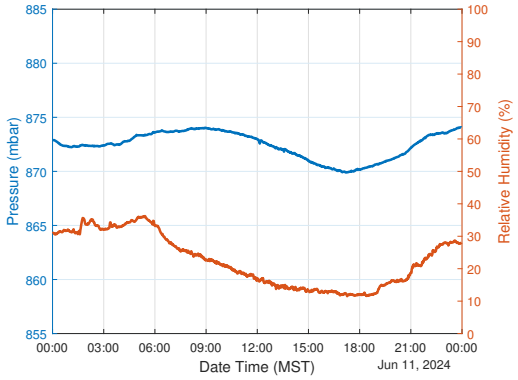
The final three cases (Figures A-4 through A-6: 10 June 2024, 2 July 2024, and 4 August 2024) represent partly cloudy sky conditions. Under partly cloudy sky conditions, cloud shadows impede the irradiance time series, causing momentary and sustained interferences. While the irradiance still maintains a Gaussian trend, the inclusion of cloud shadows leads to less uniform heating across a PV panel. Complementing the partly cloudy sky conditions are simultaneous measurements of pressure, relative humidity, temperature, wind speed, and wind direction.



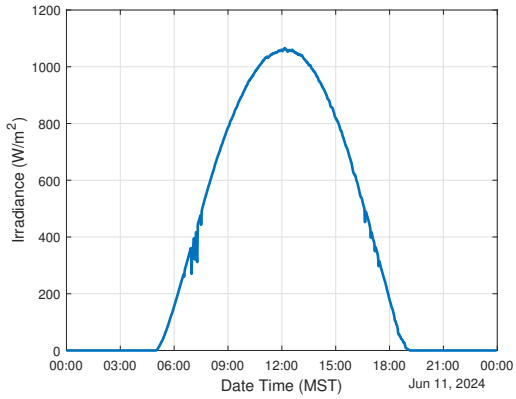

(a) Temperatures



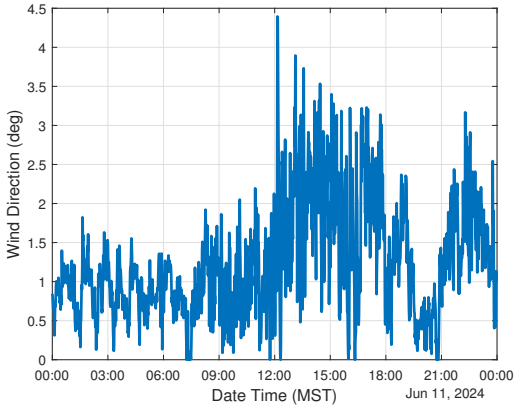

(b) Panel power



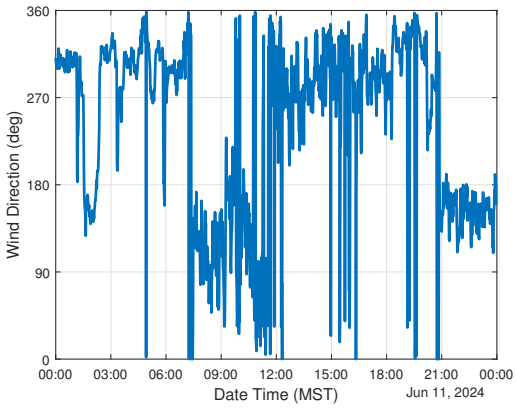

(c) Pressure




(d) Irradiance

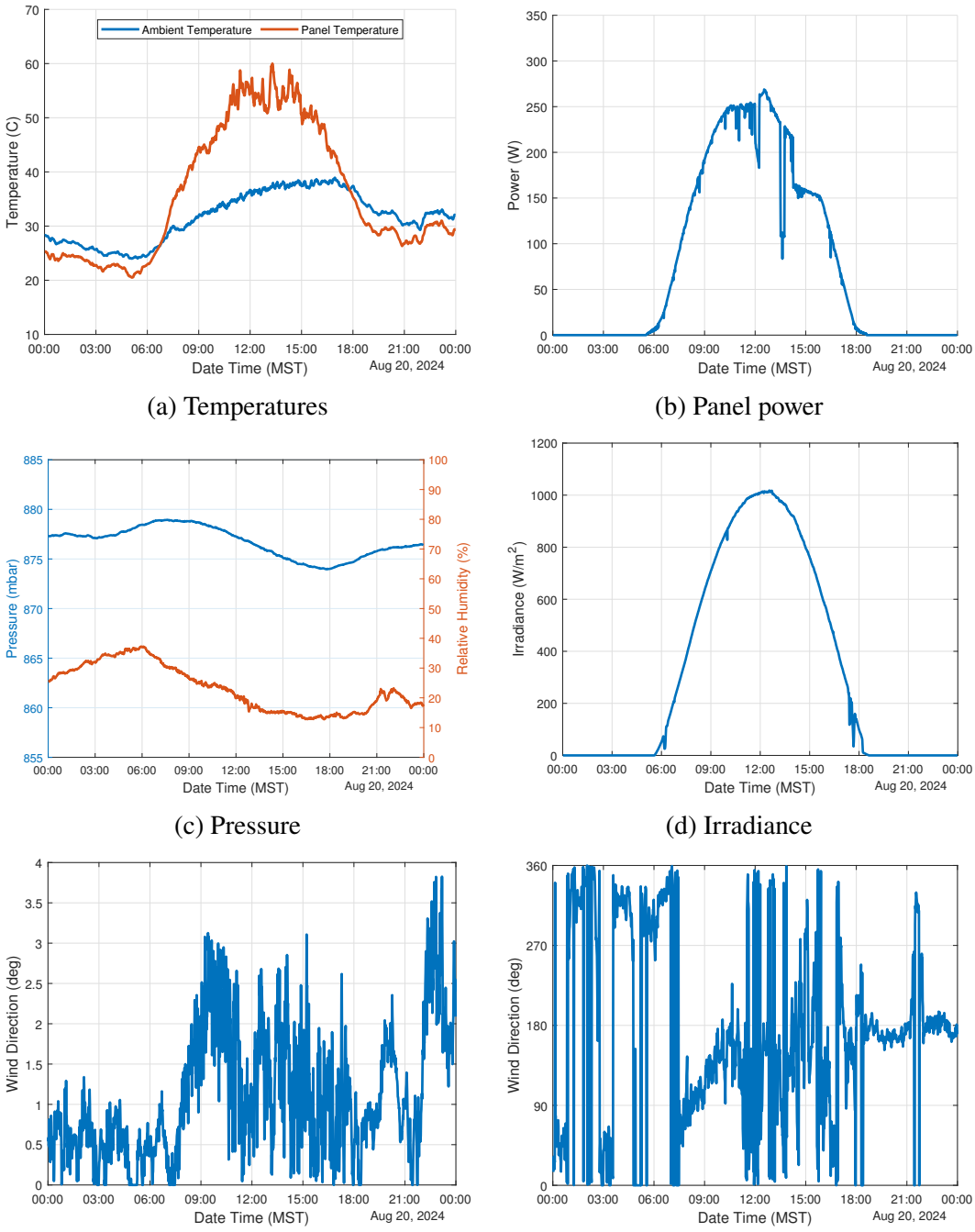



(e) Wind speed




(f) Wind direction

Figure A-1: AIHPA Testbed measurement for 11 June 2024. Representative data illustrating ambient temperature, panel temperature, panel power output, atmospheric pressure, solar irradiance, wind direction, and wind speed.




(a) Temperatures

(b) Panel power

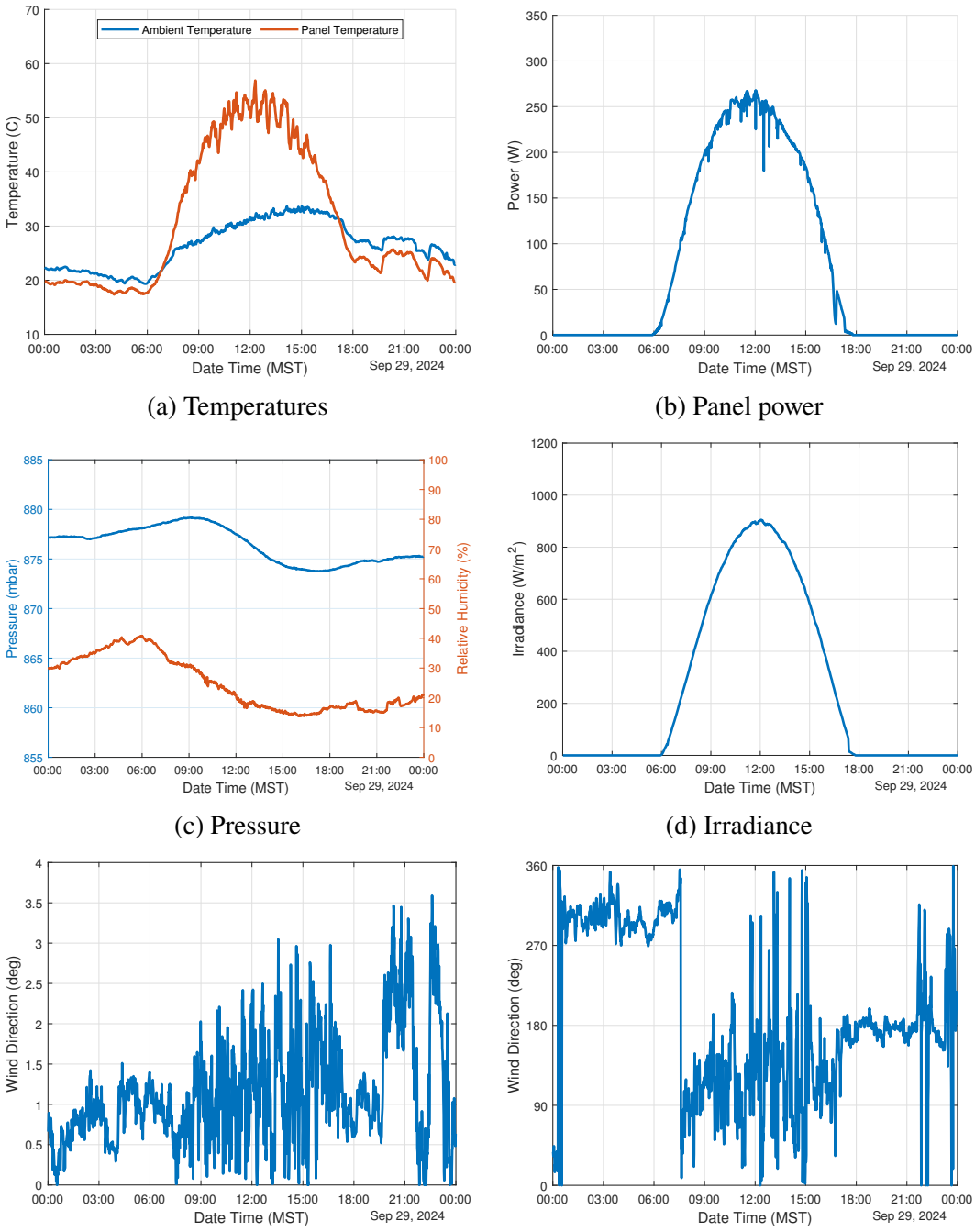
(c) Pressure

(d) Irradiance

(e) Wind speed

(f) Wind direction

Figure A-2: AIHPA Testbed measurements for 20 August 2024. Representative data illustrating ambient temperature, panel temperature, panel power output, atmospheric pressure, solar irradiance, wind direction, and wind speed.




(a) Temperatures

(b) Panel power

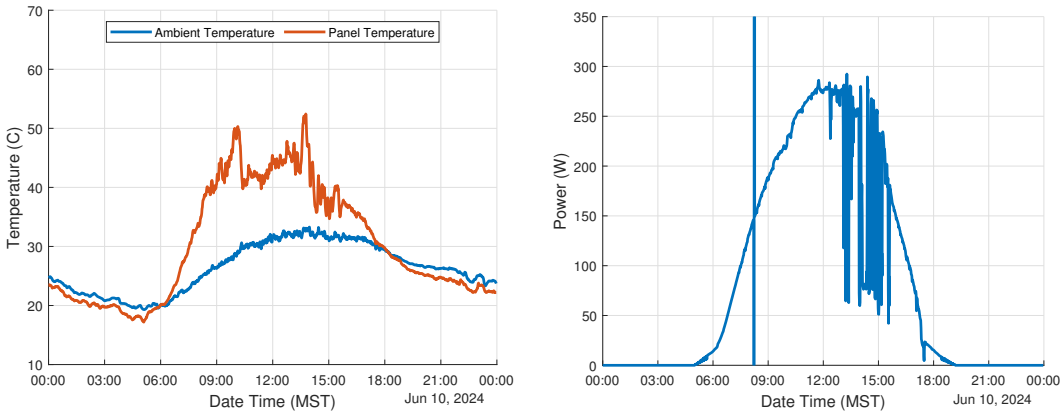
(c) Pressure

(d) Irradiance

(e) Wind speed

(f) Wind direction

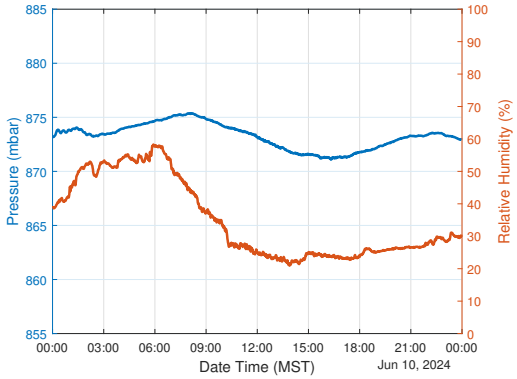
Figure A-3: AIHPA Testbed measurements for 29 September 2024. Representative data illustrating ambient temperature, panel temperature, panel power output, atmospheric pressure, solar irradiance, wind direction, and wind speed.



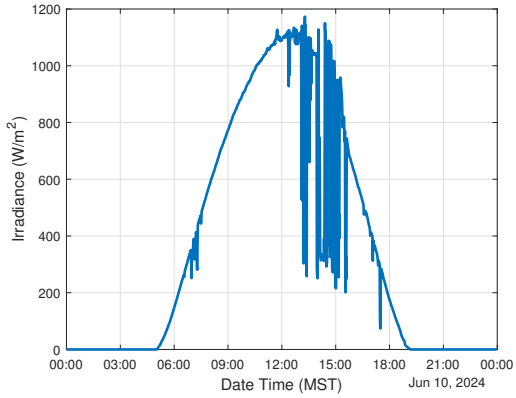

(a) Temperatures



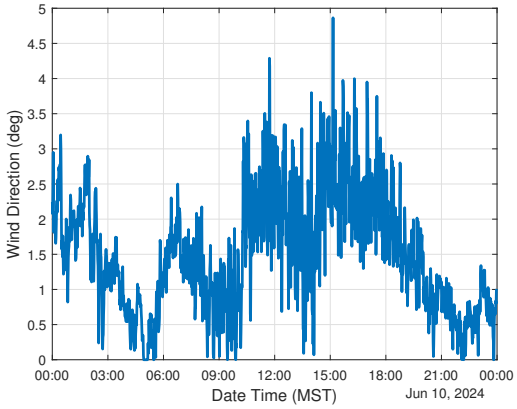

(b) Panel power



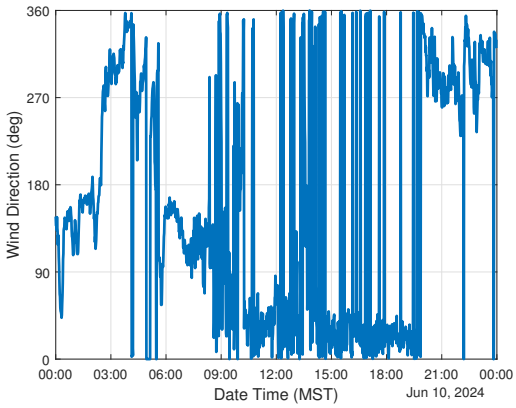

(c) Pressure




(d) Irradiance

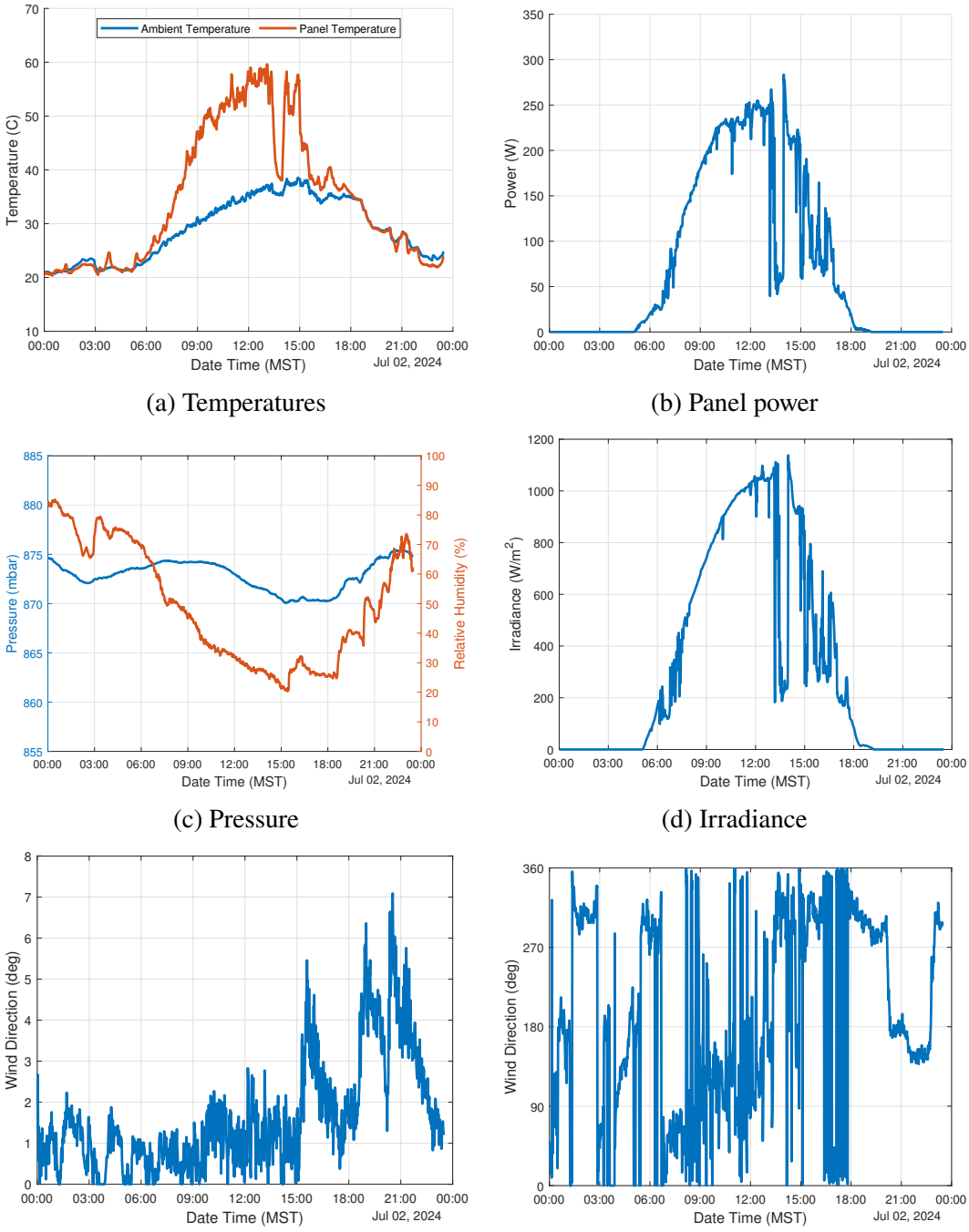



(e) Wind speed




(f) Wind direction

Figure A-4: AIHPA Testbed measurement for 10 June 2024. Representative data illustrating ambient temperature, panel temperature, panel power output, atmospheric pressure, solar irradiance, wind direction, and wind speed.




(a) Temperatures

(b) Panel power

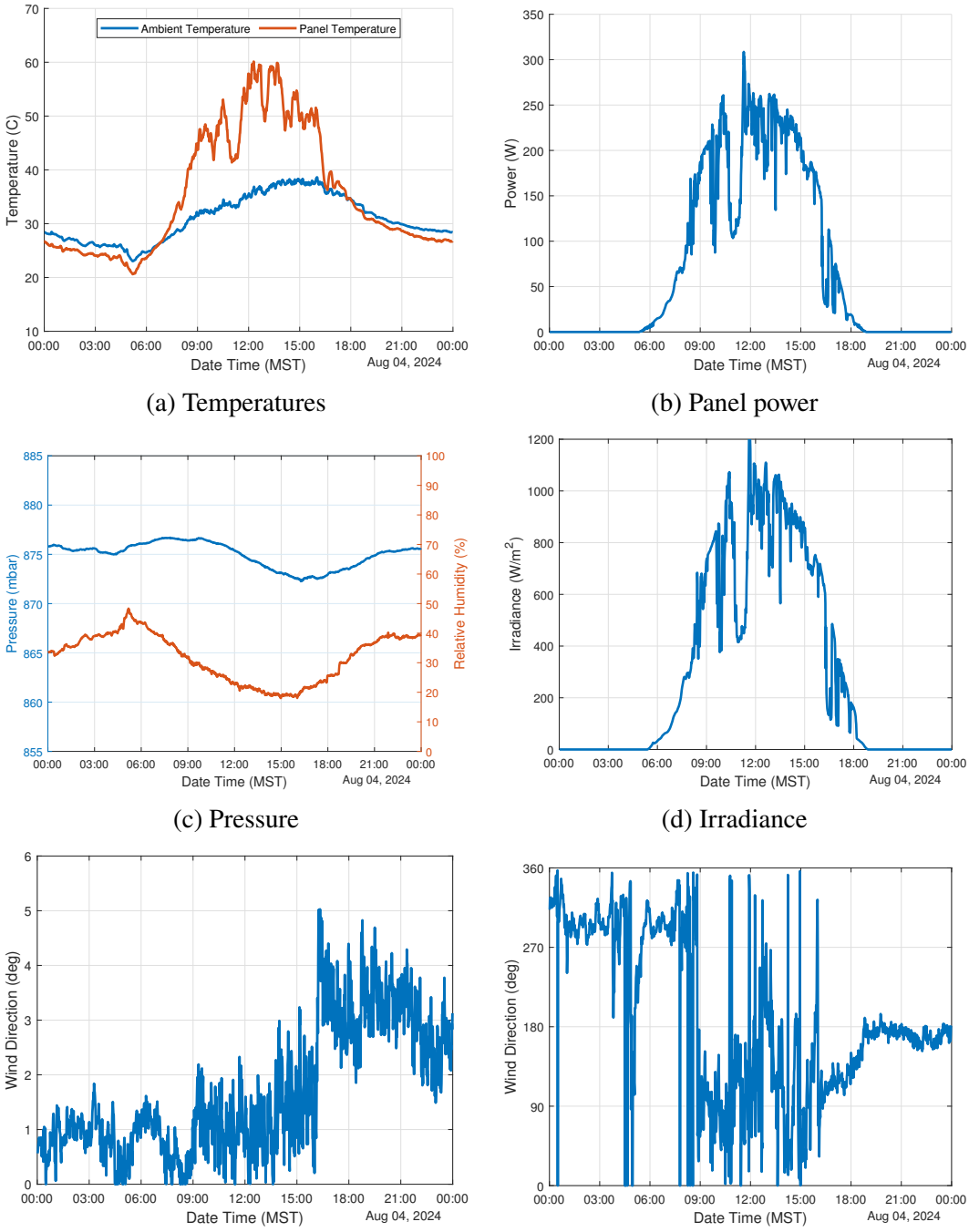
(c) Pressure

(d) Irradiance

(e) Wind speed

(f) Wind direction

Figure A-5: AIHPA Testbed measurements for 2 July 2024. Representative data illustrating ambient temperature, panel temperature, panel power output, atmospheric pressure, solar irradiance, wind direction, and wind speed.




(a) Temperatures

(b) Panel power

(c) Pressure

(d) Irradiance

(e) Wind speed

(f) Wind direction

Figure A-6: AIHPA Testbed measurement for 4 August 2024. Representative data illustrating ambient temperature, panel temperature, panel power output, atmospheric pressure, solar irradiance, wind direction, and wind speed.

## Appendix B: 315-W Sunmodule Pro-Series XL Monocrystalline

The Atmospheric Intelligence for Hybrid Power Advancements (AIHPA) Testbed possesses a 315-W Sunmodule Pro-Series XL monocrystalline photovoltiac (PV) module manufactured by Solar World. Table B-1 shows the data sheet that describes the panel at standard test conditions (STC), which holds an irradiance of 1000 W/m$^2$, ambient temperature of 25 $^o$C, and atmospheric pressure of 1.5 AM. Alternatively, the data sheet parameters that describe the panel at an irradiance of 800 W/m$^2$, ambient temperature of 46 $^o$C, and atmospheric pressure of 1.5 AM have been provided in Table B-2.

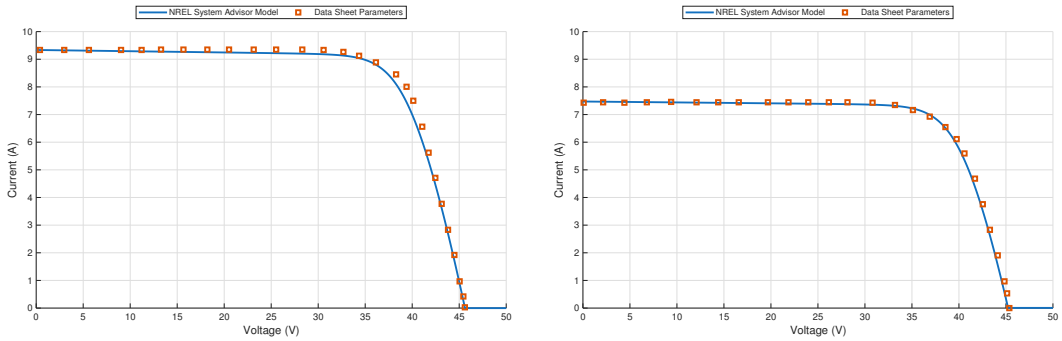
Table B-1: Data sheet parameters for a 315-W Sunmodule Pro-Series XL monocrystalline PV module at STC.

| Description | Variable | Value | Units |
|---|---|---|---|
| Maximum power | $P_{max}$ | 315 | W |
| Open circuit voltage | $V_{oc}$ | 45.6 | V |
| Short circuit current | $I_{sc}$ | 9.35 | A |
| Voltage at maximum power point | $V_{mp}$ | 36.5 | V |
| Current at maximum power point | $I_{mp}$ | 8.71 | A |
| Temperature coefficient at $V_{oc}$ | $\alpha_{V_{oc}}$ | −0.304 | %/$^o$C |
| Temperature coefficient at $I_{sc}$ | $\alpha_{I_{sc}}$ | 0.042 | %/$^o$C |
| Nominal operating cell temperature | NOTC | 46 | $^o$C |
| No. cells per module | $N_{cell}$ | 72 | # |
| No. series string | $N_{ser}$ | 1 | # |
| No. of parallel string | $N_{par}$ | 1 | # |

Table B-2: Data sheet parameters for a 315-W Sunmodule Pro-Series XL monocrystalline PV module at 800 W/m$^2$ operating at the NOTC.

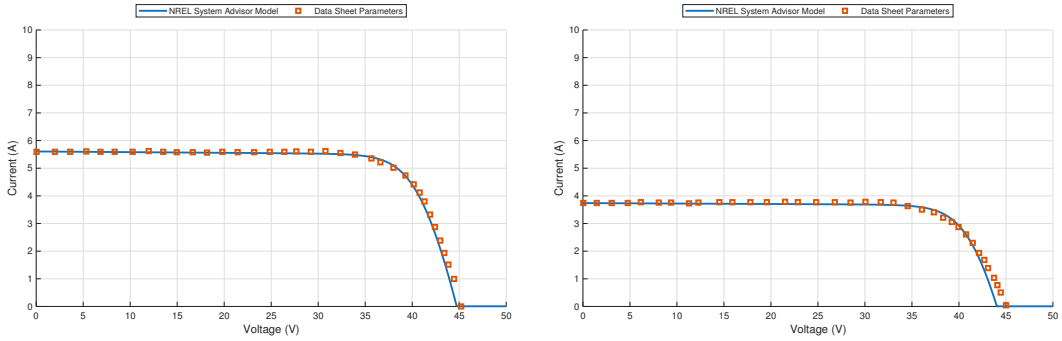
| Description | Variable | Value | Units |
|---|---|---|---|
| Maximum power | $P_{max}$ | 240.9 | W |
| Open circuit voltage | $V_{oc}$ | 39.8 | V |
| Short circuit current | $I_{sc}$ | 7.77 | A |
| Voltage at maximum power point | $V_{mp}$ | 33.6 | V |
| Current at maximum power point | $I_{mp}$ | 7.18 | A |

Numerous mathematical models have been developed to approximate PV module performance using manufacturer data [13–20]. These models seek to enhance prediction accuracy through technological advancements or mathematical simplification. Using data sheet parameters from Table B-1 in combination with the PV Array block in MATLAB/Simulink[13] (which is based on the National Renewable Energy Laboratory System Advisor Model [2018]), the model was configured according the date sheet and simulated. The manufacturer data sheet also contained representative current–voltage (IV) curves at various irradiance levels. These curves were extracted from the data sheet and compared with the model, as shown in Figures B-1 though B-3.



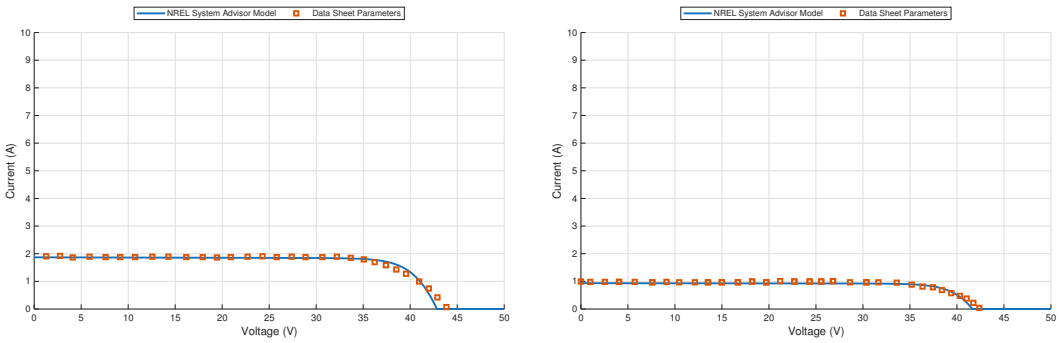

(a) 1000 W/m$^2$ (b) 800 W/m$^2$

Figure B-1: A comparison between the manufacturer data sheet representative voltage–current (VI) curves when compared with the configured Simulink subject to an irradiance ranging from 1000 to 800 W/m$^2$.




(a) 1000 W/m$^2$ (b) 800 W/m$^2$

Figure B-2: A comparison between the manufacturer data sheet representative voltage–current (VI) curves when compared with the configured Simulink subject to an irradiance ranging from 600 to 400 W/m$^2$.

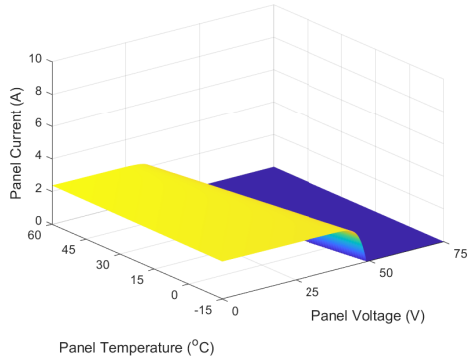



(a) 1000 W/m$^2$ (b) 800 W/m$^2$

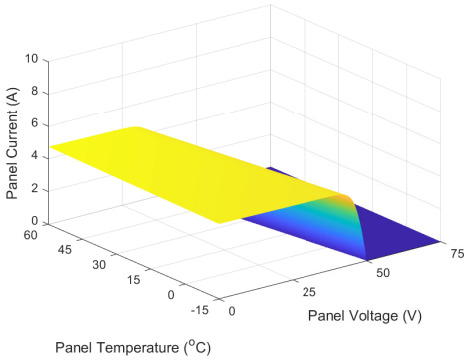
Figure B-3: A comparison between the manufacturer data sheet representative voltage–current (VI) curves when compared with the configured Simulink subject to an irradiance ranging from 200 to 100 W/m$^2$.

As shown in Figures B-1 through B-3, the simulated IV curves closely match those provided by the manufacturer, validating the model's adherence to the PV array's specifications. This indicates the Simulink model can reliably approximate array behavior under varying operational conditions. Furthermore, this model can be leveraged to develop a maximum power point tracking (MPPT) algorithm capable of approximating PV array performance characteristics.

The Simulink model was then subjected to a parameter sweep in which irradiance ranged from 0 to 1200 W/m$^2$, while the panel temperature ranged from –15 to 60 $^o$C, respectively. Based on the application of the model, a family of characteristic IV curves were obtained via the parameter sweep, as shown in Figures B-4 and B-5.

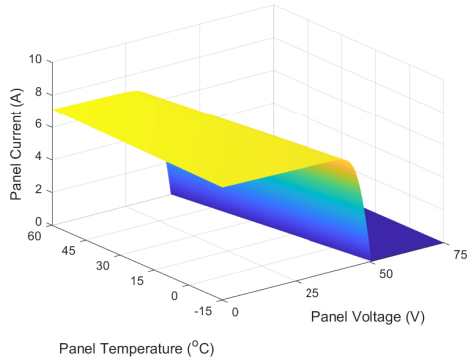



(a) 250 W/m$^2$

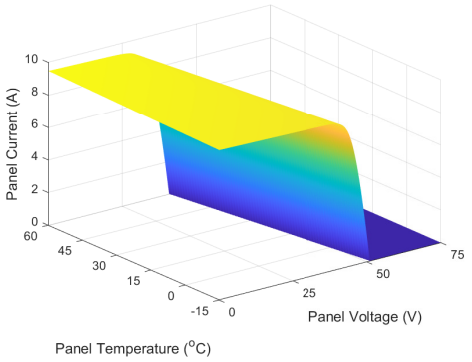



(b) 500 W/m$^2$

Figure B-4: Family of characteristic IV curves subject to variable temperatures and an irradiance ranging from 250 to 500 W/m$^2$. The color gradient represents electrical current, ranging from blue (lowest) to yellow (highest).



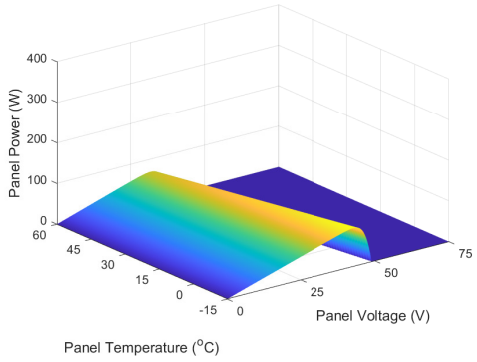

(a) 750 W/m$^2$



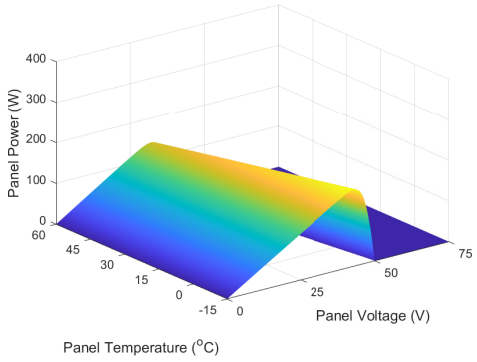

(b) 1000 W/m$^2$

Figure B-5: Family of characteristic IV curves subject to variable temperatures and an irradiance ranging from 750 to 1000 W/m$^2$. The color gradient represents electrical current, ranging from blue (lowest) to yellow (highest).

Similarly, the parameter sweep also produced a family of characteristic power–voltage curves as shown in Figures B-6 and B-7.

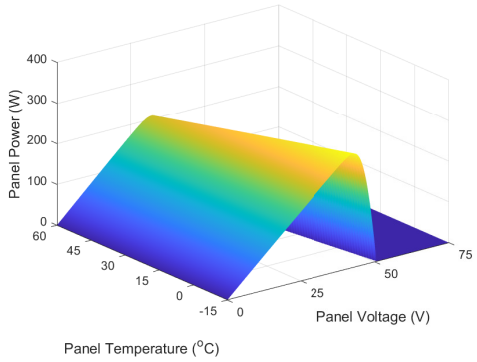



(a) 250 W/m$^2$

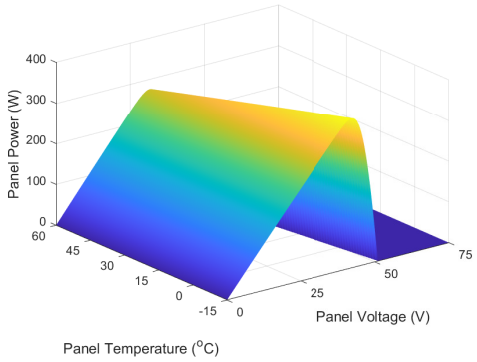



(b) 500 W/m$^2$

Figure B-6: Family of characteristic power–voltage curves subject to variable temperatures and an irradiance ranging from 250 to 500 W/m$^2$. The color gradient represents electrical power, ranging from blue (lowest) to yellow (highest).




(a) 750 W/m$^2$




(b) 1000 W/m$^2$

Figure B-7: Family of characteristic power–voltage curves subject to variable temperatures and an irradiance ranging from 750 to 1000 W/m$^2$. The color gradient represents electrical power, ranging from blue (lowest) to yellow (highest).

Aggregating the complete family of characteristic power–voltage curves enables for the maximum panel power to be approximated for a variable set of irradiance and panel temperature conditions, referred to as a maximum power point (MPP) surface as seen in Figure B-8.

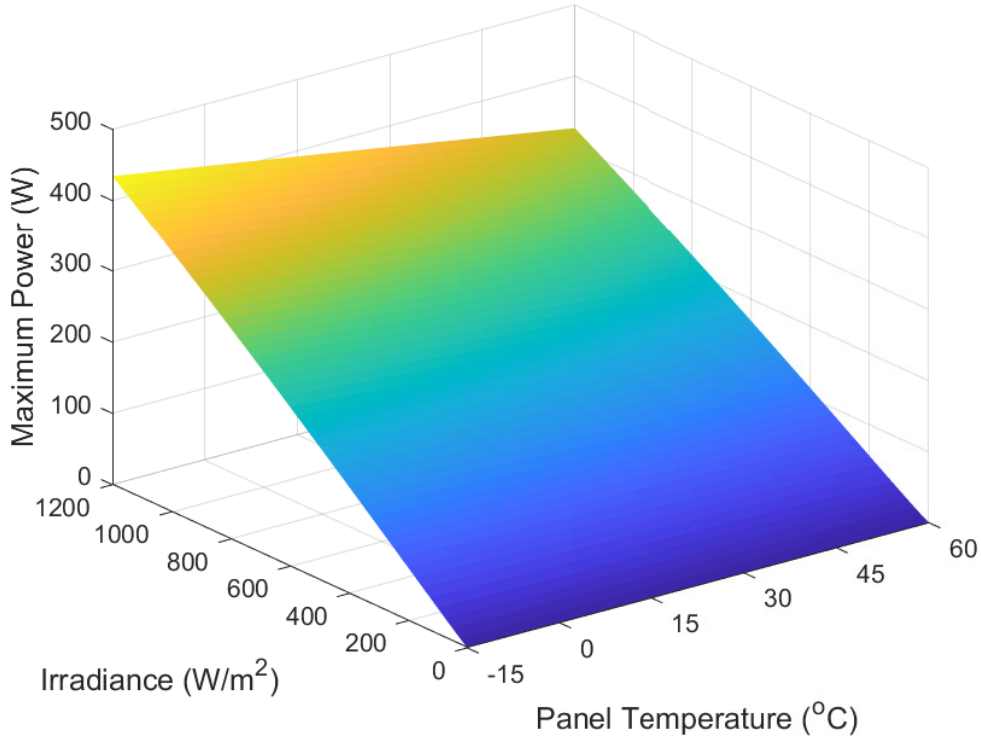



Figure B-8: A multidimensional surface approximating the maximum power point subject to an irradiance and temperature parameter sweep.The color gradient represents electrical power, ranging from blue (lowest) to yellow (highest).

A MPPT algorithm was developed based on the derived multidimensional MPP surface, providing the rationale for this technical report as detailed in the background and motivation material of the preceding report's Section 2.

## List of Symbols, Abbreviations, and Acronyms

| | |
|---|---|
| 1/2D | One-/Two-Dimensional |
| AI | Artificial Intelligence |
| AIHPA | Atmospheric Intelligence for Hybrid Power Advancements |
| ARL | Army Research Laboratory |
| DAC | Data Analysis Center |
| DEVCOM | Combat Capabilities Development Command |
| DoD | Department of Defense |
| EST | Eastern Standard Time |
| E&P | Energy & Power |
| FLIR | Forward-Looking Infrared |
| GA | Genetic Algorithm |
| IR | Inferred |
| IoBT | Internet of Battlefield Things |
| IV | Current Voltage |
| ML | Machine Learning |
| MMT | Meteorological Measurement Tripod |
| MPP | Maximum Power Point |
| MPPT | Maximum Power Point Tracking |
| MSE | Mean Squared Error |
| MST | Mountain Standard Time |
| NOTC | Nominal Operating Cell Temperature |
| PV | Photovoltaic |
| STC | Standard Test Conditions |
| USMA | United States Military Academy |
| VP | Voltage Power |

| | |
|---|---|
| 1 (PDF) | DEFENSE TECHNICAL INFORMATION CTR DTIC OCA |
| 1 (PDF) | DEVCOM ARL FCDD RLB CB TECH LIB |